Master's Thesis

Study and resolution of component deformation in the manufacture of an automotive embedded system

---

Continental Automotive

Czech Technical University in Prague

Faculty of Mechanical Engineering
Department of Automotive, Combustion Engine and Railway Engineering
[**Master of Automotive Engineering**]

Nils Ros-Jacquier

April - September 2023

Thesis assignment

CTU CZECH TECHNICAL UNIVERSITY IN PRAGUE

MASTER'S THESIS ASSIGNMENT

I. Personal and study details

Student's name: **Ros-Jacquier Nils** Personal ID number: **514419**

Faculty / Institute: **Faculty of Mechanical Engineering**

Department / Institute: **Department of Automotive, Combustion Engine and Railway Engineering**

Study program: **Master of Automotive Engineering**

Specialisation: **Advanced Powertrains**

II. Master's thesis details

Master's thesis title in English:

Analysis of defects of the electronic component during packaging – suggestion of elimination of the issue

Master's thesis title in Czech:

Analýza defektů elektronických součástí během balení – návrh eliminace tohoto problému

Guidelines:

- Analysis of twisting/bending of the component rolled on the reel during packaging.
- Mechanical tests and reproduction of the defects/fracture.
- Numerical simulation - winding of flat/plane parts on the cylindrical reel in many layers.
- Laboratory tests of a suggestion for a new packaging.
- Comparation of laboratory tests and the production tests of the suggested solution

Bibliography / sources:

Name and workplace of master's thesis supervisor:

Ing. Josef Kazda ČVUT v Praze, FS, U12201

Name and workplace of second master's thesis supervisor or consultant:

Date of master's thesis assignment: **19.10.2023** Deadline for master's thesis submission: **10.01.2024**

Assignment valid until: _____

Ing. Josef Kazda	doc. Ing. Oldřich Vítek, Ph.D.	doc. Ing. Miroslav Španiel, CSc.
Supervisor's signature	Head of department's signature	Dean's signature

III. Assignment receipt

The student acknowledges that the master's thesis is an individual work. The student must produce his thesis without the assistance of others, with the exception of provided consultations. Within the master's thesis, the author must state the names of consultants and include a list of references.

07/11/2023
Date of assignment receipt

Student's signature

Acknowledgements

I would like to express my deepest gratitude to everyone who contributed to the completion of my master's thesis.

First and foremost, I extend my heartfelt appreciation to Matthieu Fabre for his unwavering support, guidance, and attentive listening. His insights and encouragement have been instrumental in shaping the direction of my research. I also want to thank Cédric Bazin for his invaluable advice and meticulous supervision.

Thierry Fabre, Eric Rames, Clément Saint-Martin, Laurène Salvi, and François Le Rest provided a warm and welcoming environment, offering their expertise that greatly enriched the depth of my research.

Clément Althabegoïty provided valuable guidance, offering insightful direction and playing a key role in the project.

I would also like to thank Denis Aubert and Vincent Banniard for their exceptional availability and continuous support throughout the process. The operators of the SMD 4 production line played a crucial role, and their work and dedication truly were essential to the progress of my work.

Gilles Capdepon, Joachim Fardin, and David Zocca generously offered their aid in my research, displaying admirable availability and assistance.

Finally, I extend many thanks to Manon Gaulhet for her outstanding help, while the constant availability of Nicolas Doret and Dominique Gil was truly appreciated.

Declaration

I hereby declare that the present thesis has been completed independently, on the basis of the information gathered from company expertise, and the litterature sources stated in the list of references at the end of this paper.

In Toulouse, on 21/09/2023.

Nils Ros-Jacquier

For confidentiality reasons, some values owned by Continental Automotive were kept private. However the full reasoning and conclusions drawn are not affected in any way and have not been modified for the sake of the thesis.

Abstract

From April to September 2023, I had the opportunity to carry out an internship oriented towards engineering and research for production at the Continental Automotive plant in Toulouse, France. In the present work, activities conducted throughout the internship have been articulated to respond to the main problem entrusted to me. As so, this thesis investigates recurring deformation affecting an essential component in the operation of an automotive embedded system and identified during production phase. The purpose of the study is to identify the root cause of this deformation, while exploring potential solutions.

This was a newly encountered and unanticipated problem in electronic board manufacturing at Continental. The work for its resolution therefore required gaining an overview and a good understanding of the methods used, then considering a variety of potential key factors contributing to the problem, before focusing the study on the most convincing points. Integrating field data collection, thorough analyses of manufacturing processes, mechanical tests, and numerical simulations into the study enabled a better understanding of the specific component deformation.

Results of the study led to the submission of recommendations to the supplier for mitigating this deformation, mainly focused on the packaging design. Collaborating with the supplier, testing, and comparing initial solution ideas with the existing design, also brought a practical dimension to the research, while addressing the many challenges involved in adapting theoretical projections to production reality, which was essential in reaching future concrete actions to improve production quality.

Résumé

D'avril à septembre 2023, j'ai eu l'opportunité d'effectuer un stage en ingénierie de recherche pour la production au sein de l'usine Continental Automotive à Toulouse. Les activités menées tout au long du stage ont été articulées dans ce rapport pour répondre à la problématique principale qui m'a été confiée. Ainsi, le travail présenté s'intéresse à des déformations récurrentes affectant un composant essentiel au fonctionnement d'un système embarqué automobile, identifiées lors de la phase de production. L'étude vise à identifier la cause racine de cette déformation, tout en explorant des pistes de résolution.

Il s'agit d'un problème nouvellement rencontré et peu anticipé dans la fabrication de cartes électroniques chez Continental. Sa résolution a donc demandé l'adoption d'une vue d'ensemble des méthodes utilisées ainsi que leur compréhension, ce qui a permis d'examiner une série de facteurs potentiels contribuant au problème, avant de concentrer l'étude sur les points les plus convaincants. L'intégration d'observations sur le terrain, d'analyses statistiques, d'études approfondies des procédés de fabrication, d'essais mécaniques ainsi que de simulations numériques a notamment permis de mieux comprendre la déformation spécifique du composant.

Les résultats de l'étude ont permis de soumettre au fournisseur des recommandations pour atténuer cette déformation, principalement axées sur la conception du packaging. La collaboration avec le fournisseur, le test d'une solution proposée et sa comparaison avec l'existant ont également apporté une dimension pratique à la recherche, tout en abordant les nombreux défis liés à l'adaptation de projections théoriques à la réalité, en particulier dans un contexte de production. Cela fut essentiel à l'adoption d'une direction vers des actions concrètes futures en vue d'améliorer la qualité de la production.

Abstrakt

Od dubna do září 2023 jsem měl možnost absolvovat stáž zaměřenou na inženýrství a výzkum pro výrobu v závodě Continental Automotive v Toulouse ve Francii. V této práci byly činnosti prováděné v průběhu stáže formulovány tak, aby odpovídaly na hlavní problém, který mi byl svěřen. Tato práce se tak zabývá opakujícími se deformacemi, které ovlivňují základní součástku v provozu vestavěného systému automobilu a které byly identifikovány ve fázi výroby. Cílem studie je identifikovat základní příčinu této deformace a zároveň prozkoumat možná řešení.

Jednalo se o nově vzniklý a neočekávaný problém při výrobě elektronických desek ve společnosti Continental. Práce na jeho řešení proto vyžadovala získání přehledu a dobrého porozumění používaným metodám, poté zvážení různých potenciálních klíčových faktorů, které k problému přispěly, a následně zaměření studie na nejpřesvědčivější body. Začlenění sběru dat v terénu, důkladné analýzy výrobních procesů, mechanických zkoušek a numerických simulací do studie umožnilo lépe pochopit konkrétní deformaci součástek.

Výsledky studie vedly k předložení doporučení dodavateli pro zmírnění této deformace, která se zaměřila především na konstrukci obalu. Spolupráce s dodavatelem, testování a porovnávání prvotních nápadů na řešení se stávajícím designem přineslo do výzkumu také praktický rozměr a zároveň řešilo mnoho problémů spojených s přizpůsobením teoretických projekcí výrobní realitě, což bylo nezbytné pro dosažení budoucích konkrétních opatření ke zlepšení kvality výroby.

Glossary

AOI	Automated Optical Inspection
BSRF EA	*Boîtier de Servitude Radiofréquence* - External Antenna Radio Frequency Control unit - External Antenna
C.E.M.S.	Continental Electronic Manufacturing Services
CISPR	*Comité International Spécial des Perturbations Radioélectriques* International Special Committee on Radio Interference
DOE	Design Of Experiment
EFT	Electrical Fast Transient
EMC	Electromagnetic Compatibility
EMI	Electromagnetic Interferences
ESD	Electrostatic Discharges
FIFO	First In, First Out
GPS	Global Positioning System
AI	Artificial Intelligence
ISO	International Organization for Standardization
PCB	Printed Circuit Board
RF	Radio Frequency
RFI	Radio Frequency Interference
SMD - SMT	Surface-Mounted Devices - Surface-Mount Technology
T&R/TnR	Tape And Reel
8D	8 Disciplines

Contents

Introduction

The miniaturization of electronic products, coupled with increased complexity and performance, introduces new design and manufacturing constraints in various industries. The automotive equipment sector, in which Continental Automotive is a major player, is no exception. Electromagnetic compatibility (EMC) is one of these key constraints. Continental Automotive has chosen to enhance EMC on numerous products by using EMI (Electromagnetic Interference) shields, which are metallic components covering a specific area to protect on an electronic circuit board.

The present work addresses an issue related to the production process specific to the assembly of EMI shields on the electronic board of one of Continental Automotive's newly manufactured products, the BSRF EA. Indeed, after the assembly of components and shields on the board, one of these shields consistently exhibits mechanical deformation, constituting a manufacturing defect, thus making the entire board unusable.

In essence, this study aims to trace the origin of this issue, once it has been clearly characterized, and attempt to find one or more adapted curative solutions. Root cause analysis will be the focal point of this study. Adopting as broad a view as possible towards the product's lifecycle is of utmost importance for rigorous inductive reasoning.

The packaging of the specific component has garnered significant attention due to its role in the issue at hand. While a comprehensive and definitive curative solution may not be fully developed and implemented at the conclusion of this study, the resulting conclusions can still be valuable to all organizations involved. Indeed, by exploring this new and less-anticipated industrial challenge, valuable lessons can be derived for optimizing design and industrialization processes. Toward the end of this work, the discussion will focus on the approach to adopt when defining the initial specifications provided to a subcontractor, emphasizing the importance of thorough risk assessment.

Throughout the study, it has been crucial to adopt a position that combines several aspects. On one hand, a strong involvement in production was necessary to investigate the observed defect. On the other hand, it was important to leverage the rich expertise available within the company's internal technical competence center, to which I was attached. Additionally, ongoing communication with the relevant industrial project (product development and industrialization) was essential to reach decisions in alignment with the various stakeholders involved (both internal and external). Lastly, a pivotal aspect of this work has been to adopt a research-oriented perspective, in close collaboration with the company's technical laboratories.

Chapter 1

Context of the study and state of the art

1.1 Presentation of the company

1.1.1 Overview and activities

The Continental Group is a multinational automotive equipment manufacturing group created in 1871, and whose parent company, Continental AG, is based in Hanover, Germany. Continental's best-known field of expertise is tire manufacturing: the company is regarded as the world's fourth-largest tire manufacturer behind Bridgestone, Michelin, and Goodyear. However, the company's activities are not limited to that. Indeed, over the course of its history, Continental has diversified from rubber and tire manufacturing and is now specialized in a variety of automotive technologies, such as brake systems, safety systems and ADAS (Advanced Driver Assistance Systems), tire pressure sensors, as well as chassis and powertrain electronic systems (via the Vitesco technologies branch).
Nearly 200,000 people work in the Continental group worldwide (199,038 employees as of 2022), over 519 different locations, see Figure 1.1.

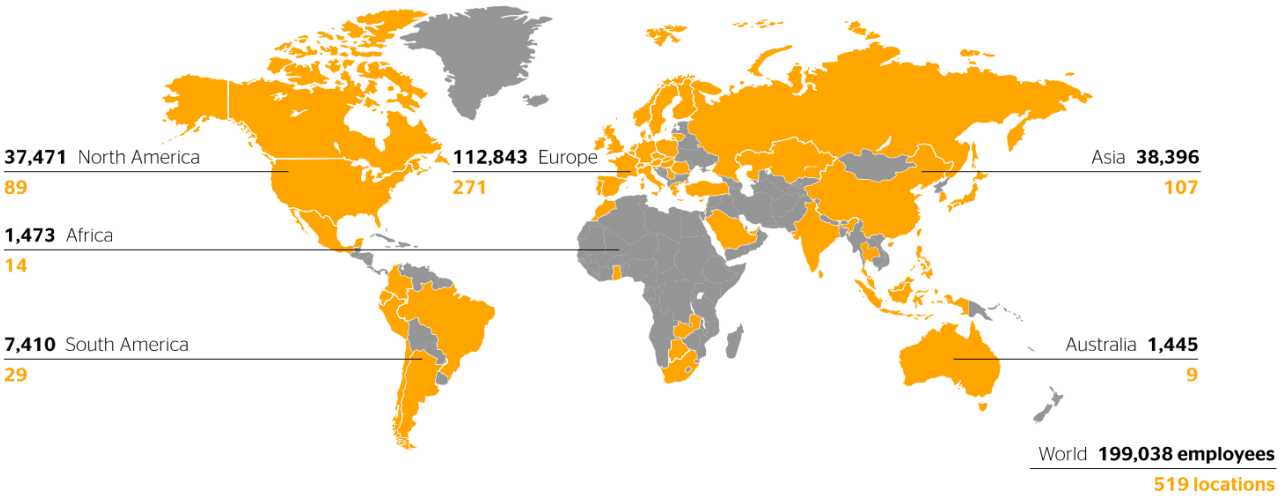

Figure 1.1: Map of Continental locations around the world [1].

The expertise at Continental is organized into three main group sectors [1]:

- **Continental Automotive:** Technologies for passive safety, brake, chassis, motion, and motion-control systems.
- **Continental Tires:** Innovative solutions in tire technology for the car, truck, bus, two-wheel, and specialty tire segment, and digital tire monitoring and management systems.
- **ContiTech:** Development and manufacturing of cross-material, environmentally friendly, and intelligent products and systems for the automotive industry, railway engineering, mining, agriculture, and other key industries.

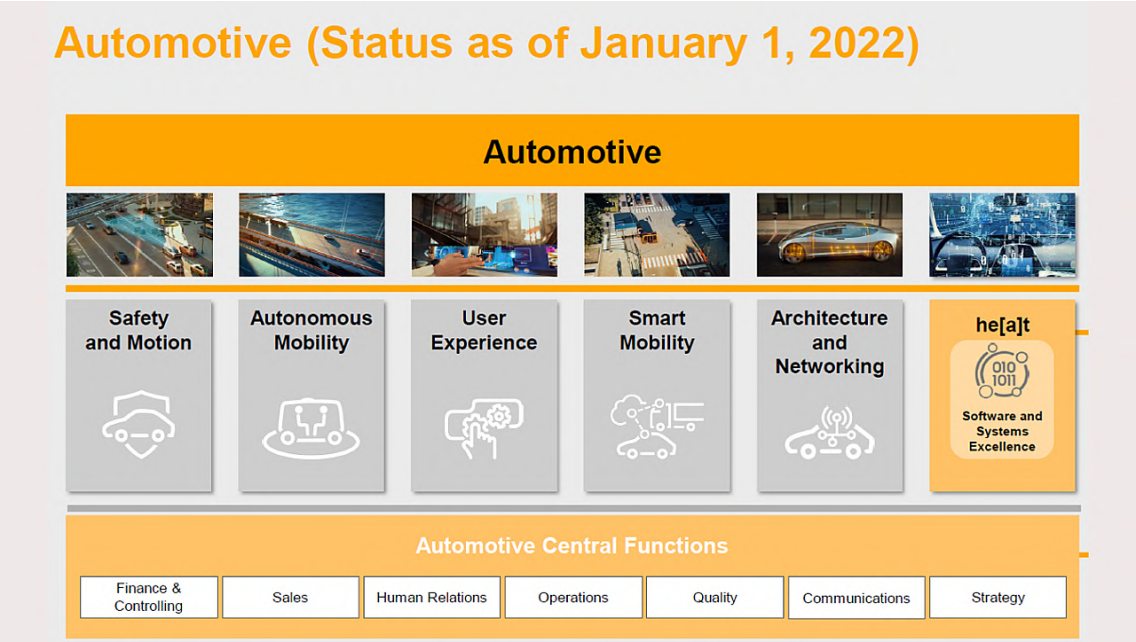

Figure 1.2: Organization of the Automotive Business Area [3].

The Continental Automotive group sector is further divided into six business areas: Architecture and Networking, Autonomous Mobility, Safety and Motion, Smart Mobility, and User Experience [1] [3].
The present work addresses activities forming part of the Architecture and Networking Business Area, in the Operations section.

1.1.2 The Toulouse location

The plant in Toulouse, France, houses the headquarters of Continental Automotive France, and is nowadays the workplace of 1,450 people, in management, R&D, and production. The history of the plant began in 1979 when Renault and Bendix jointly founded Renix. The company had 90 employees in 1979, which grew to 500 by 1985. After 1985, Renault sold its shares entirely to Bendix, who then sold it to Siemens in 1988. Siemens VDO had six production sites in France, with the largest in Toulouse employing 1,900 people. After 30 years of existence, this branch was

bought by Continental.

In 2019, Continental's Power Train division became Vitesco Technologies, with plans for an IPO (Initial Public Offering) in 2020. This change led to reorganization at the production facilities in Foix and Boussens, two other production sites in the south of France, within Vitesco Technologies (Power Train). Simultaneously, part of Continental's Toulouse site underwent redevelopment. In 2017, prior to the industrial split-up between Continental Automotive and Vitesco Technologies, the Toulouse location employed 2,300 people and the group reported sales exceeding one billion euros.

1.2 Industrial context

1.2.1 The BSRF EA product

The BSRF EA (*Boitier de Servitude Radiofréquence* - External Antenna) is the latest addition to the BSRF product range manufactured by Continental Automotive for the Stellantis group (formerly PSA and FCA). Production began in early 2023. Its purpose is to control the "shark" antennas fitted to some of the new vehicle models. Installed on the roof of the vehicle, its role is to ensure all types of communication with the outside world. It provides 4G and 5G connectivity through local WiFi in the cabin and transmits GPS data, for example [4].

Figure 1.3: Shark antenna on a vehicle's roof.

Shark antennas are becoming increasingly popular in the new vehicle market, primarily as a result of the miniaturization of electronic equipment. What's more, they meet a need for robustness, where a conventional antenna is sensitive to the climate and all kinds of external aggression, due to its size and fragility. BSRF enables this type of antenna to deliver excellent performance, for example in voice communication [2]. The shark antenna emits and receives electromagnetic waves at Radio Frequencies (RF), thus the BSRF is designed to process RF data.

The BSRF V1, an earlier version of the product, is currently produced in Sibiu, Romania. It is designed to be mounted directly under the shark antenna on the roof of the vehicle.

(a) Module assembly (b) Exploded view

Figure 1.4: Example of Continental intelligent antenna module [4].

However, the subject of this study is exclusively related to the BSRF EA version, currently in production at Continental Automotive France in Toulouse for the industrialization phase. This is a more compact version, separate from the antenna. This means that the product's electronic box is located elsewhere on the vehicle, and connected by cable to the antenna.

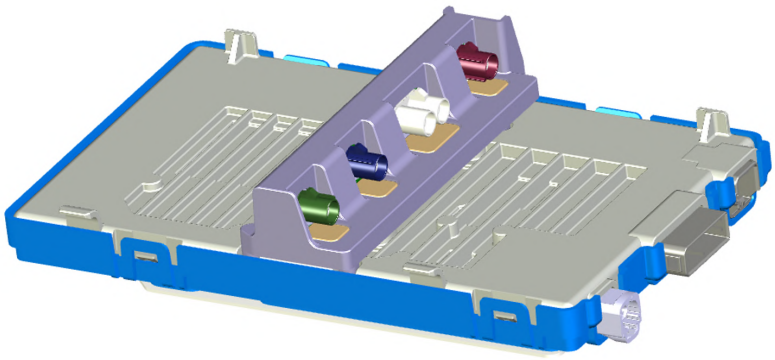

Figure 1.5: 3D view of the BSRF EA assembly (CAD).

The BSRF EA consists of an electronic board protected by a screwed housing. The circuit board, equipped with multiple components mounted on both sides - top and bottom - is mainly assembled on the Front-End phase of manufacturing, by SMT (Surface-Mount Technology), see part 1.2.2.

Next, some processing is applied and the PCB (Printed Circuit Board) is finalized on a "Middle-End" line. Finally, the electronic board is linked to the input and output connectors, assembled and encapsulated in the screw-on housing on the Back-End line, or "final" line.

1.2.2 Principle of SMT

Electronic devices and components mounted onto the PCB (Printed Circuit Board) can either be "through-hole" or "surface-mounted". On the one hand, "through-hole" components are assembled to the board by inserting their leads through the PCB and soldering them on traces located on the other side of the

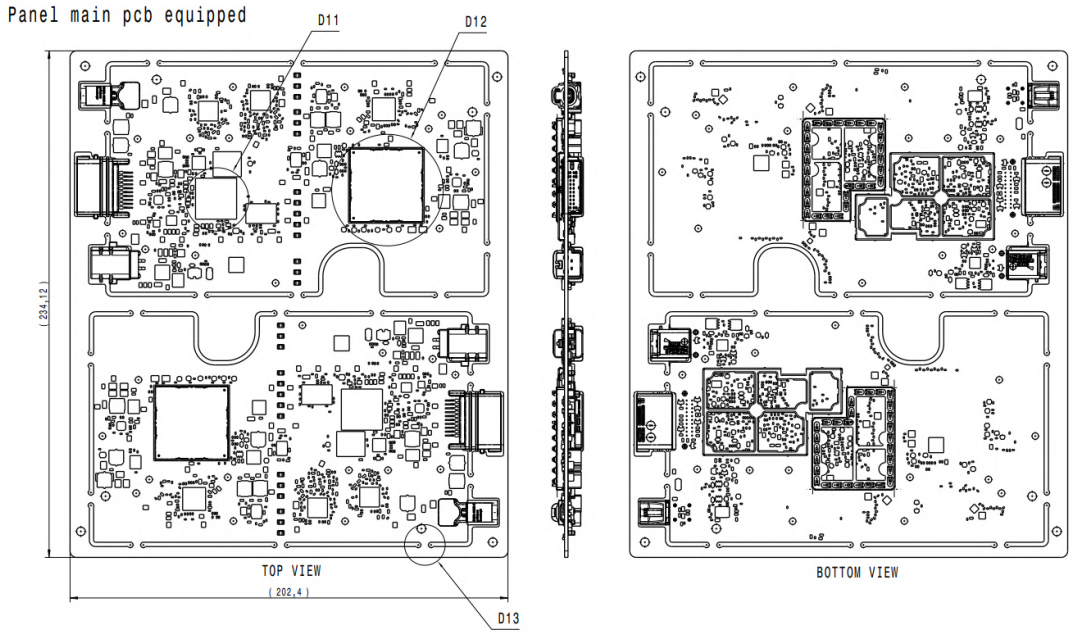

Figure 1.6: Fully equipped PCB panel for the BSRF EA, displaying 2 board units.

board. SMDs (Surface-Mounted Devices), on the other hand, have their electric pins connected directly to copper tracks on the same side of the board. Both methods are sometimes used on the same board, although most electronic boards nowadays are assembled using SMT, as in the case of the BSRF EA.

Thus, Front-End production for the BSRF EA consists in an SMD line and is the first stage in the manufacture of an electronic board, after PCB production. At Continental Automotive, PCB manufacturing is subcontracted, and product-specific PCBs are delivered from various overseas suppliers.

The blank PCBs that are the basis and starting point of the SMD assembly therefore have a predefined printed circuit. They are made up of a multitude of copper layers - providing the electrical connection between surface-mounted components - separated by an insulating material such as epoxy resin, which can be reinforced with glass fiber.

Depending on the product, several electronic board units are grouped together on the same PCB panel: 2 in the case of the BSRF EA, see Figure 1.6. The boards are then separated later in the manufacturing process when the panel is cut by milling on the Back End line.

The present section presents the global sequence of processes needed for Front-End production with SMT. The specific features of the SMD line for BSRF EA and details regarding the component concerned by the study will be discussed in further sections (see Parts 1.2.3 and 1.3.1).

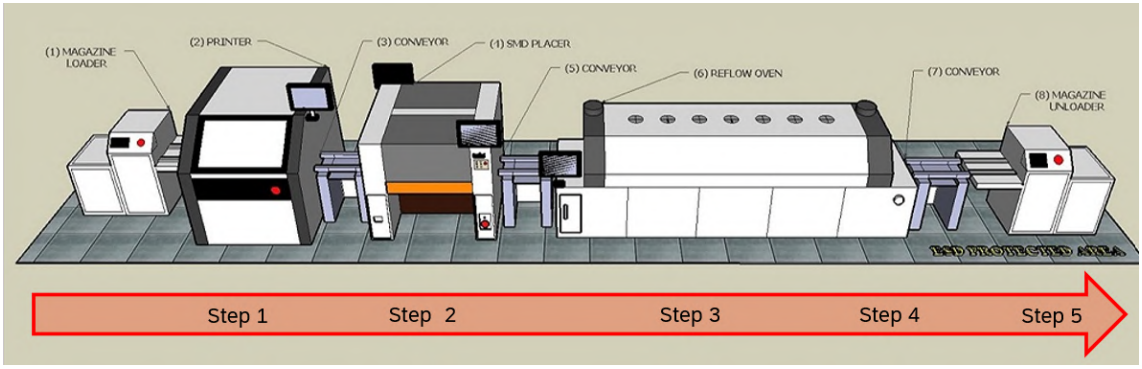

Figure 1.7: 3D view of a typical SMD line, showing the steps of SMT [10].

Step 1: Screen printing

Solder paste is a suspension of metal powder within a substrate called solder flux, often rosin-based. It acts both as a fixing base for the components placed on the PCB surface (in step 2), and as a conductive interface between them and the conductive trace terminations.

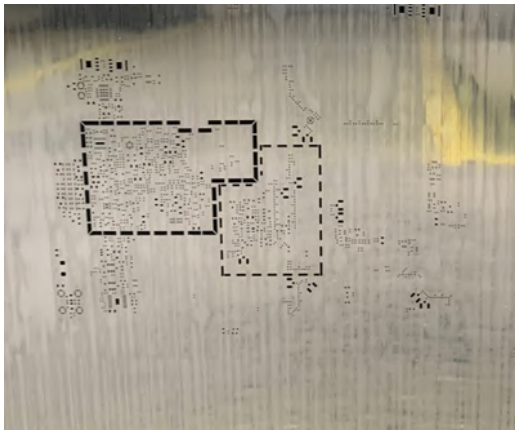

Figure 1.8: Stencil used for the bottom side of the BSRF EA PCB

As they enter the SMD line, blank PCBs are conveyed into a screen-printing machine. The solder paste is spread over the entire surface of the PCB through a stencil, specific to each product (see Figure 1.8). The stencil is placed between the blank PCB and the supply of solder paste placed in a squeegee, to fill the appropriate slots with this conductive paste.

Following this process, the PCB panel is scanned for an AI program to check the quality of the solder paste distribution to the intended areas. Any defects are reported, and the PCB panel is then scrapped.

Step 2: Placement

Once the solder paste has been applied to the PCB, the components can be positioned at their respective locations. Depending on the product, a single PCB can house dozens of different components. The components are installed in the so-called pick-and-place stage. Most of the electronic components and other parts to be mounted on PCBs are packed inside a reel (Tape-and-Reel type packaging, or T&R). In this way, components are inside in a flexible plastic tape wound into a reel, which allows good spatial density of stocks, while guaranteeing a fluid and continuous supply to the placement machines. Nevertheless, some components are sometimes packed inside trays or tubes. These are often very bulky components,

such as connectors, which are more efficiently packaged in other ways than on reels.

Before the components can be mounted on the PCB, they must be removed from their packaging. This action is automated and performed directly by the placement machine. Components are supplied to the placement machines via component feeders. In the case of feeders adapted for T&R component packaging, these are equipped with electric motors whose role is to pull the tape and thus unwind the reel while removing the protective film. This enables components to be distributed according to demand.

The kinematics diagram shown in Figure 1.9 is relatively generic, as transmissions may vary depending on the feeder reference, i.e. on its size, and even on the number of versions available for a given size.

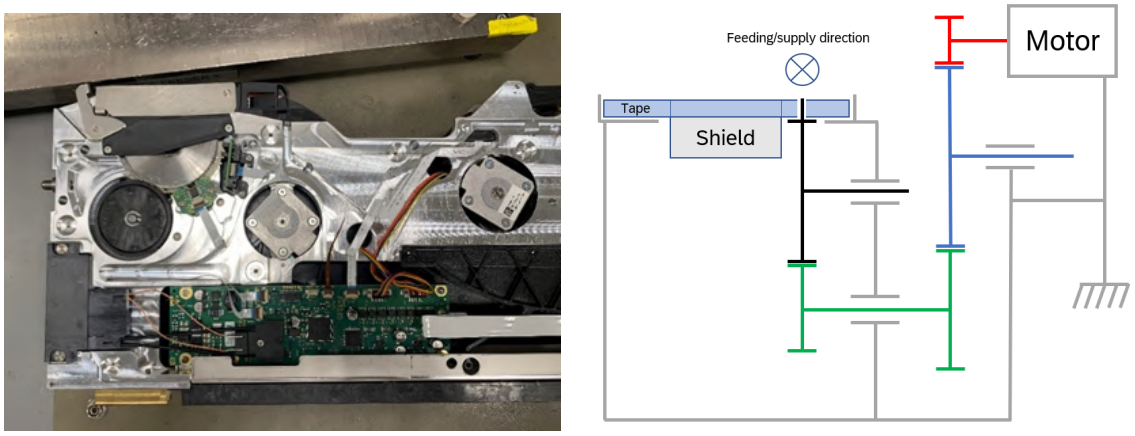

(a) (b)

Figure 1.9: Typical placement machine feeder (a) with the corresponding kinematics diagram (b)

Placement machines are equipped with two rotating heads on which suction nozzles adapted to the geometry of each component are mounted. These pick up the component by suction and transport it to its precise position on the PCB.

Lastly, the heads place each component in its slot, applying a slight force (a few Newtons, depending on the component) to ensure that the electronic pins are correctly immersed in the solder paste.

Fully equipped PCBs are then conveyed to the output of the placement machine, where a vision system automatically checks component positioning on the board layout. The PCBs then enter an industrial reflow oven.

Step 3: Reflow

The reflow process consists of fusing the soldering paste to the component pins, so as to secure them to the PCB, thus ensuring the quality of electrical connections and mechanical strength. Several reflow oven technologies are available. Small LED reflow ovens are sometimes used for laboratory operations, while larger manufacturers prefer in-line reflow ovens. Infrared (IR) reflow was originally used but has

now been largely replaced by convection reflow. Convection reflow ovens offer many advantages, including uniform heating. Modern reflow ovens mainly use closed-loop convection.

Figure 1.10: Reflow oven

In the oven, the PCBs are conveyed at variable speeds through different oven zones, each of which has a set temperature to gradually raise the temperature undergone by the PCB panel. Each zone is equipped with electrical resistors and fans at the top and bottom, generating a controlled flow of hot air. The result is a maximum temperature of around 250°C, depending on the product being manufactured.

Temperature control is essential in the reflow process, as it must be high enough to reflow the paste without damaging sensitive electronic components. To achieve this, each heating zone is programmed to a specific setpoint temperature, corresponding to the phases required for successful reflow:

- Phase 1: Flux[1] activation.
- Phase 2: Eutectic point[2] crossing.
- Phase 3: Reflow of the solder paste and component pins.
- Phase 4: Cooling.

The hot air flow generated by the fans ensures uniform heat distribution in each heating zone.

In the case of closed-loop convection ovens, the temperature is controlled in real-time by temperature sensors. These sensors continuously measure the temperature

[1]Fluxes are chemicals used to strip and clean metal surfaces prior to soldering. They remove impurities and oxidation, enabling better adhesion of solder to components and boards.

[2]Eutectic point: transition state of solder paste between solid and liquid.

throughout the PCB conveyor and adjust the heating power and airflow accordingly to maintain the desired temperature. The closed loop refers to the feedback system used to adjust oven parameters according to real-time temperature measurements. This feedback system ensures precise and constant temperature control throughout the entire reflow process.

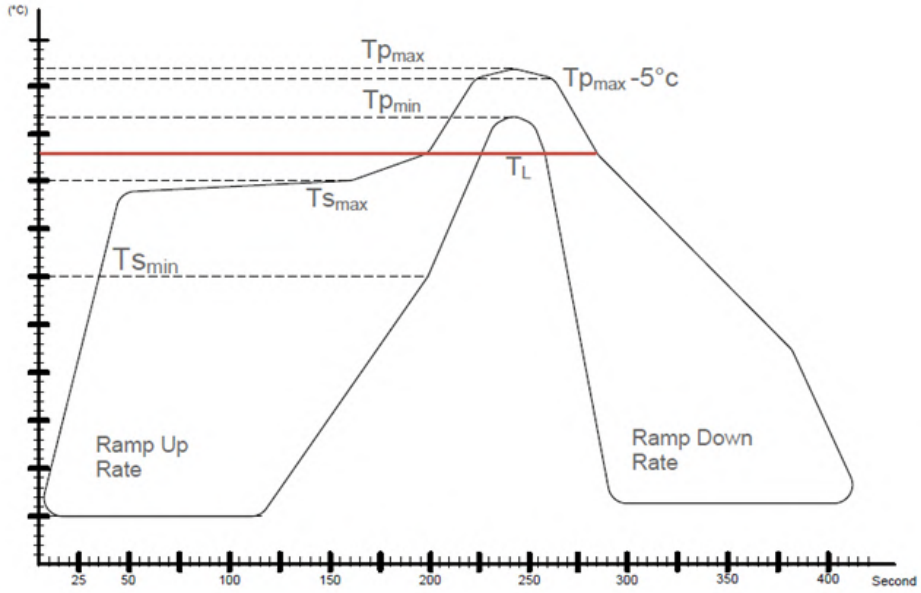

Figure 1.11: Temperature profile template used for the reflow process

The temperature is raised in stages. In the pre-heating or pre-soldering phase, the PCB is gradually brought up to the melting point of the soldering paste. This avoids thermal shock, which can damage the board and its components. It also ensures even heating of the PCB. Heterogeneity can lead to undesirable thermo-mechanical deformation (see Part 2.5.2). The phenomenon known as Soak occurs during this pre-soldering phase: the fluxes of the soldering paste melt. The temperature set during this phase enables the fluxes to be activated, which is essential for high-quality soldering: the activated fluxes clean the surfaces by removing contaminants, and they also facilitate the mixing and fusion of the soldering material with the parts to be soldered. The Soak phase is often recognizable on a temperature profile as the temperature plateau covering the first part of the reflow.

The maximum temperature is then reached. The soldering paste, which is now isolated from the flux evaporated during the Soak stage, begins to melt. At peak temperature, the surface tension at the joints is reduced, allowing the solder to take on the desired shape and properties. Controlled cooling takes place and brings the panel to a temperature close to the outside temperature. Therefore, cooling of the panel begins long before it comes out of the reflow oven.

Step 4: Cooling

More than the primer of the cooling is part of the reflow process. Indeed, once the PCBs have passed through all the heating zones, they are conveyed to the cooling sections, where the airflow is adjusted to cool the solder joints and fix the electronic components in place. Thus, the main cooling action on PCBs takes place within the oven itself, as they pass through the cooling sections, where the set temperature often drops below 40°C.

The panels are then conveyed from the oven to an air-cooled storage area, operating on a FIFO (First In First Out) basis, where they are held for a fixed period. These FIFOs ensure that the PCBs are continuously cooled down to room temperature, following the cooling process initiated in the last oven compartments.

The PCBs are then delivered for inspection and storage.

Step 5: Final inspection and storage

Towards the exit of SMD lines, AOI (Automated Optical Inspection) is performed for final SMD quality control on each PCB panel. The system runs all the control programs defined for the product being manufactured. In the case of any defect detection, the panel is set aside for visual examination by a dedicated operator, leading to the scrapping of the panel if the defect is confirmed.
Final storage is carried out in racks on wheels, arranged in dedicated corridors marked on the floor. This enables the blanks to be put on standby for electronic board function tests.

After validation, stocks of equipped panels are sent to the Back-End line, where the final product is assembled.

Even though final AOI is a reliable defect detection system, there are control stages between each process described above (after screen printing, pick & place, and reflow): Optical control systems (lasers or cameras for instance) interact with AI-enabled programs to perform these checks. Operators can also carry out visual checks at any time.

The time of each passage under the control vision (called "BISAC") gives temporal information on the passage of the panel, which is useful for obtaining traceability of each part produced. For example, if the search engine dedicated to traceability indicates "BISAC oven: 12h17", this means that the part entered was controlled at the oven entrance at 12h17.

Challenges of SMD quality

SMD quality is a critical issue for industrial performance, for financial matters as well as for environmental concerns. Indeed, depending on the number of electronic board units on a single panel, defects on one unit will lead to the scrapping

of the whole panel. In the case of the BSRF EA, defects on any of the mounted components cause the scrapping of both units of the PCB panel.

These are complex and costly products, involving highly energy-consuming manufacturing processes, and containing precious raw materials such as rare earths, as well as synthetic compounds whose potential release into the environment would be hazardous[3]. Emphasizing the impacts of SMD production and electronics systems manufacturing as a whole allows understanding the scope of such responsibilities for the actors in play, motivating the need for continuous process improvement.

1.2.3 Specific features of BSRF EA Front-End production

Figure 1.12: C.E.M.S. logo

At present, most of the processes involved in Front-End manufacturing of the BSRF EA's electronic board are carried out in the C.E.M.S. (Continental Electronics Manufacturing Services) workshop.
C.E.M.S. is Continental's competence center for industrial electronics manufacturing technologies. The workshop, which is a detachment of the factory, handles the production of new products in small series, as well as prototypes. In fact, Continental Automotive is constantly evolving and improving its mechanical and electronic design, in order to meet the demand for miniaturization and technological improvements. In addition, the C.E.M.S. workshop is currently being refurbished to provide production flexibility in line with the 4.0 Industry philosophy.

The operators working in the C.E.M.S. workshop are highly qualified, versatile, and autonomous, due to the difficulty of managing the workshop's production lines. Indeed, these lines need to be flexible, and most of them have to support the manufacture of many different products, which implies numerous configuration changes. What is more, the smaller production volumes required in the workshop compared with mass production cause the machines to be older, slower, and prone to breakdowns or malfunctions.

Ultimately, the BSRF EA is intended to be industrialized as part of mass production, with an SMD line, a Middle-End line (specific to this product, where further treatments are applied to certain components), and an innovative Back-End line, using multi-axis robots.

The SMD4 line has 3 component placement machines (i.e. 6 reel racks like the one shown in Figure 1.13). The first placement machine is designed for micro-components, and the following ones for larger components, in particular large electronic components, but also electromagnetic protection elements. The latter are the focus of this study and will be introduced in the following section.

[3]Recycling is not currently applied to scrapped products, but touch-ups remain possible. However, very few customers (car manufacturers) endorse these practices to be performed on products they purchase.

Figure 1.13: Component reel rack used for the BSRF EA production configuration.

At Continental Automotive France, the pick-and-place machines do not operate according to a predetermined task schedule. In fact, the pick-and-place of each component is carried out in a precise order but is triggered by demand, i.e. the presence on the line of the PCB ready to be fitted.

The two pick-and-place heads operate in double flow, with components arriving from opposite sides of the placement machine, to optimize component placement time on the PCB.

The BSRF EA electronic board has two sides: top and bottom. This means that each panel has to undergo the SMD process (Front-End) twice, with a different line configuration specific to the set of components to be mounted on each side.

1.3 Meeting the requirements for EMI protection

1.3.1 BSRF EA shields

Purpose and overview

The miniaturization of products generates new constraints, in particular relating to electromagnetic compatibility between components or with other electronic elements. The operation of the electronic board, conditioned by the quality of the signals circulating between the components on the printed circuit board, can be compromised by a number of factors. These factors include the proximity of the many components on the PCB, as well as the presence of an external electromagnetic environment cluttered by signals from the many systems onboard new vehicles. Underlying this issue is the subject of EMI, described in detail in the Appendix A.

It is compulsory for electronic systems manufacturers to measure and control the level of electromagnetic emissions from a component or group of components installed on the PCB. In the case of the electronic board designed for the BSRF EA, these were deemed to be too high, according to the relevant standards set out in the

EMC Directive 2014/30/EU[4]. Indeed, in order to bear the CE mark, any product falling within the scope of this directive must comply with the conditions stipulated therein.

To solve this problem, highlighted by the RF design office, the BSRF EA project team chose a solution that is often used in such cases: the installation of electromagnetic shielding tools on the areas of the PCB surface to be protected.

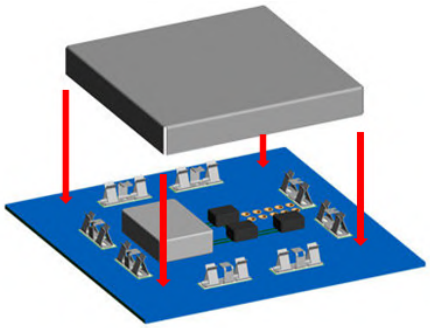

Figure 1.14: Schematic example of an EMI shield and its positioning on a PCB

Two shields are mounted on the underside (or bottom side) of the BSRF EA PCB. Although they are not electronic components, they are installed on the PCB within the SMD line, during the placement stage. Their role is to cover an area dense with components, so as to limit electromagnetic interference in this area as required.

The problem studied in this report concerns a problem observed on these shields, following assembly on the SMD line of the underside of the BSRF EA electronic board.
At SMD line visual inspection, some panels show shield defects: some of these very thin metal parts are deformed and bowed. The defect observed will be described later in this report.

Shield architecture, geometry, materials and characteristics

There are two EMI protection shields mounted on the underside of the BSRF EA PCB. Their geometry and dimensions are shown in Figures 1.15 and 1.16, taken from the technical drawings detailed in Appendix B.

	MSA Shield	**LAIRD Shield**
Drawing - Illustration	Figure 1.15	Figure 1.16
Material	TS 275	TS 275
Sheet thickness	0.2 mm	0.2 mm
Conditioning	T&R	T&R
Parts per reel	230	250
Mounting stage	SMD	SMD

[4]Directive 2014/30/EU of the European Parliament and of the Council of February 26, 2014 on the harmonization of the laws of the Member States relating to electromagnetic compatibility.

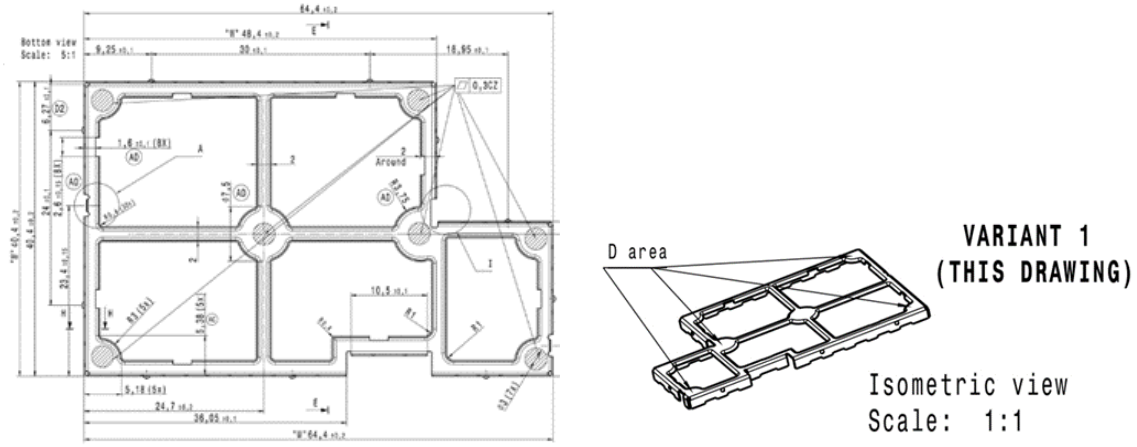

(a) (b)

Figure 1.15: Top (a) and isometric (b) views of the shield provided by MSA, currently in use at BSRF EA's production facility in Toulouse. Dimensions in mm. Scale 1:1 is not respected. A full drawing is available in Appendix B.

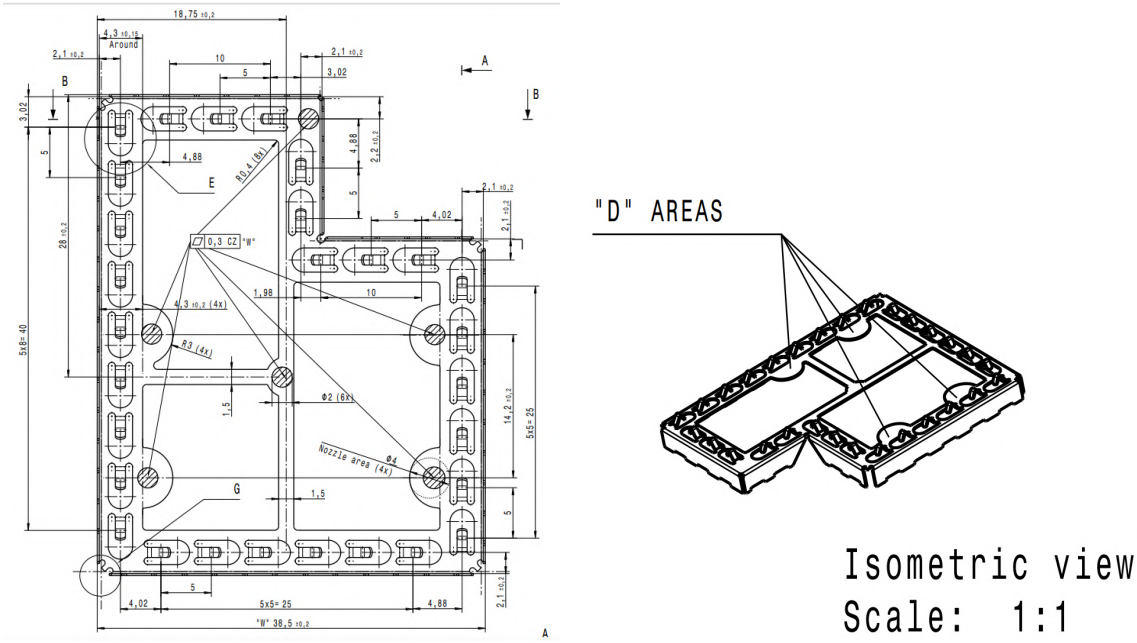

(a) (b)

Figure 1.16: Top (a) and isometric (b) views of the shield provided by LAIRD. Dimensions in mm. Scale 1:1 is not respected. A full drawing is available in Appendix B.

The first shield shown (Figure 1.15) is designed to accommodate a metal cover, which is installed later in the assembly process, at the end of the Middle-End stage. This allows the machines to maintain better accessibility to the PCB surface so that Middle-End treatments can be carried out before all the covers are installed at the same time.

The other shield (Figure 1.16) is fitted with hook-shaped attributes around the perimeter of its top surface. These are in fact springs that ensure electrical contact with an aluminum plate integral to the housing (final assembly, Figure 1.5), in order to ground the shield.

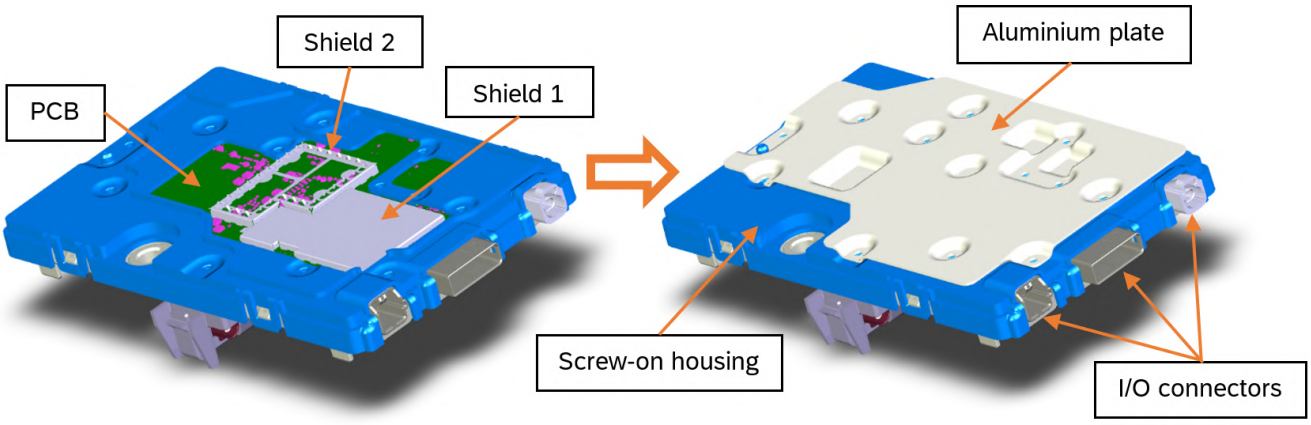

Figure 1.17: Assembly of the aluminum plate on the metal case, over the EMI shields on the bottom side of the PCB. Contact is established by the shield springs for grounding.

The metal sheet thickness used for the latest versions of shields, which are currently in production, is 0.2 mm.

The material used for these EMI shielding parts is TS275 steel. Its mechanical properties are detailed in the following table. Nominal values found in the literature are given [11] [12].

Property	Symbol	Nominal value	Dimension
Material name	TS 275		
Density	ρ	7850	kg/m^3
Young's Modulus	E	210	$GPa = 10^3 N/mm$
Yield strength at 0.2%	$R_{p_{0,2}}$	275	$MPa = N/mm$
Tensile strength	R_u	375	$MPa = N/mm$

Reel packaging

BSRF EA EMI shields are packaged in reels. For the shield shown in Figure 1.15, each reel contains 230 parts. For the LAIRD shield (Figure 1.16), each reel contains 250 parts.

The tape consists of a series of compartments, each containing a shield. These compartments are thermoformed into the plastic tape, and covered with a film which is automatically removed at the last moment by the feeder before the shield is placed on the PCB by the placement machine.

To enable the tape to be driven by the feeder, as demonstrated on the kinematics diagram (Figure 1.9), holes are drilled all along the tape, on either side of the compartments.

For a good understanding of the mechanical analyses carried out much later in this work, it is crucial to point out that it is believed that the supplier manually

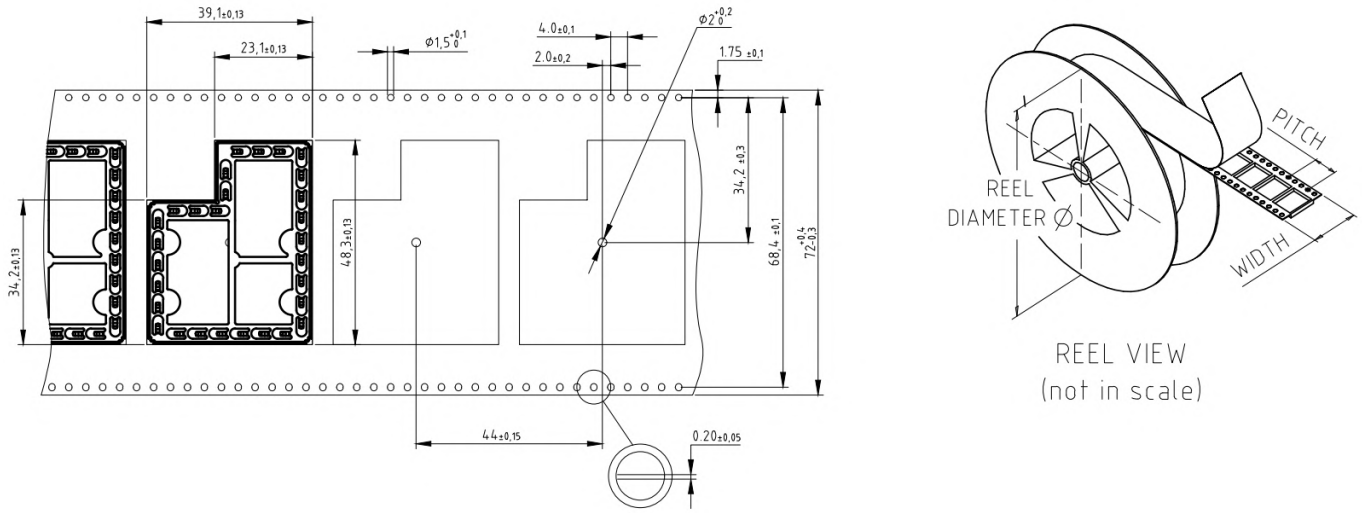

Figure 1.18: Supplier's drawings of the T&R packaging for the BSRF EA LAIRD shield. Dimensions in mm. The complete drawing is available in Appendix B.3

winds the shield reels upon production and packaging before shipping, or at least does not ensure equal tension of the tape once the winding is done and the reel is packed and conditioned for shipping.

Supply to production

As described above, Continental Automotive France has subcontracted the manufacture and packaging of the shields mounted on the underside of the BSRF EA's electronic board to LAIRD. Batches of reels are delivered from the supplier (LAIRD) by truck and stored by a logistics provider, Daher.

The logistical flow of components received by Continental Automotive France is as follows:

Upon delivery, the batches of boxes are checked: warehouse logistics ensure that the expected deliveries have been made. The reel boxes are then placed in a FIFO aisle, waiting to be opened for individual verification of the products delivered. The reels are then scanned into the logistics system and assigned a Continental product number, placed in standardized size Continental trays, and conveyed to the component store, known as the *Quickstore*.

Between a component delivery and its entry into the *Quickstore*, it takes an average of 24 to 48 hours for the reels to be handled by an operator.

In the *Quickstore*, components are stored in trays depending on the component reference and date of receipt of the batch. These trays are arranged on shelves to which the automatic dispensing system has access. When *Quickstore* operators call for a particular component reference, the trays are automatically supplied to them by the dispensing system. Prior to supplying the production line with the components, the operators "beep" the reels again to update the logistics system, and place

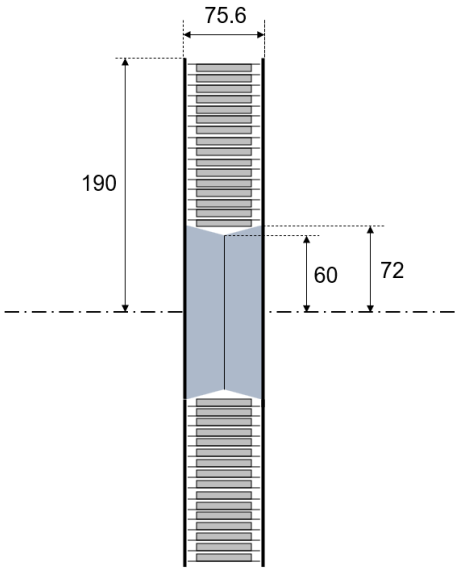

Figure 1.19: Reel geometry and dimensions (example given here for the LAIRD shield reel). Dimensions in mm (scale not respected).

them on rolling shelves, which they then transport to the lines.

The C.E.M.S. workshop, which is in charge of the current production of the BSRF EA electronic board, calls up stocks according to production requirements and the final storage space available.

Quickstore logistics operators deliver the requested stock to the storage shelves along the production lines.

The production operators then take over and position the reels in the rack corresponding to the product configuration.

In this way, between the arrival of the trays at the *Quickstore* and the positioning of the reels in the rack of the placement machine, the reels have been handled by an operator at least 3 times.

They can, however, be further reduced by grouping and/or inventorying:

- Grouping consists of combining the contents of two (or more) partially filled trays into a single tray. In fact, if the same delivery of components has been divided between several trays, the system can call up one or the other tray, provided the delivery date is identical. Grouping thus serves to optimize component storage within the *Quickstore* and requires an operator to handle the transferred reels.
- Inventory is carried out on the line shelves, by the production operators, if they deem it necessary to update the inventory of components available on the line. To do this, they have to take each reel off the shelf one by one and scan them again.

Placement process

The placement machines used at Continental Automotive France are SIPLACE machines from ASMPT, a reference in the field of component placement. As there are many different reel sizes (widths), ASMPT offers just as many different feeders, adapted to the dimensions of the corresponding reels and the components they contain.

In the case of the LAIRD shield, the strip width is 72 mm (84 mm for the other shield). The feeders adapted to these tapes are among the largest used at Continental Automotive's Toulouse site.

The mechanical operation of a feeder is similar to that described in the kinematics diagram in Figure 1.9.

The end of the feeder simultaneously removes the protective film when the tape is driven forward, which exposes the component, as shown in Figure 1.20.

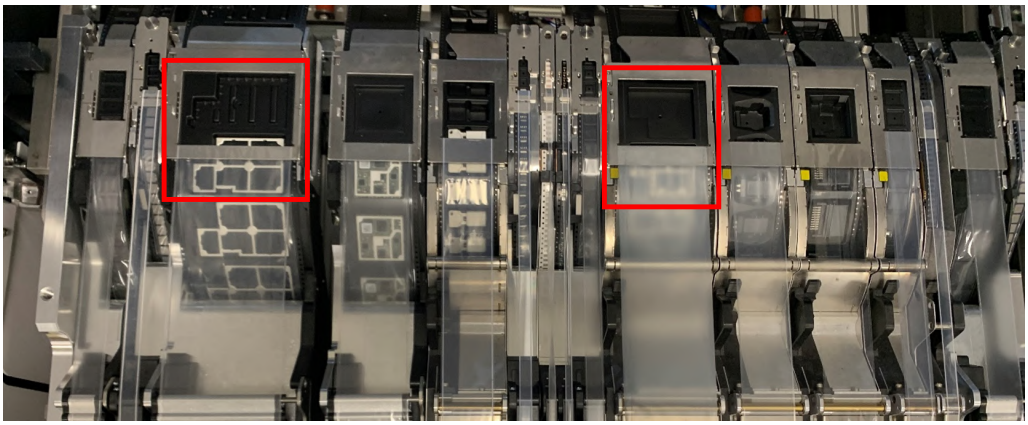

Figure 1.20: Top view of the feeders, peeling off the protective film and exposing the components for pick and place. Inset in red: The tape compartments of the two shields on the underside of the BSRF EA.

One of the nozzles fitted to the placement head is positioned on the EMI shield so as to place the suction points in the areas provided for this purpose ("D" areas on the isometric drawings in Figures 1.15 and 1.16).

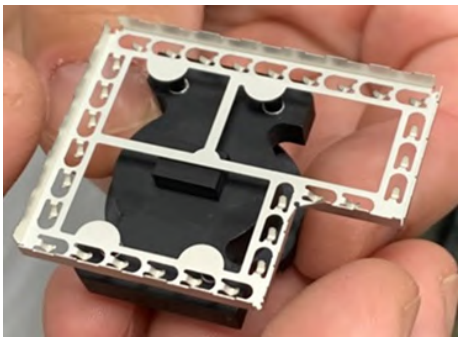

Figure 1.21: LAIRD shield with matching suction nozzle

The head then applies a standard pressure of 2 N, followed by a vacuum from the nozzle, which sucks up the component, allowing the shield to be transported from its tape compartment to its exact position on the PCB. It is also possible to set the placement machine to perform a pre-vacuum, i.e. to start vacuuming even before contact with the part. The part itself is then sucked up and pressed against the nozzle.

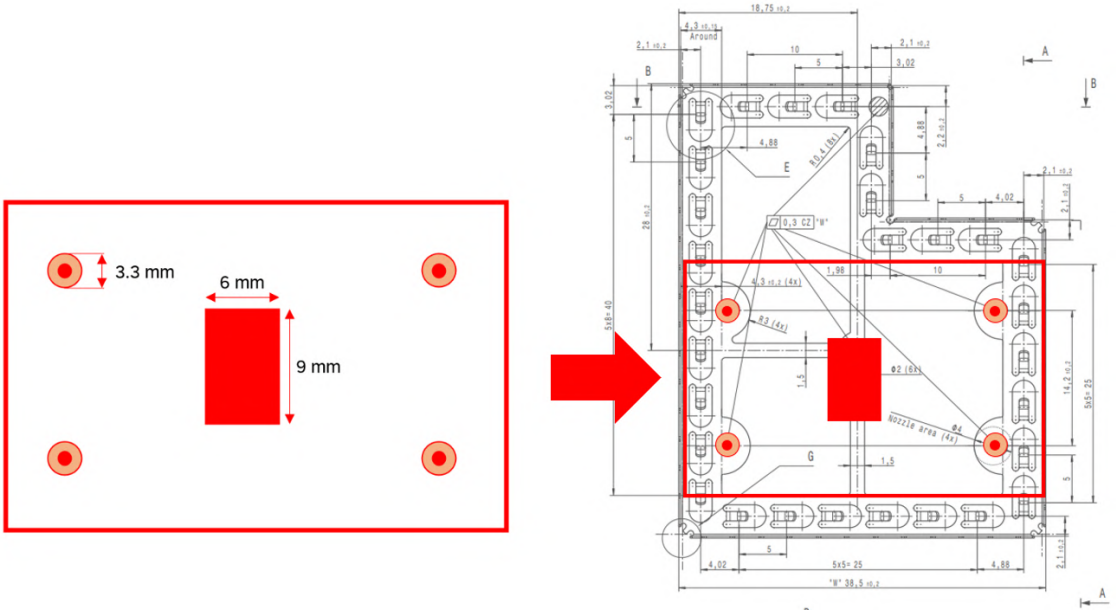

Figure 1.22: Dimensions and positioning of the suction pipette for the LAIRD shield. There are 4 suction points corresponding to the "D areas" highlighted on the part drawing (Figure 1.16)

Once the cage has been positioned over the PCB, the placement head accompanies the plunging of the cage into the layer of solder paste deposited on the PCB during the screen-printing stage. In doing so, the placement head applies a slight force, also with a minimal value of 2 N, to the "D" areas. In contrast to the gripping phase, it is impossible to adjust the placement machine to avoid the force applied during the application/plunging phase.

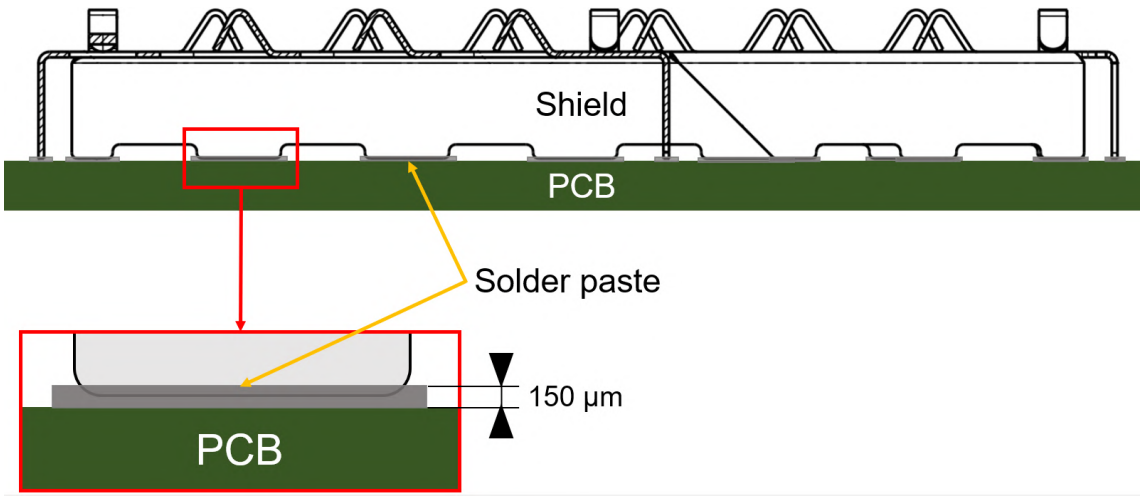

Figure 1.23: Cross-section of LAIRD shield illustrating the plunging of fixations into the solder cream layer during pick-and-place.

The solder paste thickness of the layer applied during screen printing (by the use of a stencil, see Section 1.2.2) varies according to the product. It is set at 150 μm for the underside of the BSRF EA card, as shown in Figure 1.23.

Reflow soldering

The oven is a crucial stage in PCB assembly, as it enables all components to be fixed to the PCB via the reflow process: exposure to the oven's high temperatures causes the soldering of the components' electronic terminations (pins); see Section 1.2.2.

In this particular case, the soldering is done with the base of the shield, made up of the 31 contact pins provided for this purpose, visible in Figure 1.23 above.

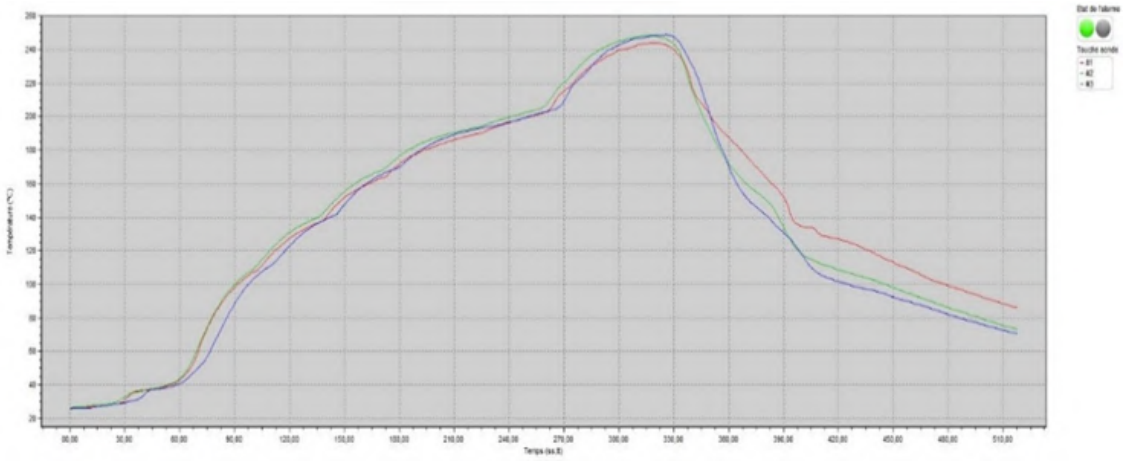

Figure 1.24: Temperature profile measured during reflow validation for BSRF EA (lower and upper sides). This is the actual temperature experienced by the PCB when the temperature setpoint profile is applied (stages corresponding to the different oven zones).

Conveying through the oven is set to a speed of 800 mm/min, and the PCBs go one by one through the various oven compartments, which are set to a precisely defined temperature, and the PCB temperature thus follows the profile shown in Figure 1.24.

As explained in the SMD line principle (section 1.2.2), on leaving the oven, the panels are conveyed into a rack where cooling is continued simply by convection of air at ambient temperature. The rack has a capacity of 16 panels, although in practice around 5 panels are held there at any time. The rack operates on a FIFO (First In, First Out) basis, and the storage and cooling time for each panel is defined at 120 s.

The entire process of packaging, supply, and assembly on PCBs is summarized in the Life Cycle Analysis section (2.1.3), providing a better overall understanding.

Chapter 2

Critical analysis of the issue

2.1 Manufacturing defect characterization

2.1.1 Overview

The problem to be addressed by this study is the following:
Deformation of the LAIRD shield, leading to its poor mounting, is observed when the PCB panels come out of the SMD line. This is because the shield must be fixed to the PCB all the way around its base, to ensure proper protection against EMI (see Appendix A). To achieve this, flatness (plane A of Figure B.2) must be ensured during pick and place and reflow. On the parts concerned, the line output shows disbonding between the PCB and the shield mounting lugs in the lifted areas. An in-depth description of the deformations, which is the first step forward in this study, will be given in section 2.1.2.

The deformation problem was reported to the supplier prior to the start of the study, aiming for a claim on quality requirements impeding by the supplier. The latter rejected the report because the deformations measured were consistent. In fact, their measurements were within the flatness tolerance (0.2 mm). It should be noted that 100% of the supplier's measurements on a series of components were taken after the parts were manufactured and before they were packed.

Thus, the situation at the start of the study is as follows:
The flatness tolerances (0.3 mm on the top, Figure 1.16, and 0.2 mm on the bottom, surface A Figure B.2) are respected according to the measurements carried out by the supplier at the end of the manufacturing process. However, a significant flatness defect is observed at the output of the SMD line, on a consequent number of parts.

2.1.2 Description of the observed deformations

Some deformations have been observed on the MSA shield, appearing suddenly on a series of PCBs, grouped and randomized over the production run. However, these deformations are very rare and do not have a typical typology, unlike the majority of deformations observed, which concern the LAIRD shield exclusively. They are therefore considered as accidental special cases, unlike the usual deformations described here on the LAIRD shield.

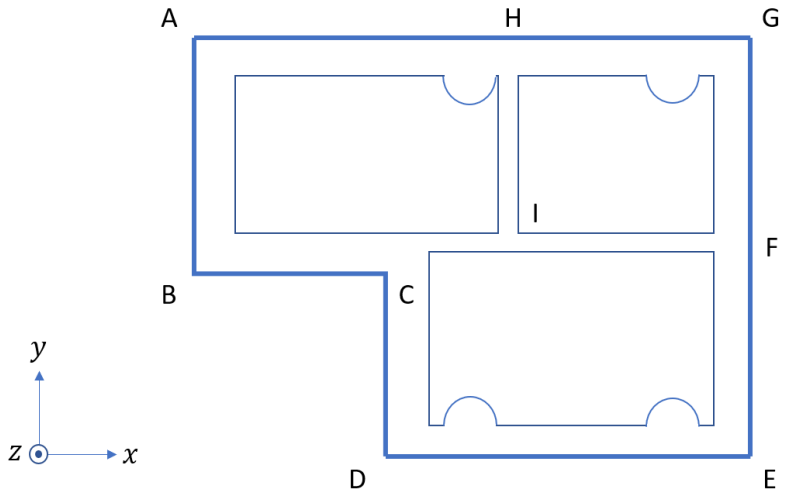

Figure 2.1: Overall formalized geometry of the LAIRD shield

To clearly describe the occurring deformations, it is useful to formalize the overall geometry of the LAIRD shield as shown in Figure 2.1.

Based on this geometry, we can proceed with a detailed characterization of the deformation and disbanding (or delamination) typologies observed during repeated observations of BSRF EA production (PCB underside assembly). This characterization leads to the classification of deformation types into four different modes. It should be noted, however, that the classification is not guaranteed to be an exhaustive representation of all possible deformations, but it does include all the deformations identified in this study.

The amplitude of the deformation observed was classified on a scale from 0 (indiscernible) to 5 (very pronounced).

- **Type 1:**
  Corner B is lifted, causing the broken segment [ABC] to arch in the z-direction, and the shield base to fail to contact the solder paste (no soldering) in the vicinity of segment [BC]. This results in non-parallelism of segment [AB] with the PCB plane. In the case of medium (3) to very pronounced (5) deformation amplitude, the entire segment [BC] can be lifted, and the buckling then propagates to corner D. This also results in non-parallelism of segment [CD] with the plane of the PCB. In the case of very slight (1) or even indistinguishable (0) to slight (2) buckling amplitude, the shield-PCB contact is sometimes preserved, but with a very weakened solder joint, indicating poor reflow.

- **Type 2:**
  Raising of corner D, and non-contact of shield base with solder paste (no solder) in the vicinity of corner D. This results in non-parallelism of segment [DE] with the PCB plane.

- **Type 3:**
  Lifting of the entire broken segment [BCD], and non-contact of the shield base

with the solder paste (no soldering) in the vicinity of corners B, C, and D. This results in non-parallelism of segment [DE] with the PCB plane.

- **Type 4:**
  Uplift of corner A, and non-contact of shield base with solder paste (no soldering) in the vicinity of corner A. Uplift extends to corners B and G. This results in non-parallelism of segments [DE] and [GA] with the PCB plane.

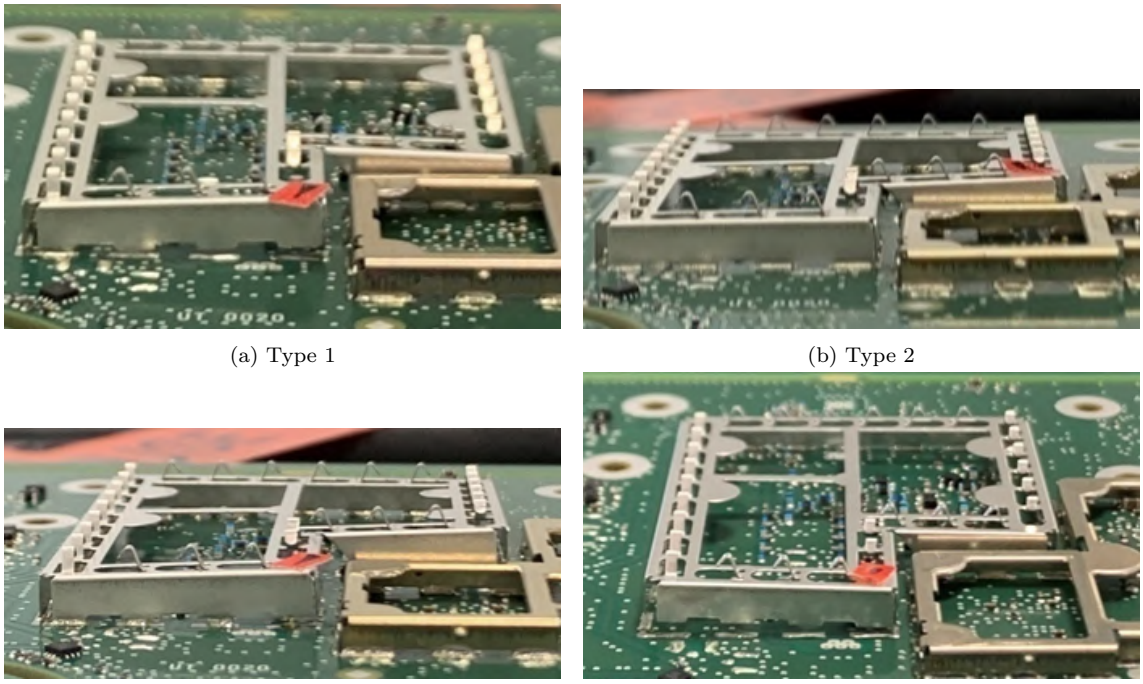

(a) Type 1

(b) Type 2

(c) Type 3

(d) Type 4

Figure 2.2: Examples of each observed deformation tyoplogy

On the SMD line in normal operation, defects are not detected until the final inspection. In particular, the EMI cage deformation defect requires 100% visual inspection by the operator, i.e. on all parts leaving the line. AOI visual inspection tools are limited in their ability to detect this type of defect, which is still new to production and concerns only the EMI shielding components on the underside of the BSRF EA.

In parallel with this study, the quality department of the C.E.M.S. workshop has been able to work on the development of an AOI vision whose role is to detect the deformation of these shields. This is an invaluable aid for rejecting defective parts at the end of the SMD line, but provides no additional information for locating the origin of the defect and thus limiting its consequences. This is why a study involving in-depth observations of the production process is necessary.

2.1.3 Shields' life cycle assessment

To summarize all the actions EMI shields have undergone since they were manufactured, and thus provide a clear picture of all the events likely to have an impact

on their integrity, let's illustrate the portion of interest in the life cycle of these components. This extends from the end of shield manufacturing by the supplier to the moment when the defect is reported, i.e. AOI control on the SMD line at Continental Automotive France.

Focus is given to the post-production processes because, as explained earlier, the supplier has verified (on an admittedly limited series) conformity with specifications once the parts have been produced. The packaging method (T&R) and the quality instructions mean that the parts are inaccessible from the moment they are packaged.

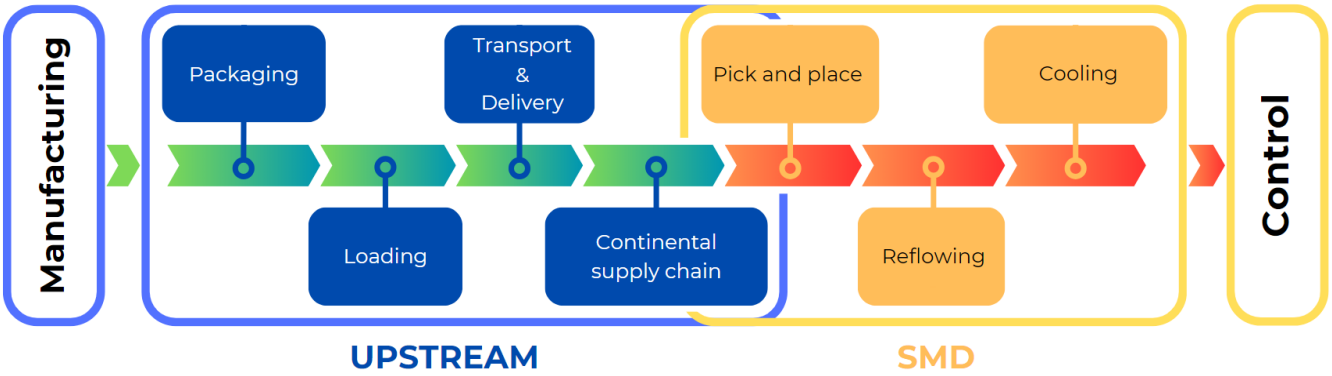

Figure 2.3: Shield life cycle limited to the phase of interest for problem identification. Synthesis of logistics and assembly processes.

Here, it is crucial to distinguish stages during which parts are individually inaccessible to inspection, and stages between which inspection is possible. The entire upstream phase is thus characterized by the opacity of processes concerning the impact they may have on damage to parts. In contrast, during the SMD phase, it is possible to observe and control the integrity of the shields on sight. This can be done during the fault-finding stage.

2.2 Research strategy

2.2.1 Introduction to the 8D approach

The 8D (8 Disciplines) method is a structured approach widely used in industry to solve quality problems effectively. It enables problems to be identified, analyzed, and resolved systematically, with an emphasis on collaboration, rigorous analysis, and continuous improvement. In the industrial world, 8D provides a clear and coherent framework for working teams to help them resolve certain complex problems or those whose origin is difficult to identify, by relying on specific steps that guide them through the resolution process.

The following 8 steps provide the skeleton of the resolution method:

D1: Assemble a team.
D2: Define the problem.
D3: Implement emergency measures (palliative, to protect the customer).
D4: Identify root cause.
D5: Define corrective action plan.
D6: Implement the corrective action plan and evaluate its effectiveness.
D7: Implement preventive actions.
D8: Evaluate work, debrief, and congratulate the team.

In the classic 8D scheme, steps 1D to 3D must be completed within 24 hours of the problem being detected or reported.

In this case, the first action taken was 3D (protecting the customer and reducing the occurrence of the problem "with the means at hand"). The 1D stage was dealt with in the following months (the creation of the problem-solving team being my recruitment as an intern at Continental Automotive), and the 2D stage was dealt with in the first few weeks of my internship.

Thus, the perennial resolution of this production problem can be characterized by an 8D method more spread out over time than the classic scheme.

In addition, the 8D method is designed for problems that have arisen as a result of customer dissatisfaction (it's a Customer Complaint Management method), i.e. an undetected problem that has gone unnoticed during the inspection stages and that has been delivered to the customer with the defect. Here, since the first identification of the defect, which has proved to be recurrent, visual detection has taken place and the parts concerned are systematically scrapped. Thus, we will not consider the parallel study dedicated to resolving the non-detection of the problem. In addition, the C.E.M.S. workshop's quality teams have been working on an automatic detection system for soldering defects (non-contact of the shield with the PCB), which, in most cases, reflect the deformation (non-planarity) of the shield.

The comparison with the 8D method will therefore focus on explaining the origin of the problem and the approach to solving it. In other words, from an 8D point of view, the aim of this study is to scan stages D2 to D5.

Step D2 has been completed: the problem has already been defined, with a precise description of the deformations involved, characterizing the production problem encountered.

There's no need to dwell on D3, which has been handled directly by the production teams in order to react quickly and remedy the defect as far as possible.

All in all, this is a methodological formalization for this type of problem-solving, which will be natural to follow in this study.

2.2.2 Application of the method for root cause identification

The search for the root cause, in production engineering, corresponds to step 4 of the 8D methodology described above.

In theory, there is a list of preliminary steps to applying the 4D methodology:

- Ask why the fault was not detected.
- Ask why the problem was not anticipated (FMEA process: Failure modes and effects analysis).

Despite the crucial importance of these questions, their applicability in the context of this study is nevertheless limited (as explained above), firstly because the defect is detected here, and secondly because the anticipation of the problem can be questioned more legitimately at a later stage, once the "mechanical" root cause has been identified and resolved.

The systematic root cause methodology contains two main tools: the Ishikawa Diagram, and the 5-why method.

The principle of the Ishikawa diagram (also known as the fishbone diagram) is to list all the potential causes that could contribute to the defect, separating them into 5 areas (Materials, Process, Environment, People, Equipment).

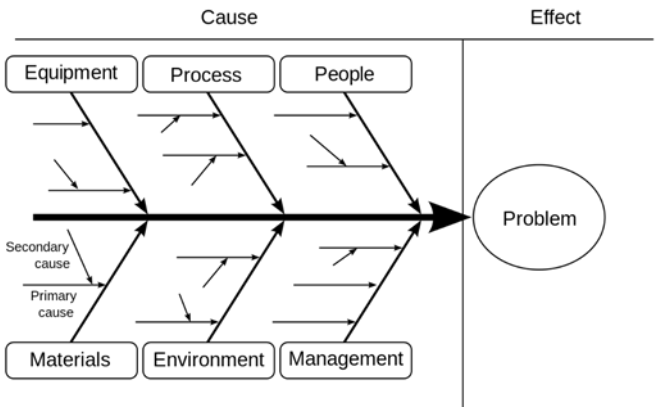

Figure 2.4: Ishikawa (or fishbone) diagram principle

It should be noted that it is possible to find in the literature 4 or even 6 groups of causes: we will apply the method used at Continental Automotive, with 5 branches.

Once the Ishikawa diagram has been drawn up, the potential root causes need to be validated by means of research fuelled by scientific reasoning. In this case, the potential causes linked to a mechanical phenomenon will call for a validation process involving mechanical testing, fault reproduction, and simulation of each potential

root cause studied.

For this purpose, it's common to draw up DOEs (Design of Experiments). Mastery of DOEs is a useful tool for effectively tracing the root cause: it allows bypassing individual parameters during experiments, while still arriving at a valid and interesting conclusion. However, it is not a prerequisite.

The Ishikawa diagram suggested here (Figure 2.5) is intended to take into account any process or phenomenon occurring in the shield's life cycle, upstream of the first AOI, and whose interaction with the shield could possibly contribute to the observed defect.

Potential causes have been separated on the basis of their technical nature, and therefore their accessibility for treatment within the scope of the present work.

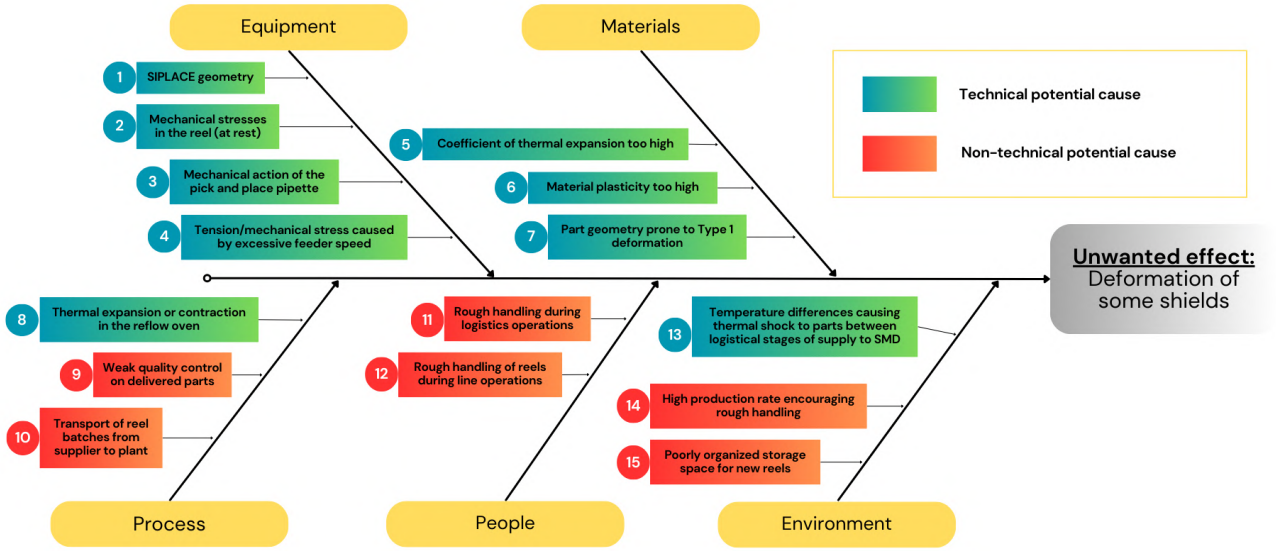

Figure 2.5: Ishikawa diagram proposed as a basis for finding the root cause of the deformation observed on EMI shields.

It is possible that two potential causes classified in two different categories present a redundancy in their contribution to the defect, and are in fact linked by a cause-and-effect relationship. For example, it is quite possible to imagine that causes 14 and 15, linked to the environment in which production takes place, are the origin of cause 12, which relates to people.

Similarly, we must not rule out the possibility that several factors listed in the potential causes may contribute in parallel to the appearance of the observed fault, with different levels of importance. For example, if the validated root causes are potential causes 2, 4, and 7, they act in concert to produce the fault, and the solutions

that may resolve them will not necessarily be redundant.

For all these reasons, starting from the potential causes listed in the Ishikawa diagram, it will be necessary to trace back to a minimum number of causes that may give rise to the factors considered on the diagram, which in turn will cause the observed defect. If these original causes still have a physical content that allows for a conceivable technical resolution, they must be tackled in order to provide a technical solution to the problem at hand.

In this way, we can rethink and refine the Ishikawa diagram, redefining the causes by grouping together as many technically treatable potential factors as possible (see Figure 2.6).

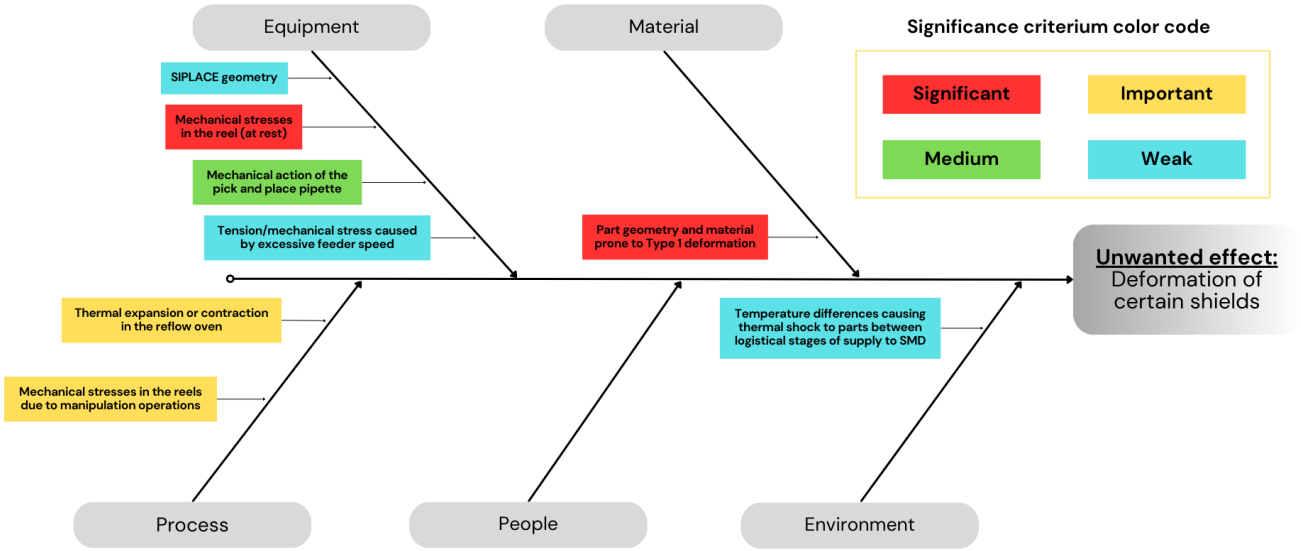

Figure 2.6: Simplified Ishikawa diagram, listing potential technical causes in order of importance

Here, the selected causes have been sorted by order of importance. This discrimination was based on the field observations and will be justified by the resulting analyses. A different numbering assignment is also made based on this importance criterion.

The last theoretical stage of 4D involves the "5-why" method. For the root cause(s) validated, this involves tracing the fault's "path of occurrence", by asking the question "Why is this happening?" successively at least 5 times, which amounts to transforming each root cause into an effect of a deeper, and therefore more systemic, cause. This helps to find a root cause that can be solved to treat the problem sustainably, and potentially prevent other issues, related to similar subjects or depending on the same parameters.

This method often questions upstream processes that go beyond technical aspects.

It is therefore legitimate to question the relevance of this method for the technical problem addressed by this study. Indeed, the ambition for this work is limited to the technical resolution of the shield deformation problem. This remains compatible with a broader approach to solving similar problems encountered on the electronic board production line. In this case, we could consider a complementary study aimed at tracing the problem back to a more general root cause: anticipation, component sourcing, or even a design philosophy that takes account of packaging and logistics constraints at the same time as component design.

2.3 Field data collected during production

2.3.1 General observation

For a complete study of the defect's appearance on the SMD line, several series of observations were carried out during production runs, corresponding to the assembly of the underside of the BSRF EA. For each of these observations, it was ensured that the instructions (Poka-Yoke[1] type) given to the operators were respected, i.e. the prohibition of tape splicing[2] for EMI shielding components, as well as the mounting of their reels on a mobile axis allowing rotation of the reel without tape tension, which would be due to friction between the reel and the rack (a factor amplified by the consequent weight of these reels).

A first observation, on a global level, aimed to identify the presence of the defect on the shield, in order to constitute the description seen above, and also to characterize parameters related to the defect's emergence.

In this case, the aim is to identify whether the temporal distribution of part assembly shows a concentration of deformed shields among those coming from a certain portion of the reel (beginning/middle/end). It is indeed legitimate to imagine that the increased curvature of the final/central portion (last tape layers) of the reel is likely to cause the components to warp, in the direction observed (see Figure 2.7).

The first hypothesis we set out to formulate and verify was thus the correlation between the end of the reel and the occurrence of deformations.

[1]Literally "error-proofing" in Japanese, it was first introduced in Toyota factories in the 1960s and aims to limit inadvertent errors during handling processes. It uses instructions, symbols or signs intended for operators.

[2]Tape splicing is a technique used for most electronic components, which consists in splicing the beginning of a new tape to the end of the previous one, to avoid temporarily stopping the line when changing reels.

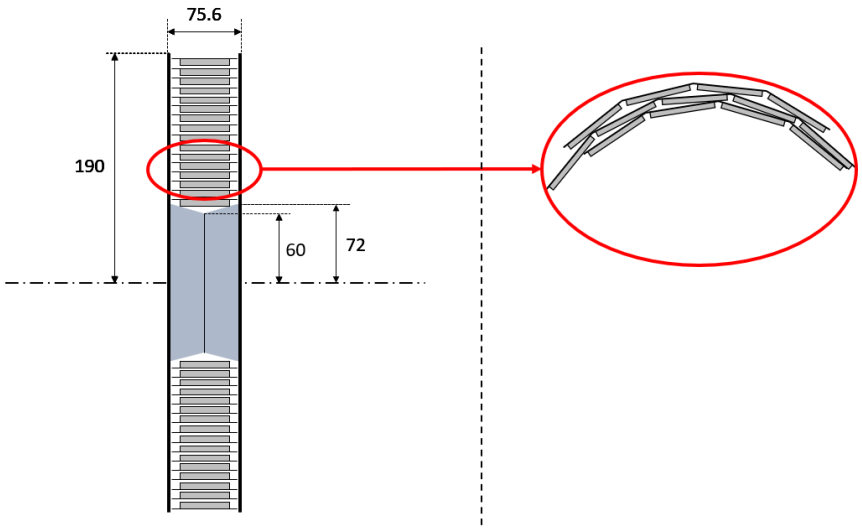

Figure 2.7: Potential effect of curvature on tape layers close to the reel center: winding direction favoring component warpage.

Defect type	Type 1	Type 2	Type 3	Type 4	Total	% Total
Manufactured parts					500	100
Scrapped parts	18	1	2	0	21	4.2
Manufactured panels					250	100
Scrapped panels	14	1	2	0	17	6.8

Table 2.1: Results of the first general observation, from parts' and panels' point of view.

The data from the first analyzed production run is as follows:

Out of 500 parts produced, 21 showed a geometrical defect on the LAIRD shield, compromising its correct installation on the PCB, corresponding to a defect rate of 4.2%. Of these defects, 18 were type 1 (see Figure 2.2a), representing 3.6% of the total number of installed LAIRD shields.

From the defect identification and tracing table (Figure 2.8), it was possible to recreate the production chronology (Figure 2.9).

Thus, this first global observation[3] of a 500-units production run leads to the conclusion that the defects (mainly type 1) observed on the EMI shiels are mostly present on the last components of the reel. Furthermore, the only defects identified on shields originating from the beginning of the reel are unusual deformation types, namely types 2 and 3.

[3]In fact, this was the 2nd observation carried out. The first observation, less significant in terms of parts produced, had resulted in 10 scraps caused by shield deformation (i.e. 2.6% of production), 9 of which came from the end of the reel (i.e. 90% of defective shields).

Type de défaut	Amplitude défaut		BISAC SIPLACE	BISAC four
1		3	18h02	18h09
1		3	18h02	18h09
1		1	18h02	18h11
1		1	18h11	18h17
1		4	18h12	18h18
1		4	18h12	18h18
1		5	18h18	18h31
1		4	20h08	20h17
1		3	20h20	20h28
1		4	20h20	20h28
1		4	20h21	20h29
1		3	20h28	20h35
1		3	20h29	20h36
1		3	20h29	20h36
1		3	20h35	20h42
1		4	20h36	20h42
1		2	20h47	20h53
3		5	20h52	21h04
3		5	20h54	21h06
2		4	20h57	21h08

Figure 2.8: Defect identification table. This table was used to monitor production, enabling defects to be traced and characterized.

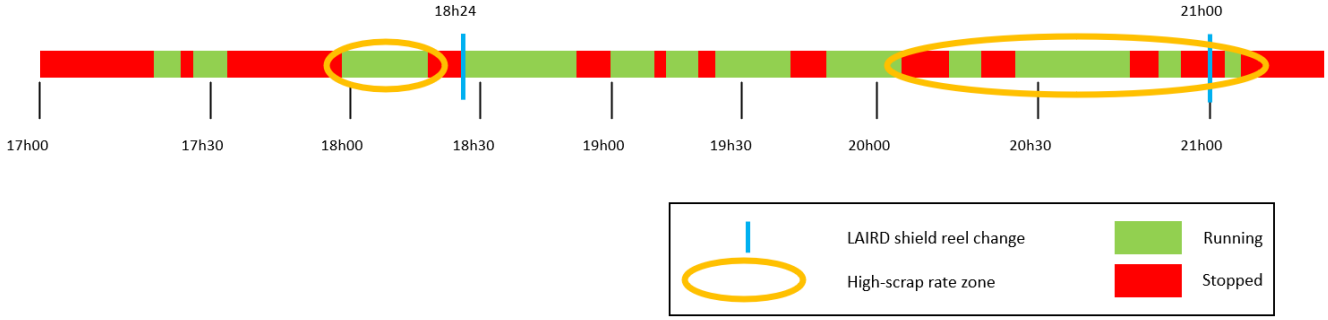

Figure 2.9: Production timeline. Information on the (SMD 4) line's running and stopping periods was entered via internal production support software, including traceability of parts produced.

A statistical analysis carried out during a subsequent production run produced the following results:

		Total	% of production	% of scraps
Total Scraps	Parts	23	9.2%	100%
	Panels	16	15.1%	100%
Scraps due to warped shield	Parts	13	5.2%	56.5%
	Panels	9	7.2%	56.2%

Table 2.2: Statistical information on scraps number, differentiating parts from panels, from general observation during a subsequent production run

The defect rate (from the parts' point of view) is consistent with what has been observed previously (around 5%), as is the scrap participation of around 60%.

For the following observations, it will be advisable to give a quantitative definition of the "end of reel". Let's assume for now that the end of the reel designates its last 20%.

The correlation between type 1 defects and the end-of-reel occurrence can therefore possibly be confirmed by the following observations. This observation will have to be supported by a more in-depth study to validate or exclude causality (factors 2, 4, and 7 of the Ishikawa diagram shown in Figure 2.5).

Indeed, if confirmation of the correlation hypothesis is only supported by other observations pointing in the same direction, no causal link can be established and proven without a methodical demonstration of the root cause.

2.3.2 Localized observations

Let us use the chronology established in the life cycle analysis limited to the phase of interest for fault-finding (Figure 2.3).

The stages accessible to observation are those constituting the passage on the SMD line (placement, reflow, and cooling).

By making observations between each stage of the process, the aim is to identify defects at various points on the line, in order to monitor their evolution and thus study the influence of SMD actions on part integrity. The underlying goal is to trace the presence of the defect as far back as possible on the line. Indeed, the root cause of the defect is what is ultimately searched, and it goes without saying that if a defect is identified on the line, the root cause occurs upstream of the place of observation.

Observation of parts between placement and reflow

Since the earliest observable production phase is placement, a privileged position for observing shield deformations is at the placement machine exit, just before the panels enter the reflow oven.

It should be noted that for all observations made between 2 SMD production stages, the accuracy of these observations was limited by the visual analysis conditions: observations were carried out while parts were being conveyed between two production stages, sometimes with a temporary halt to the conveyance to enable better observation, but sometimes on moving panels. It should also be noted that, when parts are on the SMD line, it is forbidden, for quality reasons, to touch the part or pick it up for closer observation of the components.

In the case of this observation, defects were indeed identified during the observation at the placement outlet.

Although this observation proves that the origin of the deformation predates reflow, it is interesting to compare the observations made before the oven inlet and at the end of SMD. In doing so, we focus on factor 8 (Figure 2.5), which leads to the formulation of hypothesis 2 below.

Hypothesis 1: Shields from the last 20% of a reel lead to the majority of deformations, visible as early as the placement stage.

Hypothesis 2: Scraps justified by shield deformation are due to an initial deformation present before reflow, which prevents the solder paste from setting (plunging of the shield base into the solder paste, see Figure 1.23). Deformation may be amplified during subsequent steps (reflow, cooling).

		Total	**% of production**	**% of scraps**
Total Scraps	Parts	34	7.6%	100%
	Panels	22	9.9%	100%
Scraps due to warped shield	Parts	21	4.7%	61.8%
	Panels	16	7.2%	72.7%

Table 2.3: Statistical information gathered from localized observation between placement and reflow during a production run.

The summary table above shows that shield deformations, of type 1 in the vast majority, account for around 2/3 of rejects (61.8%), representing around 5% of parts produced.

At the time of this analysis, no AOI device had been implemented to recognize this defect. All parts were therefore visually inspected, and the EMI shields were checked on the basis of the following quality criteria: The soldering (meniscus) must be perfect on the fixing lugs which are present all around the component, at its base. Parts not meeting this criterion are scrapped[4].

In some cases, the reflow process leads to acceptable soldering quality, even though observation at the placement outlet shows a small amount of deformation, but enough to compromise the plunge of the shield base at corner B. Although these parts are not scrapped, they are of interest for the study of shield deformations. However, it is not possible to observe the evolution (amplification) of deformations on these parts as they exit the line since they are not set aside for later analysis.

This phenomenon, where parts show extremely small deformation without causing a defect at the end of the line, only occurs on shields that do not come from the end-of-reel region (as defined earlier: the last 20% of the reel).

Below (Figure 2.10) is a column taken from the defect tracking table constructed upon observation between placement and reflow. It gives the percentage of components remaining in the current reel, i.e. the position of the component within the reel (in % of the reel, 100% symbolizing the position of the first component and 0% the position of the last one).

[4]No quality criteria have been established for shield deformation: this is not prohibitive as long as the solder joint has no defects. As we have seen, the deformation phenomenon is more difficult to qualify than the soldering quality, due to the continuous nature of the possible deformation amplitude.

The components that showed no defect at the line outlet, but that had shown a slight defect at the observation location, have been marked with a red border line. The slight defect mentioned here means that the deformation amplitude is less than 1/5 and that the deformation is visible only because of the abnormal plunge in the solder paste (see representation below, Figure 2.11).

In this case, it would appear that the most raised anchor bracket (on the right of the diagram) remains sufficiently close to the solder paste surface for reflow to take place correctly. Thus, if we eliminate these "borderline" cases (see Figure 2.10b), it becomes striking that type 1 defects appear unanimously on the end of the reel (last 20%).

Another conclusion to be drawn from this observation is that a significant proportion of these parts show an amplification of deformations at the end of the process, which must then occur during the post-placement stages (reflow, cooling)[5].

Another rare phenomenon has been observed: on occasion, the solder joint is not correctly made at corner B after reflow, although no deformation is apparent to the naked eye. This shows that, despite a common soldering defect appearing on the most deformed parts initially, defects can appear in the same place (corner B) even though no deformation is discernible.

Precise measurements will enable us to estimate the flatness of these parts, indicating the presence or absence of Type 1 deformation. Given the low amplitude of these deformations (if any), we might also ask whether an initial deformation of the shield is the only factor that could explain these cases of poor soldering. Another hypothesis will be explored in section 2.5.

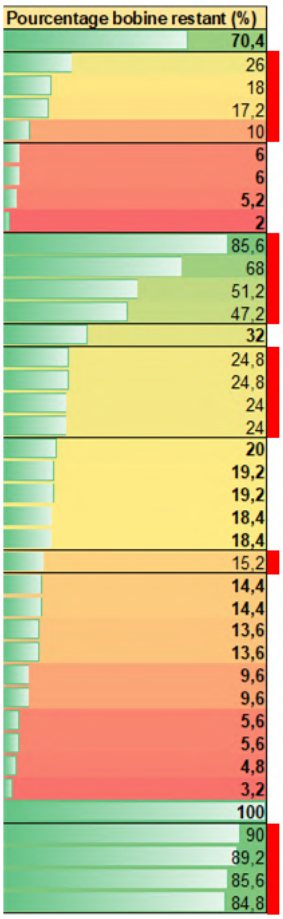

(a)

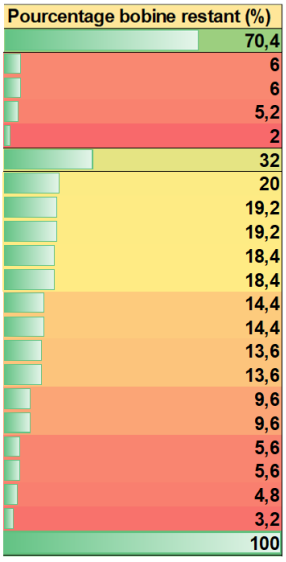

(b)

Figure 2.10: Positions displaying a defect upon observation (a), and after filtering out false defects at line output (b), in% of the reel.

[5]This amplification of deformations can be studied as a consequence of aggravating causes that should be identified at a later stage, outside the framework of the search for the defect's root cause.

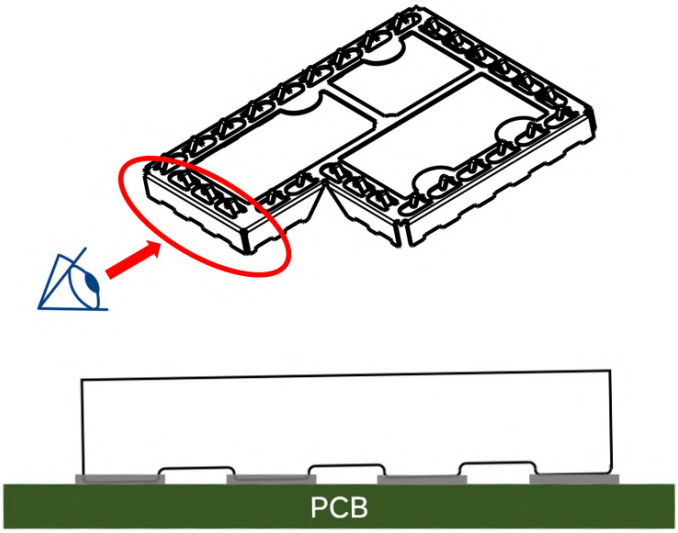

Figure 2.11: Common slight shield deformation resulting in uneven plunging of AB segment into the solder paste.

Observation of parts between reflow and FIFO (end of cooling)

When the parts exit the reflow oven, most of the cooling process has already been carried out: the parts' temperature is relatively low, depending on their "thermal mass"[6]. The FIFO's main role is to store parts and regulate the flow for the AOI. It is fair to assume that there will be limited interest in observation between the oven outlet and the FIFO. Nevertheless, we are careful to remain as impartial as possible and to carry out all possible observations with the same rigor. This ensures that no possibility is overlooked that could prove decisive for the study.

However, during a subsequent run, the comparison of parts observed at this stage with scrapped parts at the end of the SMD line showed no significant difference.

[6]Jargon used (especially in the building industry) to describe a property similar to the thermal capacity of a part. Also known as thermal inertia.

2.4 Root cause hypothesis

2.4.1 Partial conclusions drawn from field data

The field data summarized above allows us to draw the conclusion that type 1 deformations appearing on LAIRD shields originate from a root cause that enters into play prior to the SMD reflow stage, where panels enter the oven.

In the context of this study, the supplier's assertion that all the parts respect the tolerances upon manufacturing - which has been justified by measurements on a series of parts, as explained in section 2.1.1 -, will not be questioned for the sake of providing a solution-oriented study within the reasonable amount of time granted, and with the data at hand.

Given the hypotheses considered, the initial defect could only be inflicted on the shields during intermediate steps happening between component packaging on the supplier's site and observation made at reflow oven entry on the SMD line. A convenient visualization of this is made available by the life cycle analysis carried out earlier in the study (section 2.1.3). These steps include manipulation for truck loading, transport, manipulation upon delivery at the Continental site, manipulation for Quickstore loading, manipulation for line supply, and the pick and place SMD stage.

Several hypotheses can therefore be considered for the root cause of shied deformations. According to the Ishikawa diagram suggested earlier (2.6), the most plausible origin for the problem is mechanical. Indeed, the importance criteria were based on the observation of all aspects of production. In this case, some deformation imprinted on the packaging alveoli (or compartment cells) was visible from the side of some reels, giving priority to the hypothesis of mechanical deformation of parts inside the reel for root cause identification. This visible packaging deformation is shown in Figure 2.12.

Figure 2.12: Deformation of packaging compartments (circled in red) visible from the side of the reel.

This priority hypothesis is reminiscent of the idea formulated in Section 2.3.1 and illustrated in Figure 2.7: The loading conjecture that will be theorized and tested is identified as the consequence of tape layers' stacking coupled with the tape tension and augmented curvature imposed by the neighboring reel center.

Other potential factors in line with the conclusions on the product's life cycle will be assessed. However, they fail to show sufficient material to enable consideration as the most plausible root cause.

2.4.2 Intra-packaging mechanical loading conjecture

In order to prepare a thorough study of the impact of reel packaging on the shields explaining their deformation, it is highly relevant to firstly carry out a preliminary study, using a rough model to characterize in a broad outline what happens when a load is applied to the part, modeling the stress experienced in the packaging.

In that preliminary study, the model undergoes a bending load in the direction that matches the reel winding. The aim is to extract a rough value of deformation (or an order of magnitude) resulting from the application of a load to this simplified structure, using tools from the theory of deformable solid mechanics. This load case is very practical because it is easy to recreate with the real part in a mechanical test lab (see Section 3.4), which allows a great possibility of comparing theoretical projections with reality. Indeed, this load case imitates the action of a compression tool applying a force due to mid-width line contact with the part.

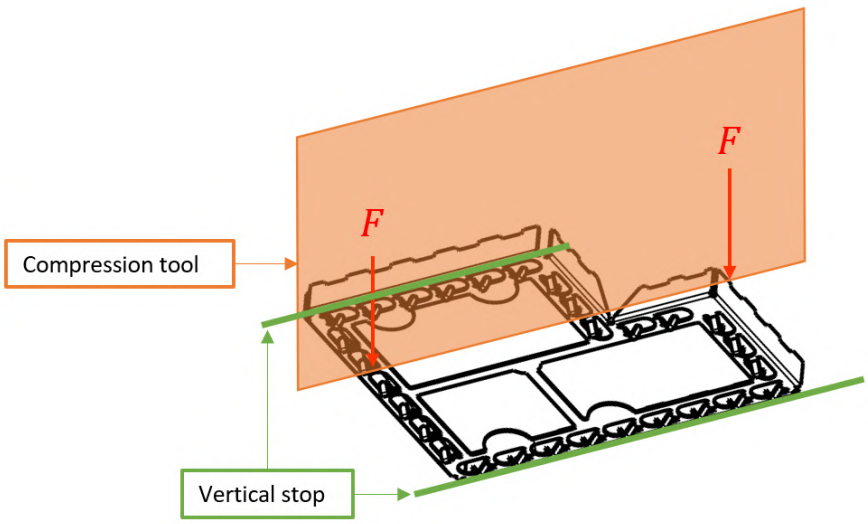

Figure 2.13: Load case studied for preliminary calculation

For a matter of simplification, the model established consists of treating the 3D problem as the superposition of two 2D problems, one in the (Oxy) plane and the other in the (Oyz) plane. This separation into sub-problems justifies the new simplified, overall structure considered, shown in Figure 2.14, which is thought of as equivalent to the structure of the angular side of the shield (AD segment in Figure 2.1). We then estimate f, the total deflection of the point undergoing loading F, by summing the deflections f_1 and f_2 of the beam assemblies making up the two sub-problems (see Figure 2.15).

Each segment (between two points of Figure 2.14) will be modelized as a beam, using one of two section types as shown in Figure 2.16: L-shaped section, and rectangular

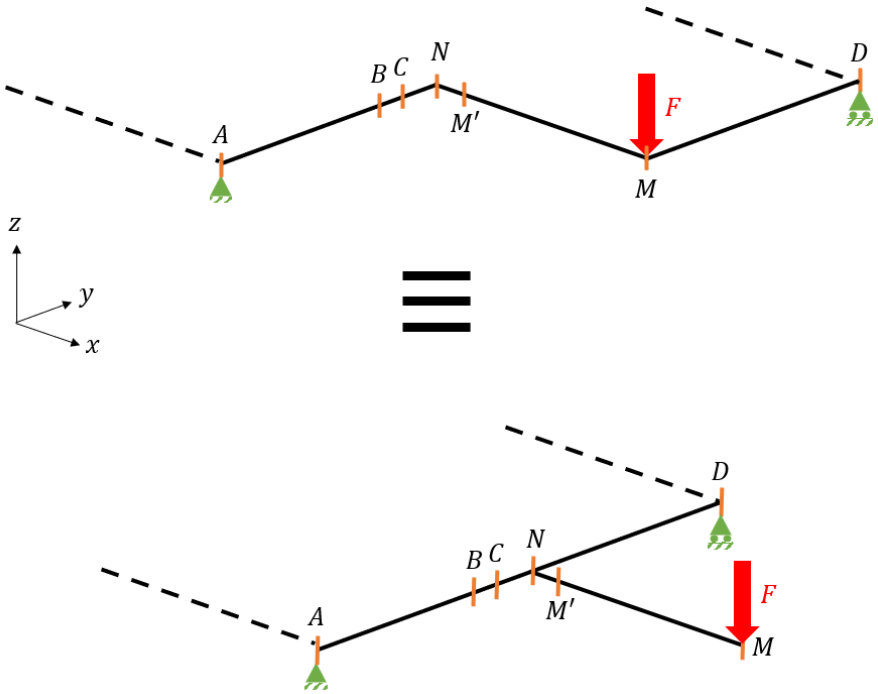

Figure 2.14: Simplification of the structure of the angular side of the shield

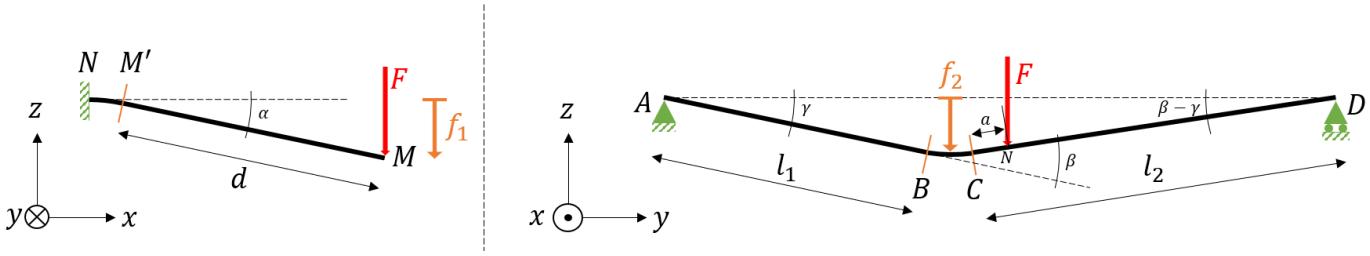

Figure 2.15: Deformations resulting from bending loading, broken down into two sub-problems dealing respectively with the (Oxy) and (Oyz) planes. All the parameters for superimposing the sub-problems and calculating the global deformation at point M are displayed.

section.

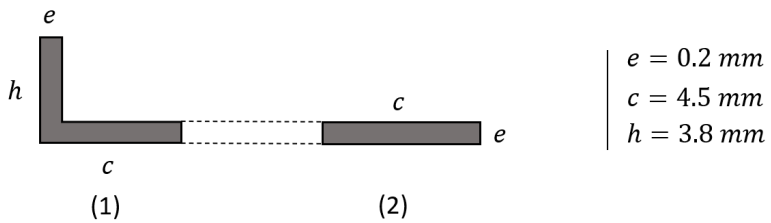

Figure 2.16: Section types used in the preliminary calculation model: L-shaped (1) and Rectangular (2)

Hypotheses:

- The stiffness of L-shaped section beams is assumed to be infinite. As a result, they do not allow any deformation. This is because the stiffness of rectangular-section beams is much lower than that of L-section beams. In fact, the bending

of thin rectangular section beam-portions is thought of as fully responsible for the global shield deformation in this hypothetical model. That is why this model only takes care of the angular side of the shield, whereas the opposite side (straight L-section beam) is assumed undeformable under its share of the load applied. The only beams that can deform on the angular side (represented in Figure 2.14) are NM' and BC. Beams MM', AB, and CD will only be able to rotate as rigid bodies in planes (Oxz) and (Oxy) to let the deformable beams take the whole deformation.

- The length of the small rectangular section beam portions will be set equal to $\epsilon_1 = \epsilon_2 = 1\,\text{mm}$.
- Based on the technical drawings for the LAIRD shield (see B.2), and for practical reasons simplifying the study, the geometric parameters of the model will be set to:

$$\begin{cases} L &= 38.5\,\text{mm} \\ b &= L/2 = 19.25\,\text{mm} \\ a &= 2\,\text{mm} \\ l_2 &= a + b = 21.25\,\text{mm} \\ l_1 &= L - l_2 - \epsilon_2 = 16.25\,\text{mm} \\ d &= 14.1\,\text{mm} \end{cases}$$

- Some of the calculations carried out will be based on the formulas suggested in a Solid Mechanics booklet by Pierre-Olivier Martin [7].

The bending of deformable beams will thus produce deflection angles of segments MM' (on the Oxz plane), and AB and CD (on the Oyz plane). From these deflexion angles, it is easy to trace back to the vertical deformation (f):

$$|f| = |f_1| + |f_2| \tag{2.1}$$

$$\text{Where: } \begin{cases} |f_1| &= |f_{M'}| + d\sin\alpha \approx d\sin\alpha \\ |f_2| &\approx l_1 \sin\gamma = l_1 \sin\left(\frac{\beta}{2} - \arctan\left(\frac{l_1 - l_2}{(l_1+l_2)\tan\left(\frac{\pi-\beta}{2}\right)}\right)\right) \end{cases} \tag{2.2}$$

Sub-problem n°1

In Figure 2.17, the vertical stops on either of the shield's x-oriented extremal edges are represented by the green horizontal line, like in Figure 2.13 (corresponding to vertical stop symbol in Figures 2.19 and 2.20).

The shear force F applied to M produces bending moment:

$$M_y(\epsilon_1 \leq x \leq \epsilon_1 + d) = -F(\epsilon_1 + d - x) \tag{2.3}$$

The moment loading that is applied to the NM' beam as a result of the shear force F is:

$$M_y(x = \epsilon_1) = -Fd \tag{2.4}$$

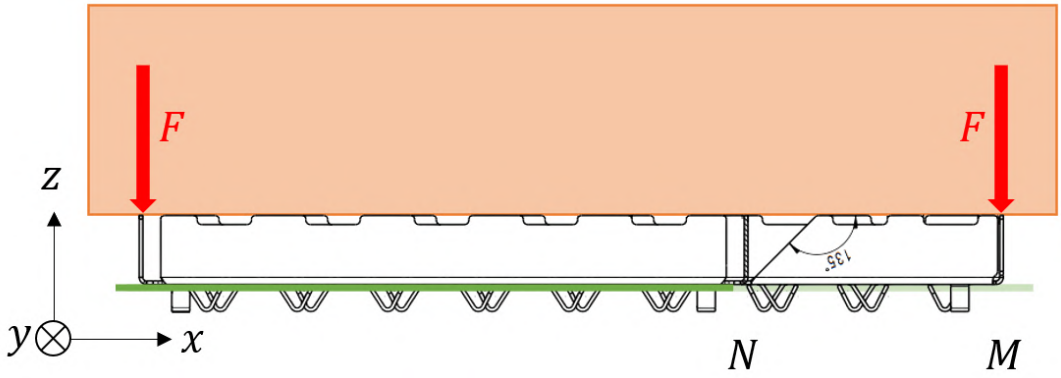

Figure 2.17: Sub-problem 1: bending of the part in the y direction

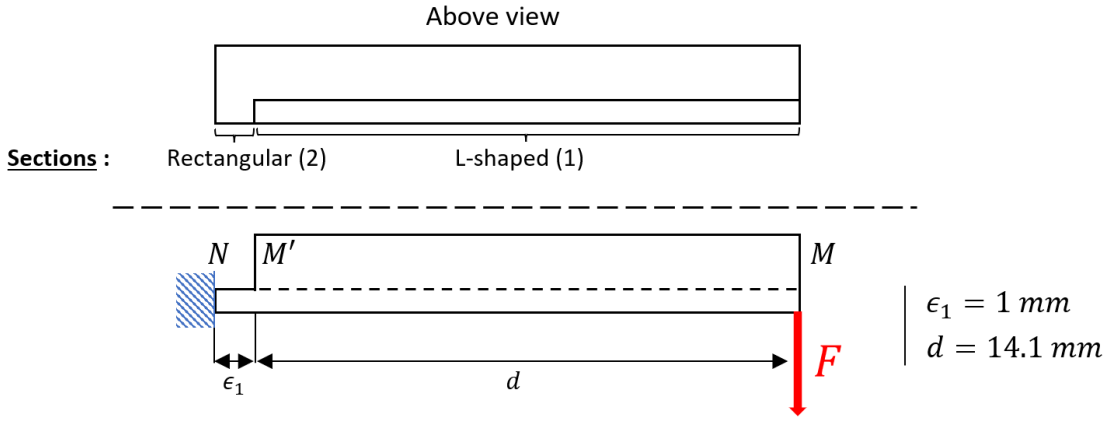

Figure 2.18: Sub-problem 1 model using beam mechanics

The shear force also propagates through the beam length, giving:

$$V(x = \epsilon_1) = V(x = \epsilon_1 + d) = F \tag{2.5}$$

And the angular deflection at point M', which is needed to calculate the vertical deflection at the extremity M, can be obtained with:

$$\tan \alpha = \frac{M_y \epsilon_1}{E I_y} \tag{2.6}$$

Where I_y is the second moment of area of the NM' beam with respect to the y axis:

$$I_y = \int_S z^2 dS = \iint z^2 dy dz = \frac{ce^3}{12} \tag{2.7}$$

Sub-problem n°2

On the cross-sectional view $(B - B)$ in Figure 1.16, the two points of application of the load are not visible, but we can imagine that it is distributed over the two points resulting from contact between the compression tool and the sheet (on segment AB in addition to the point visible here on segment EG).

As this model is purely theoretical and simplistic, it neglects the material interpenetration that can occur at high deformations.

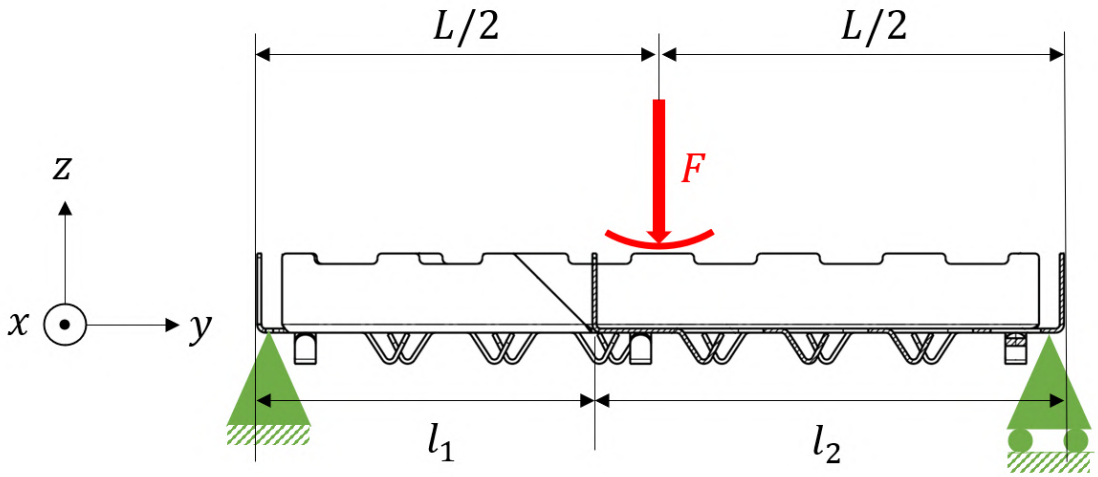

Figure 2.19: Sub-problem 2: bending of the part in the x direction

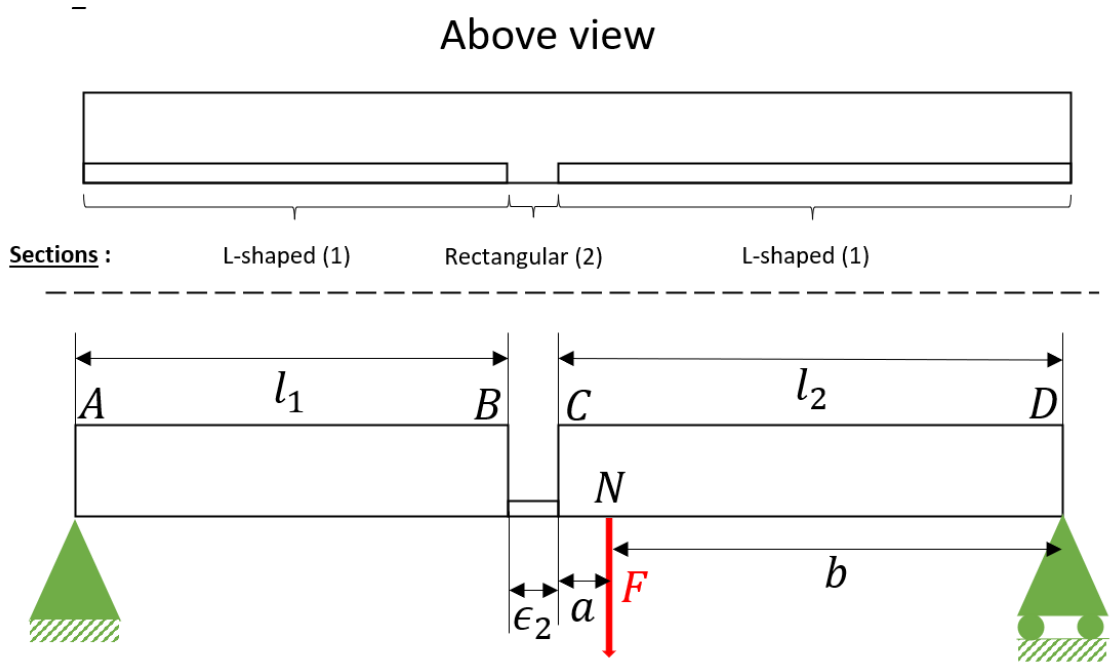

Figure 2.20: Sub-problem 2 model using beam mechanics

From this diagram we can derive relationships between the beam lengths:

$$\begin{cases} l_1 = \frac{L}{2} - a - \epsilon_2 \\ l_2 = \frac{L}{2} + a \end{cases} \tag{2.8}$$

The shear force applied to N (which is considered equal to the real shear force applied to M in sub-problem 1) produces a bending moment:

$$M_x(L - l_2 \leq y \leq L - b) = \frac{Fb}{2l_2^3}\left(d_2^2 y - d_1^2 l_2\right)$$

Where:

$$\begin{cases} d_1 = \sqrt{l_2^2 - b^2} = \sqrt{a^2 - 2ab} \\ d_2 = \sqrt{3l_2^2 - b^2} \end{cases} \tag{2.9}$$

Hence:

$$M_x(L - l_2 \leq y \leq L - b) = \frac{Fb}{2l_3^3}\left[(3l_2^2 - b^2)y - (l_2^2 - b^2)l_2\right] \tag{2.10}$$

When considering the BC beam only, embedded at point B and subjected to the load propagated from beam CD to point C, we get the angle of deflection β:

$$\beta = \arctan \frac{M'_x \epsilon_2}{EI_x} \tag{2.11}$$

Where M'_x is equal to the reaction moment at the interface between the two beams (point C).

$$M'_x = M_{RC} = \frac{Fb}{2l_2^2} d_1^2 \tag{2.12}$$

Similarly to equation 2.7, the second moment of area of the BC beam with respect to the x axis is expressed as:

$$I_x = \frac{ce^3}{12} \tag{2.13}$$

Estimation of the deformation

We can now apply equation 2.1 by injecting the expressions found for deflection angles of sub-problems 1 and 2:

$$\begin{aligned} |f| &\approx d \sin\alpha + l_1 \sin\gamma \\ &= d \sin\alpha + l_1 \sin\left(\frac{\beta}{2} - \arctan\left(\frac{l_1 - l_2}{(l_1 + l_2)\tan\left(\frac{\pi - \beta}{2}\right)}\right)\right) \end{aligned} \tag{2.14}$$

Application:

Let's estimate, using this simplistic model, the total vertical deflection of the structure (maximal at point M) when the compression tool (illustrated for the load case presentation in Figure 2.13) applies a total force $F = 15\,\mathrm{N}$. The angular side of the structure only undergoes half that load, one of the application points of the compression force being localized at the halfway point of the beam at the opposite side of the shield.
We will be using $E = 210\,000\,\mathrm{MPa}$ which is a common value for steel.

$$I_x = I_y = 3 \times 10^{-3}\,\mathrm{mm}^4$$

$$M_y = \frac{Fd}{2} \approx 105.75\,\mathrm{N\,mm}$$

$$M'_x = \frac{Fd}{4l_2^2} d_1^2 \approx 12.95\,\mathrm{N\,mm}$$

$$\alpha = \arctan\left(\frac{M_y \epsilon_1}{EI_y}\right) \approx 0.17\,\mathrm{rad}\ (\approx 9.74^\circ)$$

$$\beta = \arctan\left(\frac{M'_x \epsilon_2}{EI_x}\right) \approx 0.02\,\mathrm{rad}\ (\approx 1.15^\circ)$$

$$\gamma = \frac{\beta}{2} - \arctan\left(\frac{l_1 - l_2}{(l_1 + l_2)\tan\left(\frac{\pi-\beta}{2}\right)}\right) \approx 0.01\ \mathrm{rad}\ (\approx 0.57^\circ)$$

$$\Rightarrow |\boldsymbol{f}| \approx \mathbf{2.55}\ \boldsymbol{mm}$$

In conclusion, the constructed theoretical model for preliminary calculations predicts a 2.55 mm vertical deflection of the shield structure upon the application of a 15 N load, in the conditions described in Figure 2.13.

This model is far from perfect, as it changes some of the geometrical features of the real structure and noticeably omits the repeated holes cut out on each beam from the sheet metal manufacturing. Some of the more rigid beams have also been considered undeformable, which is obviously untrue, although relevant in this model. Finally, the real behavior of such structure in the test conditions copied by the model can be more complex than assumed. For instance, it can be expected that the angular side globally lifts off the vertical stop in reaction to the load being applied to the more rigid side of the shield. Such behavior will be explored during the analysis of lab tests, in section 3.4.

2.5 Assessment of other potential factors

2.5.1 Pick & Place

As explained in Chapter 1 (section 1.3.1), during the SMD process, Pick & Place machines use nozzles to take the shield out of its packaging (picking), carry it above its position on the PCB and install it (placing). In that process, nozzles apply a 2 N downward force onto the D-areas intended for this purpose, first when picking, and second when placing the shield.

Such a mechanical load does not seem significant, and it is difficult to understand at first glance how this type of load (vertical and downwards, with loaded areas towards the center of the part) would provoke the observed deformation. However, it is important to take into account every possible action provided to the components, even the slightest. Moreover, this potential cause was listed in the Ishikawa diagram made in preparation for the root cause assessment (Figure 2.6). Therefore, it is legitimate to devote a technical study to this question.

A numerical simulation run of the load corresponding to pick & place conditions was carried out and showed no similar result in terms of part deformation than the many observed cases on the SMD line. Visualization of the part deformation is shown in Figure 2.21. The means employed to obtain the simulation as well as the main parameters for setting up this simulation were the same as what will be presented in a section dedicated to numerical simulations in the next chapter (section 3.3).

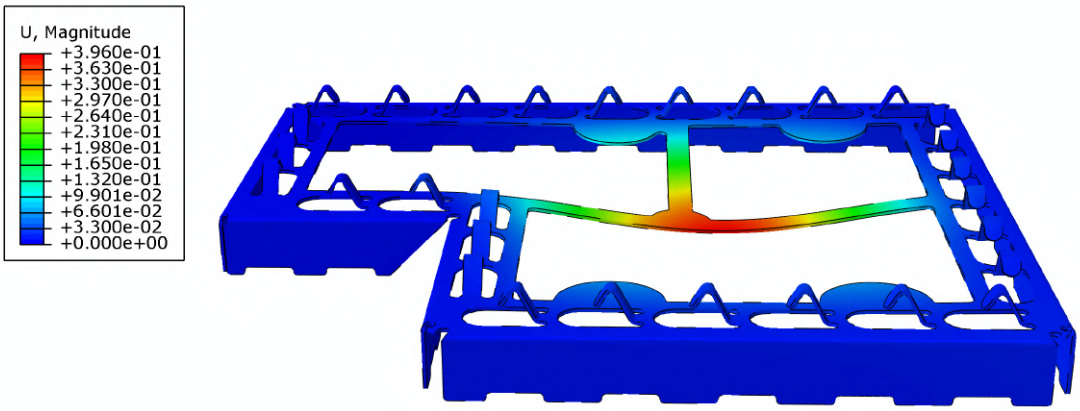

Figure 2.21: Part deformation obtained on *Abaqus* when applying a 4-point loading on the D-areas of the shied.

2.5.2 Potential amplification factors

As highlighted in the field observations analysis section (section 2.3), the amplitude of deformation tends to be greater at the SMD line output than at the observation point, prior to reflow. This phenomenon has been observed on multiple PCB units, by comparing the deformation before and after, on the same part.

As explained earlier, such amplification testifies that processes of SMD have an impact on the deformation itself when it is already present prior to SMD, and when the shield installed displays slight deformation (of type 1, see 2.2), sufficient to see that the anchor bracket at corner B is lifted (no plunging), to a certain degree, before entering the oven. However, it cannot explain nor trace the creation of the defects. That is why the interest in studying the deformations' amplification factors remains limited.

Different hypotheses can nevertheless be developed regarding the amplification of defects:

Firstly, we can imagine that the lack of contact with solder paste at corner B creates different boundary conditions than required, thus allowing the shield to expand under oven heat, which causes the arching of the structure.

Secondly, the behavior of the PCB plate under heat also plays a role in reflow quality. Because of the complex properties of composite materials making up the panels, a digital tool is available at Continental for experts to assess the thermal behavior of the PCB of each product under reflow conditions (see Figure 2.22).

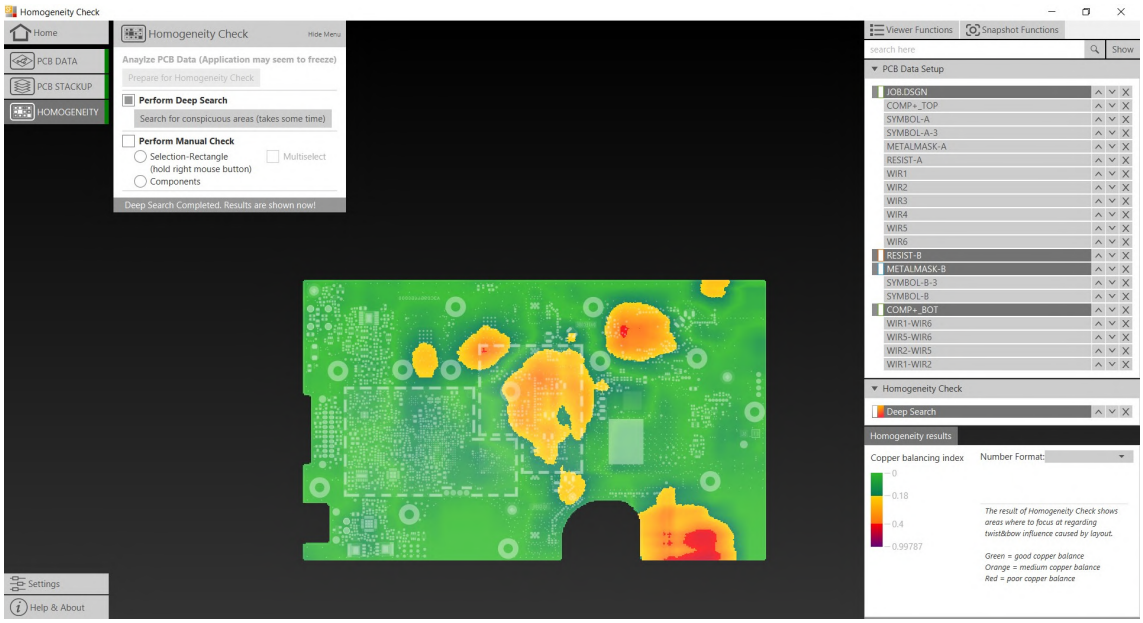

Figure 2.22: *Homogeneity check* file for the BSRF EA PCB.

Figure 2.22 displays results obtained using the *Homogeneity check* internal software, developed in Germany to map the distribution of copper balance in the PCB. Copper balance is closely linked with the thermo-mechanical behavior of PCB plates: during the reflow stage, unbalanced zones are subject to greater transverse (out-of-plane) deformation. Copper balance refers to the quality of copper distribution inside the multi-layer PCB: copper layers must form an evenly distributed structure along the thickness of the PCB.

We can see that the location of the angular side of the LAIRD EMI shield goes

across a highly unbalanced region, which suggests a partial explanation of the sensitivity of this area to deformations.

The rest of the report is based on the assumption that these lines of explanation are not sufficient to encompass the problem. Indeed, the same thermal load is applied to all units produced. Therefore, the only phenomenon showing a sufficiently satisfying correlation with the defect to be explored further in the study is the identified mechanical load enhanced close to the reel center. The above-mentioned potential causes for deformation amplification are distinguished as supplementary to the original cause of deformation, and can only worsen the situation, once the already-present defect subjects the shield to further deformation via the manufacturing processes to come.

2.5.3 Human factors

Human factors play a crucial role in factory production, particularly in the context of component handling, and significantly influence the potential damage caused to components. How operators handle the reels, at the delivery and logistics building, at the *Quickstore*, and then on the SMD line (see section 1.3.1) is paramount to ensuring the overall quality of the final product. Human factors encompass aspects such as training, ergonomics, attention to detail, and adherence to standardized procedures. Issues related to component handling can have profound consequences on the integrity of each component, in particular the fragile ones such as the EMI shields, and thus on the assembly. These factors have a predominant effect on the overall quality and reliability of the manufactured product. Therefore, emphasizing human factors in the production environment is imperative to prevent defects on the components.

In the case of the BSRF EA shields for EMI protection, the conditioning reels are of such dimensions and weight - compared to the majority of components -, that handling is truly critical. That is why, during the investigation, it was often pointed out as the suspected cause for the observed deformations.

However, whether that is the case or not, this issue not only is challenging to assess with precision during production phases, but it also holds an inevitable aspect, at least on a short-term basis. Indeed, operators often find themselves under pressure to meet demanding production targets and tight deadlines, creating a delicate balancing act between speed and precision. While these challenges are inevitable, a constructive approach involves suggesting a set of rules or guidelines that aim to minimize the impact of handling issues on component integrity, that can be effective in the long run. These guidelines can encompass best practices for handling, emphasizing proper training, ergonomic considerations, and procedural adherence. By providing a structured framework, manufacturers can empower operators to navigate the demands of production more effectively, reducing the likelihood of errors and damage during the handling process.

Precise reel-handling guidelines can be part of the suggestions to mitigate the issue of shield deformations, but for the technical part of the study, we will focus

on the mechanical bending factor, which constitutes a deeper root cause for the problem, as will be demonstrated in the following chapter.

Chapter 3

In-depth study of the packaging

3.1 Influence of reel winding on shield planarity

The field observations let us understand that the closer to the reel center, the greater the deformations. The first concrete way to verify this statement is to carry out measurements.

Measurements will of course not prove anything, but they can take the observation one step further than what was previously observed on the production line, by quantifying an example of the deformations inside the reel, before the automated unpacking by the placement machines, which suffer too limited control for serving this investigation.

3.1.1 Measurement method

It was decided to use an optical measurement tool to assess what is called the coplanarity of the shield anchor brackets.

Coplanarity refers to the flatness or levelness of multiple surfaces on a component relative to each other. It measures how closely aligned or parallel different surfaces are in relation to a common plane. In electronics manufacturing, coplanarity is a crucial quality metric to ensure the evenness and uniformity of surfaces in components, contributing to the overall precision and thus quality of the soldering.

In the case studied, coplanarity will be used to characterize the level at which parts are bent. This will allow the observation that deviation magnitude due to bending is predominant compared to common coplanarity imperfections.

The coplanarity measurements performed follow a precise documented method, described in-depth in Appendix C [6]. To explain briefly the measurement protocol, the optical measurement machine takes into account a user-defined mapping of the measurement points, then zooms in on each of these points to determine the distance from its sensor to the object's surface, according to the optical characteristics of the tool. For this assessment, the chosen protocol is the coplanarity measurement using the "maximum" plane, which can also be described as the seating plane of the object. It is the best possible approximation of the PCB plane, on which the

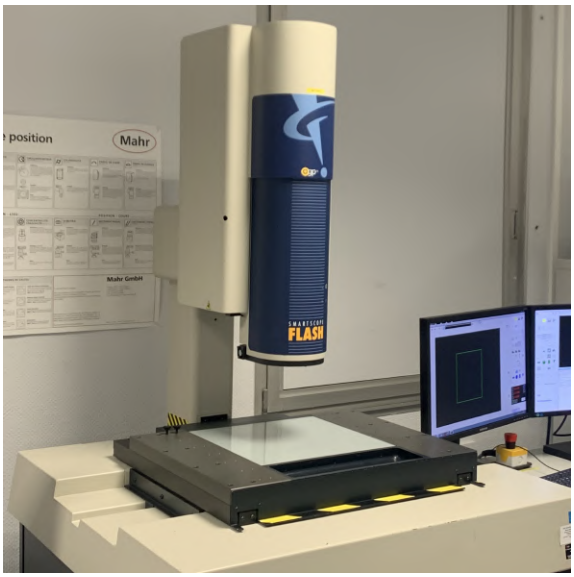

Figure 3.1: Optical Gaging Products *SmartScope* is the tool used for our coplanarity measurements.

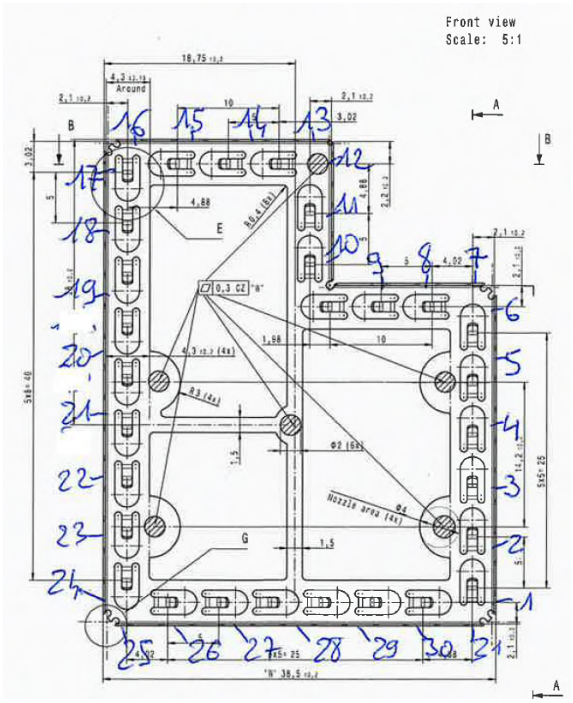

Figure 3.2: Definition of the measurement points on every anchor bracket of the LAIRD shield. This definition applies to all the measurements performed.

shield seats (see Appendix C). The program finally outputs the values of altitude differences between measurement points and the reference (seating) plane. In that way, we dispose of a convenient visual interpretation for the results of coplanarity.

To carry out the measurements, the shields have to be placed upside down on the *SmartScope* support in order to have the anchor brackets face up toward the optical measurement system. That is why the computed seating plane is always spatially located above every measurement point, apart from the three seating points that are on the seating plane.

3.1.2 Results of the reel start-to-end comparison

Ten shields from the beginning of a sample reel and ten shields from its end were taken for coplanarity measurements and comparison. The shields from the end of the reel (the closest to the reel center) are numbered 11 through 20. The shields from the beginning of the reel (from the layers of tape that are the farthest from the reel center) are numbered 21 through 30.

The component reel taken as sample was removed from the manufacturing circuit when it entered the CEMS workshop. This means the reel had undergone normal conditions up until that point, among which handling by logistics and *Quickstore* operation workers, but no handling was performed by the CEMS manufacturing line operators.

Following is the part deformation of the first of each group of shields (it would not be necessary to show the result for each of the 20 shields measured). The deformation was displayed using a Python script, mapping the vertical deviation of each point compared to its theoretical (perfect) location on the reference plane.

The maximum deviation and the point where it was identified for each shield are classified in Table 3.1 below, where the lines corresponding to the diagrams of Figure 3.3 have been entered in bold, and the lines corresponding to the maximum deformation of each group have been colored in red.

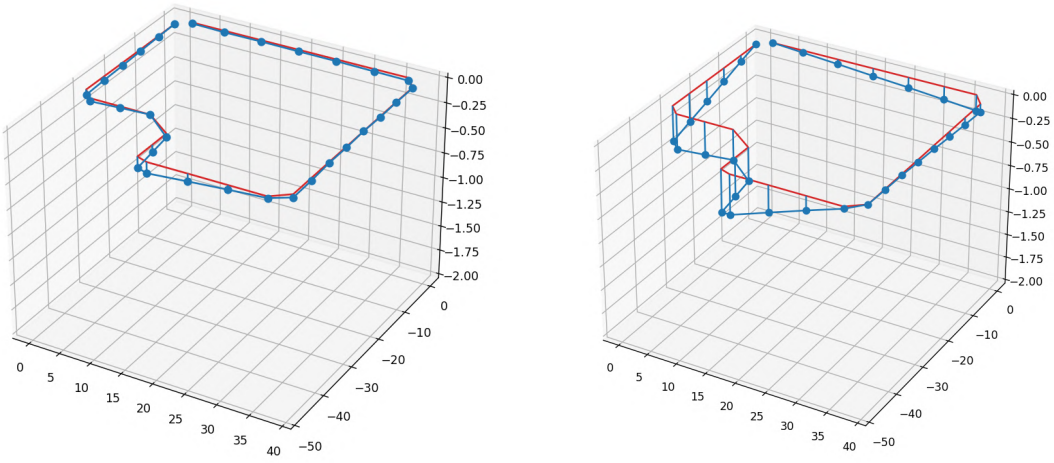

(a) Part n°21

(b) Part n°11

Figure 3.3: Deformation of 2 shields coming respectively from the beginning (a) and end (b) of a sample reel.

Although shield n°11 is fortuitously the one with the highest deformation, this observation testifies to the symptomatic deformation of shields at the end of the reel, even before SMT manufacturing processes (namely handling by the line operators and Pick & Place) can interfere.

Observed area	Shield n°	Max. def. [mm]	Meas. point
Beginning of reel	**21**	**0.106**	**13**
	22	0.111	13
	23	0.110	13
	24	0.115	13
	25	0.115	13
	26	0.104	13
	27	0.092	13
	28	0.110	13
	29	0.117	13
	30	0.092	13
End of reel	**11**	**0.435**	**12**
	12	0.104	13
	13	0.102	13
	14	0.097	13
	15	0.106	13
	16	0.231	12
	17	0.118	13
	18	0.099	13
	19	0.107	13
	20	0.094	13

Table 3.1: Maximum vertical deviation (coplanarity) for each shield measured

3.2 Non-destructive X-ray analysis

Product qualification laboratories at the Toulouse site include an X-ray analysis facility, which was natural to use. Indeed, the study of inner-reel deformations could benefit from the non-destructive and comprehensive approach 3D X-ray tools offer, allowing for a thorough analysis without compromising the integrity of the parts. This capability is particularly valuable when investigating complex or intricate components where external inspections may fall short.

An X-ray study is essential for two primary reasons. Firstly, it helps reveal deformations within the reels before manipulating the shields, shedding light on the role of packaging in the occurrence of defects. This aspect emphasizes the importance of understanding how the parts are positioned and interact within the packaging. Secondly, the X-ray study extends the reasoning established in the previous section by providing evidence of a cause-and-effect relationship, where lies the added value of the study. It links the deformations observed in scrapped parts with those identifiable within the packaging.

3.2.1 X-ray resources and system limitations

The X-ray machine available at the Toulouse site and which was used here is of the same type as that shown in Figure 3.4. The X-ray analysis lab is equipped with the software *vgstudio max*, which allows tomographic reconstruction of a volumetric

body, for example from the 3D data collected through the X-ray scans.

The X-ray scanning process is rather special in this case, in that the dimensions of the reel make it impossible to perform a single scan encompassing all 250 components present on a single reel.

Therefore, a way to cover the whole reel in several scans had to be imagined: The reel is placed vertically in the X-ray machine, so as to frame the lower part of the disc. By positioning the X-ray shooting window in this way, the machine's resolution is satisfactory for analyzing flatness deviations of the order of magnitude of the tolerance indicated on the shield drawings (see Appendix B.2). In this way, faulty parts can be properly identified[1].

Figure 3.4: GE phoenix v-tome-x s 3D X-ray scanner

Thus, the reel is "cut" into 6 "sections", which are analyzed one by one. Analysis of a reel therefore requires 6 X-ray shots, reorienting the reel between each shot to cover each part with a different shot.

Early attempts shed light on several challenges that had to be faced. For instance, it was discovered that the multiple layers of tape containing the shields moved relative to each other in between two shots, i.e. from one orientation of the reel to another, due to the action of gravity. This affected the total counting of the number of shields. Indeed, counting the components displayed on the images from the scan is necessary to assign them a position numbered from 1 to 250. The counting is based on the superimposition of the 6 images, using markers placed on the software used to analyze the scans.

It was therefore decided to mark the "slicing" of the reel into 6 sections with metal strips, physically present on the reel structure and visible in the X-ray image. In addition, the addition of adhesive tape on the side of the layer stack (areas accessible from the outside of the reel) should limit the relative movement of tape layers.

3.2.2 Deformations tracking strategy

The reel is collected from the manufacturing line stock and supplied to the laboratory, which performs the necessary 6 shots (see previous section to understand why 6 X-ray shots have been found most convenient for carrying out the scans).

[1]Please note, however, that the deformation within the reel is an imposed deformation, and the potential mechanical behavior of the part may well result in a final deformation after placement that consists only of residual (plastic) deformation. This subject will be explored in greater depth in a subsequent section.

The reel is then replenished on the production line on the next day of BSRF EA bottom-side production.

When the reel is used on the SMD line, the corresponding shields are observed on the PCB panel at the SIPLACE output, in order to record all deformed shields and their position in the reel. To do so, we rely on the current component number indicated on the SIPLACE machine interface, cross-referenced with a meticulous count of all the components crossing the observation point (from the start of the use of the corresponding reel).

The production data is sent back to the laboratory, which can then efficiently carry out their analysis on the components at the indicated positions, by directly taking measurements in post-processing of the X-ray imaging.

Rejected panels are also supplied to the X-ray laboratory, so that the scrapped parts installed on the PCB can be scanned, at a final state, after passing through all steps of SMT. This allows a comparison of the deformations before and after the SMD line.

3.2.3 Results

Initially, the X-ray scans were used to count the components inside the analyzed reel, so as to assign a position to each one of them from 1 to 250, as explained above. To do so, screenshots of each scan along a section plane orthogonal to the reel's axis were performed. As visible in Figure 3.5, the resulting images showed diverse shapes corresponding to the shields inside the reel, depending on the section plane's defined location along the shields' width. In spite of these differences, all images were clear enough to be used for counting shields. The challenges faced when assigning a number to each shield were discussed in section 3.2.1.

The X-ray images here allow to better understand how the shield layers stack onto each other, which gives a first concrete view of the conditions that apply on the shields to result in their deformation, according to the priority hypothesis for the root cause of deformations, formulated in section 2.4 (see Figures 2.7 and 2.12).

Indeed, these images show just how much the shield stacking conditions evolve with the winding radius: it is apparent that shields closer to the center should be more likely than those further away to bend in the winding direction, given the way in which they rest on one another. It also seems that correct overlapping (as parallel planes) is easier to achieve on the outer layers than close to the reel center.

Once the reel positions of bent components have been identified during the PCB assembly (SMT), the goal was then to use the 3D tomographic reconstruction of the shields inside the reel to measure the plane deviation of the shields involved, which could be found across the 6 different scans (for 1 reel) thanks to the meticulous counting carried out beforehand.

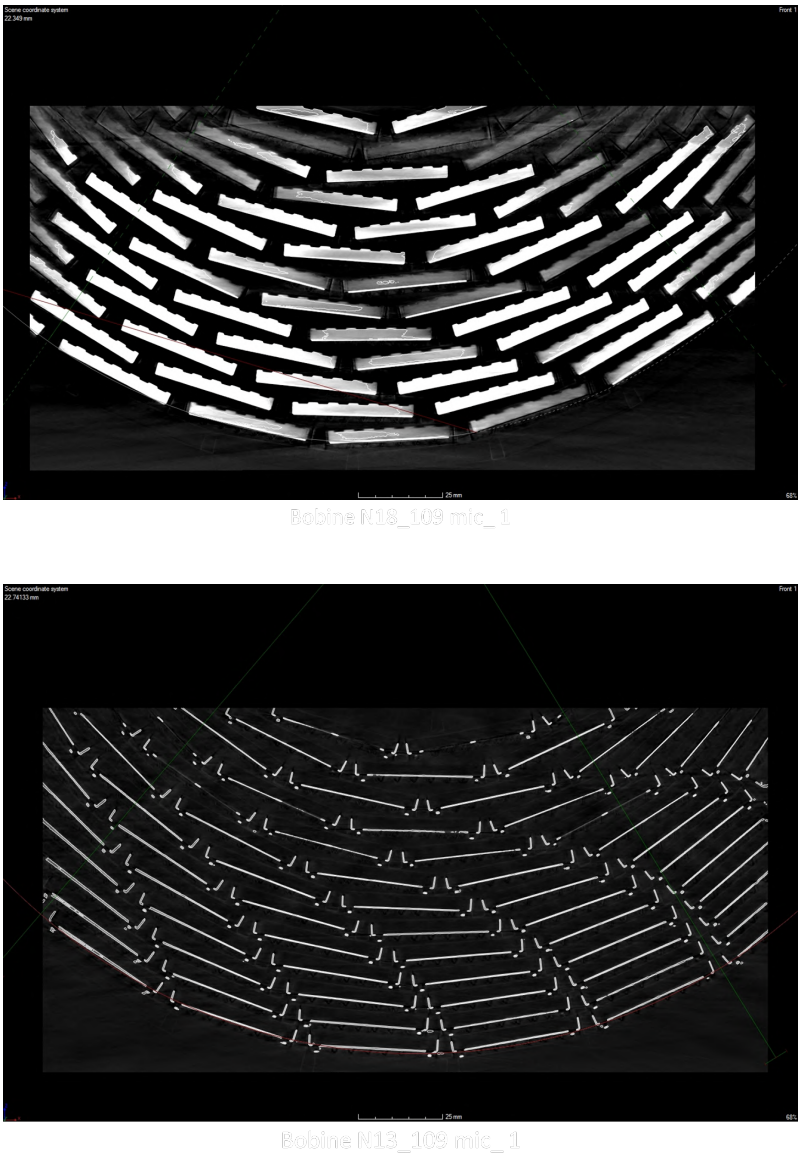

Figure 3.5: Two examples of screenshots from the 3D tomographic reconstruction obtained on *vgstudio max* from the X-ray scan of a reel.

Even though the reel selected for the results analysis has given rise to a substantial quantity of defects, it was decided to repeat the analysis for comparison on the three most exploitable examples of shield deformation that were found from this reel. X-ray studies are extremely time-consuming, especially with the protocol applied in the present study (from 1 to 2 hours for one single scan).

An example of the measurements carried out is shown in Figure 3.6.

In order to prevent any possible counting errors, even if we have ensured that it is as close to perfect as possible, we also carry out flatness measurements on the shields in the vicinity of the identified position (± 6 positions).

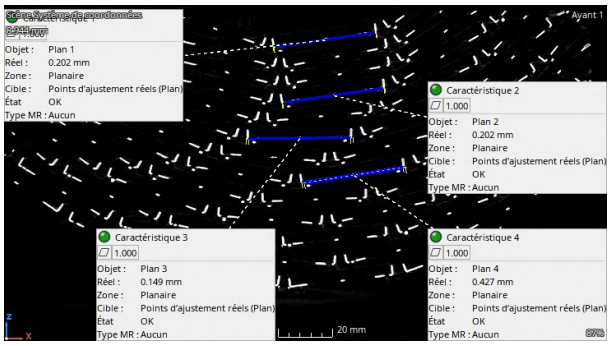

(a) Examples of planar deviation measurements for several shields from an X-ray scan of one portion of a reel, with the definition of a reference plane on the 3D tomographic reconstruction using three corners.

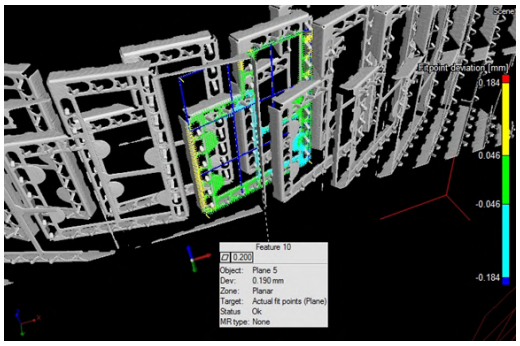

(b) Initial planar deformation measurement of a shield within the reel.

Figure 3.6: Examples of non-destructive X-Ray measurements of shield deformation within a reel.

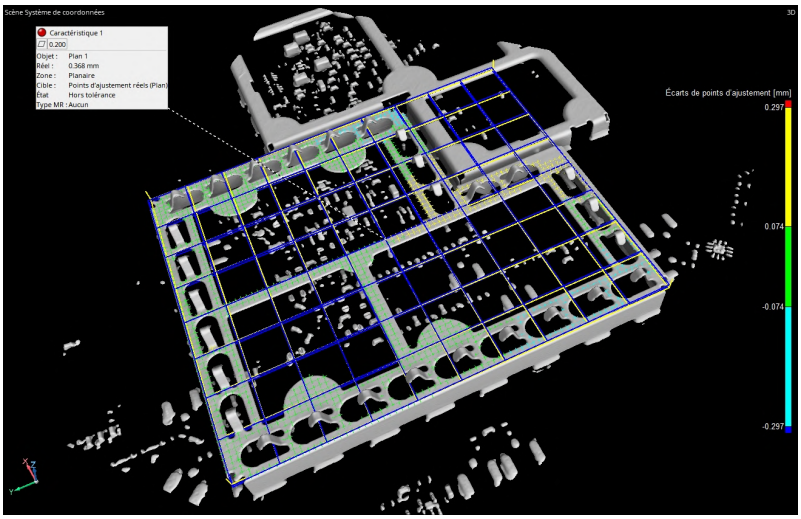

Figure 3.7: Final planar deformation measurement of a shield following PCB front-end assembly.

The same measurement method was applied to the shields installed on the resulting faulty assemblies (see Figure 3.7).

The results and comparison of deformations inside the reel and on the PCB have been compiled in Table 3.2.

Statistical data about each group of shields that have undergone planarity measurements has also been gathered in table 3.3 below. That information allows taking advantage of the measurement groupings around these positions scattered across the reel, all the same with a focus on the end of the reel. This was used to establish

Sample n°	**2**	**4**	**13**
Reel position	180	196	226
Deformation (Reel) [mm]	0.488	0.511	0.542
Deformation (PCB) [mm]	0.302	0.368	0.364

Table 3.2: Results of deformation measurements on 3 samples with *vgstudio max*

Shield group	Average deformation [mm]	R_{pot} (%)	R_{obs} (%)
A [174;186]	0.224	41.67	25.00
B [190;202]	0.210	33.33	25.00
C [220;232]	0.286	50.00	33.33

Table 3.3: Statistical data on each measured population (±6 units around the targeted component), where R_{pot} and R_{obs} are respectively the potential and observed defect rate among the three shield groups.

predictions of defect rates based on the share of shields exceeding deformation tolerance within the reel, and to compare them to the actual defect rates within the three groups of shields.

In this table, population A corresponds to the 12 shields surrounding position n°180 (included) in the winding order, population B to the 12 shields surrounding position n°196, and population C to the 12 shields surrounding position n°226. As a reminder, the counting of shields inside a reel has been defined by positions in order of unwinding, from the reel beginning towards the reel end or center.

What is demonstrated through this experiment is that the average deviation of the observed populations (around the positions that gave rise to scrap) is greater than the part's flatness tolerance.

Within groups A, B, and C observed, between 60 % and 75 % of potential defects identified within the reel (deviation 0.2 mm) resulted in actual production scraps due to a deformation of the LAIRD shield.

Note that the final deformation is without exception lower than the deformation within the reel of the same shields. In fact, this difference is associated with the fact that the shields are deformed under stress for the entire time of conditioning in reels, which means that a certain range of elastic deformation is compensated for when the stresses are released at the time of unwrapping and simultaneous placement of the shields on the PCB.

This phenomenon will be explored in a later section dedicated to the analysis of mechanical behavior and related laboratory tests (section 3.4).

3.3 Simulation of shield bending

3.3.1 Digital tools and resources

The entirety of simulation works carried out during the internship was achieved using the *Dassault Systèmes* software *Abaqus*. *Abaqus* is a versatile finite element analysis (FEA) software offering capabilities such as predicting structural responses under various conditions, simulating multiphysics interactions, utilizing diverse material models, managing nonlinearities effectively, analyzing dynamic events like vibration and impact, among other use-cases. It finds extensive popularity across

industries for virtual testing and design optimization.

The nature of the mechanical problem in question led to the use of a 3D environment: 3D simulations provide a more realistic representation of the entire structure, capturing spatial variations in stress, strain, and deformation. In addition, when dealing with complex three-dimensional geometries or components, a 3D simulation is necessary to accurately capture the behavior throughout the volume.

In light of the shield's design and construction - folded sheet metal with very low thickness (200 μm) - it probably would have been possible to model the problem using shell elements in a 3D modeling space. However, for practical reasons, the pre-existing CAD model for the part was used, thus saving the time required for part design, especially knowing the complexity of the shield's geometry. Therefore, the model used was a 3D solid deformable model. After importing the provided *.STEP* file of the assembly (see Figure 3.8) into the *Part* module. The only part worth keeping for the *Abaqus* assembly is the LAIRD shield, which is the object of interest for the study.

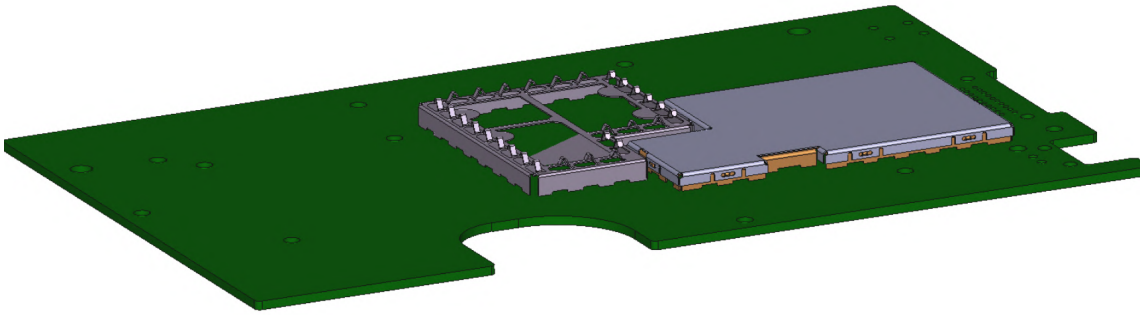

Figure 3.8: 4-Part assembly *.STEP* file containing the PCB plate, the two EMI shields, and the cover for the MSA shield.

In the *Property* module, we define the material according to what has been assessed in the state of the art overview (section 1.3.1): Homogeneous material ($\rho = 7.85 \times 10^{-6}\,\mathrm{kg\,m^{-3}}$) with elastic properties ($E = 210\,000\,\mathrm{MPa}$, $\nu = 0.3$).

3.3.2 Boundary conditions and loading

A static analysis was configured through the *Step* module. In the *Edit Step* feature, we set an automatic incrementation with the following parameters: Maximum number of increments: 100; Increment size: Initial = 0.01; Maximum = 0.1. There is no need to change the default Minimum increment size.

The load case imagined to simulate the bending of the part in a similar fashion to what happens inside the reel is the following:

A 3 mm displacement is imposed (with a quasi-static assumption, granted by the static analysis model) to a region defined geometrically as shown on the diagram

of Figure 3.9, which represents mid-width linear loading on the lower (xy)-coplanar surface (sheet metal width) of the anchor brackets.

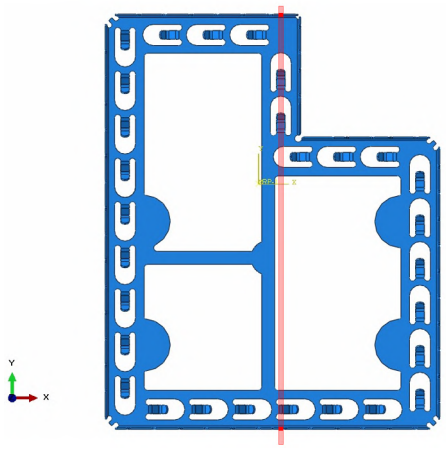

Figure 3.9: Loading areas definition: linear load on at mid-width of the bottom surface of the anchor brackets.

A previous test was run with an imposed force instead of an imposed displacement. Thus, we had to define a surface of load application. That is why the width of this area was arbitrarily set to 0.2 mm (the same model was used for both simulations). Note that an imposed displacement is considered in *Abaqus* as a boundary condition and not a load *per se*.

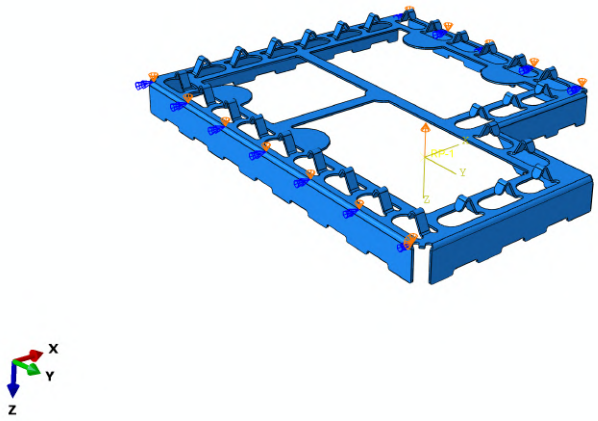

Figure 3.10: Load and boundary conditions for the shield bending simulations carried out.

In order to express that the defined surfaces' imposed displacements take place simultaneously, we chose to establish a kinematic coupling type interaction (within the *Interaction* module), with two options for the coupling parameters:

1. All d.o.f.[2] coupled.
2. Only U_3 coupled for both surfaces.

[2]degrees of freedom.

When establishing the interaction between the loaded surfaces, a reference point is created, whose function is to control the kinematic behavior of the interleaved surfaces according to the defined coupling. Thus, the vertical 3 mm imposed displacement *load* is applied directly to this reference point.

BCs[3] are illustrated on Figure 3.10: vertical stop on two edges, and displacement BC applied on the reference point (indicated by the arrow pointing in the direction of displacement, which can be confused with the representation of a force). Furthermore, two possibilities have been devised to express the fact that the two top edges of the shield are pressed against a vertical stop, in terms of kinematics rules that can be processed by *Abaqus*:

1. $U_3 = R_1 = 0$ and 2 Pinned knots to avoid uncontrolled rigid body movement.

2. $U_2 = U_3 = R_1 = 0$ and 2 Pinned knots.

All of the options offered by combining the BCs and interaction types give rise to relatively different results, that will be discriminated based on their consistency with the observations and tests to follow, as well as their sheer plausibility.

Before running the simulation, the part is meshed using *tet* elements. Indeed, other element types seemed not to work as *Abaqus* returned an error message. Homogeneous seeds were defined on the thin edges where stress concentration is expected. The meshed part is shown in Figure 3.11.

3.3.3 Results from the elastic model

The evaluation of simulation results obtained with a purely elastic model (parameters defined in the previous section) was made with the only combination of interaction type 1. and BC type 1. as defined in the previous section. Indeed, it is best not to dwell on this model, as the results obtained with the second model tested, involving the plastic behavior of steel, are potentially much truer to reality.

Results of simulation runs carried out with the hypotheses established for the moment give rise to some very telling visualizations: we find the exact signature of the deformation fault causing so much scrap (see section 2.1.2).

The application of the imposed displacement only seems to affect the region of lower stiffness, resulting in the observed deformation. However, the instruction for coupling the displacement of both load-application surfaces does not seem to have behaved in the way intended. We will extend further on this matter in section 3.3.5.

[3]Boundary Conditions.

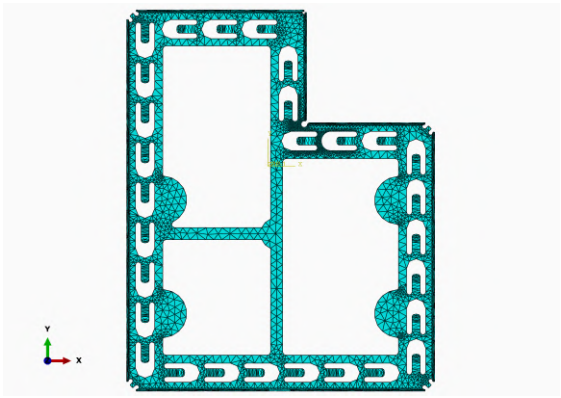

(a) View n°1 (global view)

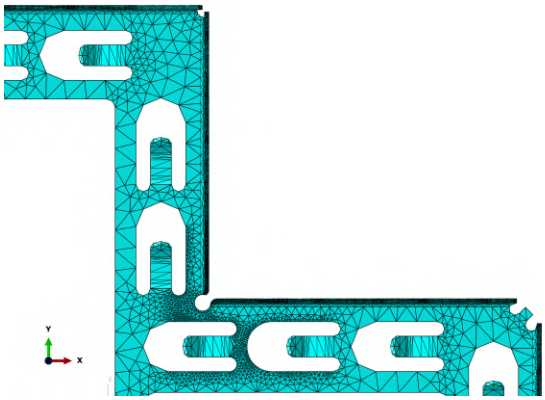

(b) View n°2

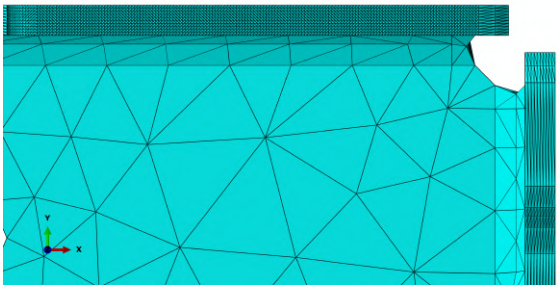

(c) View n°3

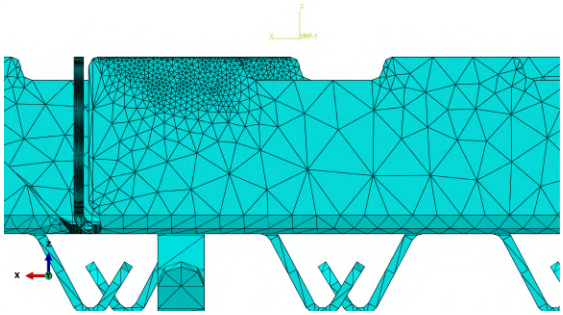

(d) View n°4

Figure 3.11: Global and precise views of the mesh applied to the part, using 3D tet elements.

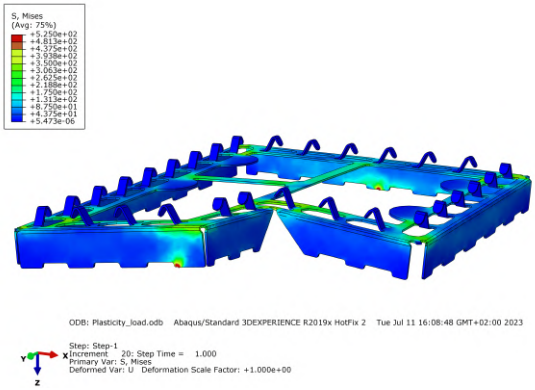

(a) Von Mises stress

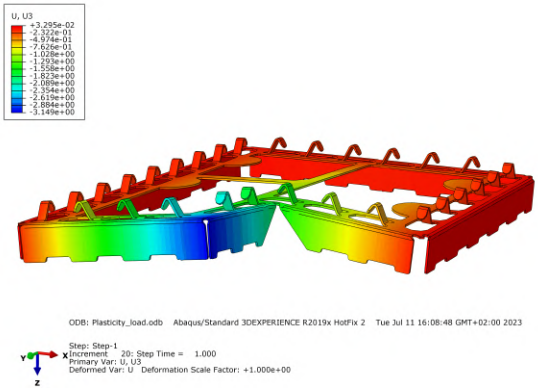

(b) Displacement along the z-axis (U_3)

Figure 3.12: Simulation results with the elastic model

3.3.4 Realistic model: implementation of component plasticity

To refine the simulation model, it is relevant to redefine the properties of the material used. The TS275 steel used for the shields features plastic deformation once the yield strength has been reached. Only in this way can deformation be observed when no mechanical stress is applied to the part. This is residual deformation (after unloading and after elastic properties have taken effect), corresponding to the plastic deformation of the material.

Yield stress [MPa]	Plastic strain
340	0
350	0.02
400	0.035
450	0.05
500	0.075
520	0.1
525	0.2

Table 3.4: Values entered in the *Plasticity* feature for defining material properties of S275 steel in *Abaqus* according to the stress-strain curve of Figure 3.13.

To model this behavior, a second step is added, where the BCs are conserved and the loading conditions are canceled, acting as a release from mechanical constraints (when unpacking the shield). This step (*Step 2*) is called the unload or relaxation step. Thus, in the *Load* module, only the displacement boundary condition is not propagated to step 2.

The mechanical properties of the material also need to be modified. The *Plasticity* behavior was defined after the Engineering Stress-Strain[4] curve below (Figure 3.13) [13]. Values set as input to the *Plasticity* behavior feature are listed in table 3.4.

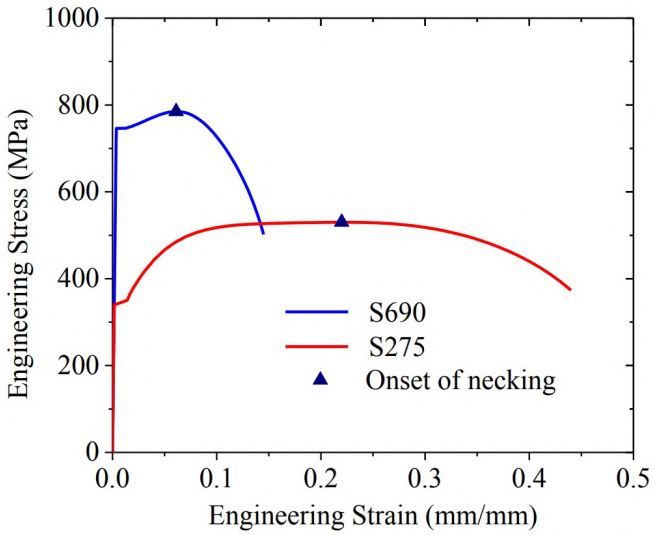

Figure 3.13: Engineering stress against engineering strain for S275 and S690 steels [13].

Upon the first simulation run, rigid body rotation around the z-axis occurred during *Step 2*, which prompted us to rethink BCs, hence the introduction of BC n°2. All results found with BC n°1 are potentially influenced by this rigid body rotation.

[4] *Engineering* values do not account for any changes in cross-sectional area or length of the part, they are based on the original (undeformed) geometry of the part.

BC type	Int. type	Deflection [mm]
1.	1.	−1.30
1.	2.	−0.95
2.	1.	−1.26
2.	2.	−0.80

Table 3.5: Deflection obtained at corner B at the end of *Step 2* for each BC/interaction type tested.

As expected, the deformation obtained features the same signature shape, which leads us to believe that the hypothesis of the cause of the deformation is well-founded. At the end of *Step 2*, residual deformation remains, as a result of the yield strength of the material exceeding under load (*Step 1*).

By the end of *Step 1*, the vertical displacement at the most lifted point is always (without surprise) approximately 3 mm, which is the value of the imposed displacement. However, we notice that simulation runs carried out using interaction type 2. result in this exact displacement value, which leads us to think that the conditions of interaction type 1 produce a parasitic effect. It is thus believed that the most relevant results are the ones obtained using both interaction type 2. and BC type 2.

The final deflection obtained (at corner B) after *Step 2* (after relaxation) is listed for each BC/interaction type in table 3.5. Obtained values are negative because of the orientation of the z-axis, corresponding to the upward direction in lab conditions where the shield is placed on a support upside down and bent by the displacement of a compression tool in a downward direction.

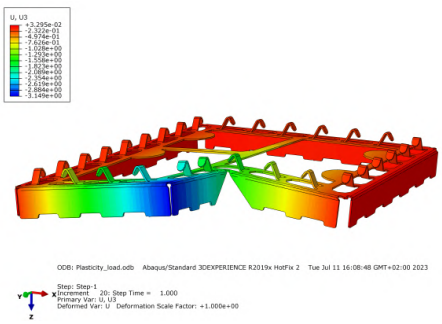

(a) Displacement along the z-axis (U_3) at the end of *Step 1*.

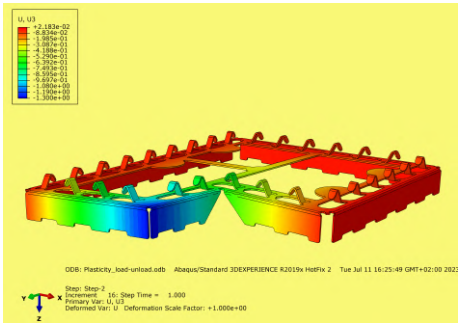

(b) Displacement along the z-axis (U_3) at the end of *Step 2*.

Figure 3.14: Plastic behavior simulation results obtained with BC type 1. and interaction type 1.

3.3.5 Limitations of the numerical simulation

The question arises as to why identical lifting is not achieved from the two coupled surfaces. One possible hypothesis to tackle this question is the following: the defined kinematic coupling might not ensure that the two surfaces remain at a fixed distance from the reference point, which allows the latter to be displaced by the

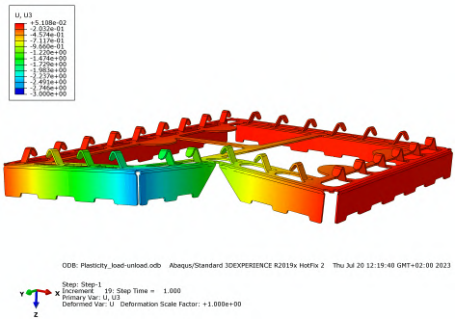

(a) Displacement along the z-axis (U_3) at the end of *Step 1*.

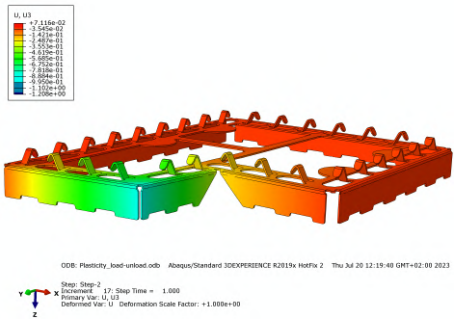

(b) Displacement along the z-axis (U_3) at the end of *Step 2*.

Figure 3.15: Plastic behavior simulation results obtained with BC type 1. and interaction type 2.

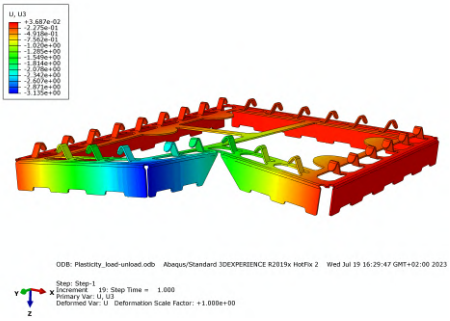

(a) Displacement along the z-axis (U_3) at the end of *Step 1*.

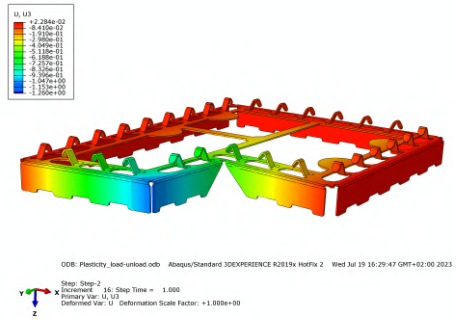

(b) Displacement along the z-axis (U_3) at the end of *Step 2*.

Figure 3.16: Plastic behavior simulation results obtained with BC type 2. and interaction type 1.

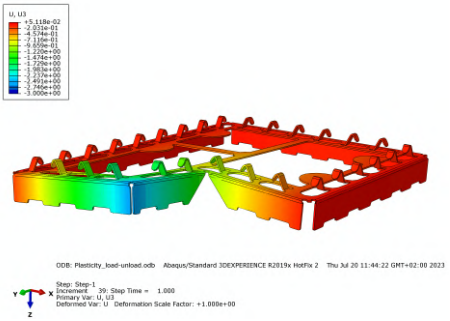

(a) Displacement along the z-axis (U_3) at the end of *Step 1*.

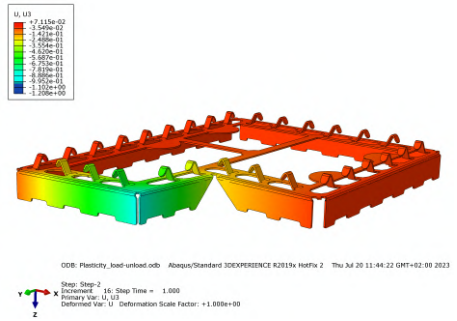

(b) Displacement along the z-axis (U_3) at the end of *Step 2*.

Figure 3.17: Plastic behavior simulation results obtained with BC type 2. and interaction type 2.

amount set, while the difference in rigidity of the two regions results in the tilting of the coupled surfaces' plane.

However, as will be shown in the next section, the fact that corner B lifts upon applying the bending load, unlike the other side of the shield, agrees with what will be observed and concluded from the mechanical tests carried out.

Moreover, in considering the {shield + packaging} assembly, it turned out that extrapolating the numerical simulation to an assembly was too complicated to manage under the imposed time constraints. The interplay between the shield and packaging components introduces a level of intricacy that demands careful consider-

ation and in-depth analysis. The building of an assembly model was initiated, but we ran up against a problem of mesh compatibility with the interactions defined between the various parts. The comprehensive assessment of the entire assembly is thus deferred to a later phase.

The forthcoming tests will specifically hone in on scenarios where the shield is positioned within its packaging cell (or compartment). This approach allows for a more concrete exploration of the dynamic interactions between the shield and the packaging, fostering a nuanced understanding of their mutual behavior.

3.4 Mechanical tests and defect reproduction

3.4.1 Tools used

All the mechanical tests carried out were made possible by the REL lab at Continental Automotive Toulouse, which is equipped with mechanical testing machines (tensile/compression tests) such as that shown in Figure 3.18. These traction machines are used for various materials tests such as tension, compression, and flexure, and are widely used in industries like automotive and aerospace. They feature a sturdy frame, advanced control systems, and embedded software for test results display and analysis.

Figure 3.18: Instron 5900 series universal machine

To perform shield bending tests with this setup, the idea is to run a displacement of the compression tool coming up against the part (shield), at the intended point of load application. Conditions are the same as those intended for the mechanical simulations (see previous section). The first step is to conceive a custom fixture for our part, in order to recreate as truly as possible the boundary conditions taken as hypothesis for the whole study.

A first fixture (Figure 3.19), designed based on the basic part dimensions, was machined, but the first tests carried out did not result in consistent results due to unavoidable contacts of the small springs with the fixture's inner wall.

To avoid any parasitic contact, the final custom fixture presented in Figure 3.20 was designed on the *Dassault Systèmes* software *Solidworks*, and manufactured by 3D printing of polylactic acid (PLA) material. Notches have been added to leave room for the springs, while holding the workpiece on the edge of its sides, with a bearing area between each spring. Horizontal stops also follow the outer shape of the workpiece to keep everything in place.

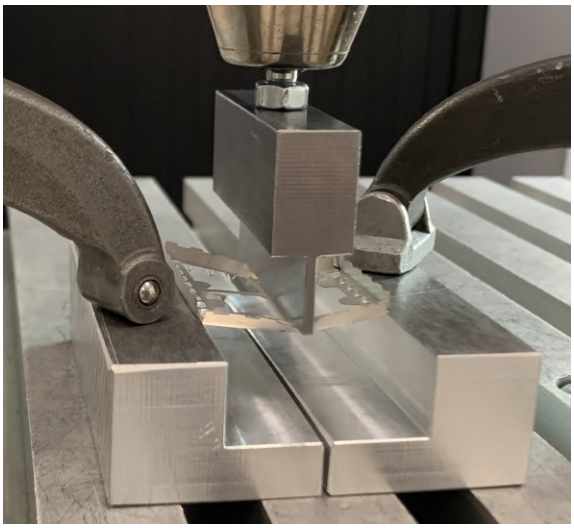

Figure 3.19: First attempt of custom fixture for the mechanical tests.

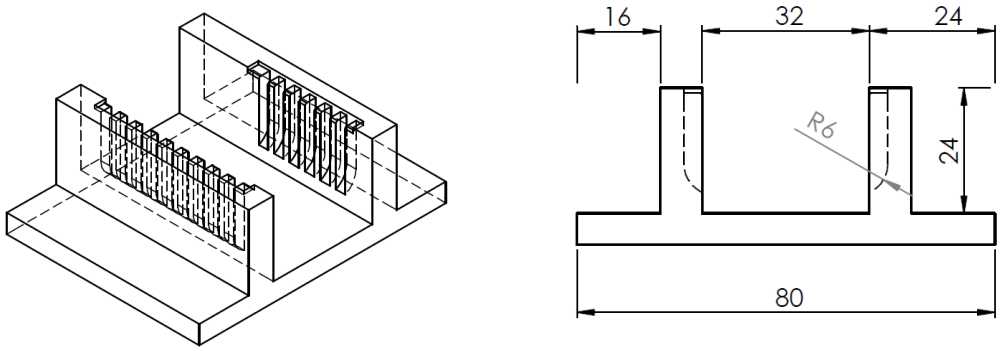

(a) 3D view

(b) Front view with dimensions

Figure 3.20: Excerpt from the technical drawing of the custom fixture (see Appendix B).

3.4.2 Three-point shield bending test

The parts tested are samples from T&R packaging (all shields are received from the supplier and therefore packaged in the same way). These samples are, by experimental consideration, assumed to be "ideal" before testing (as we will see, this is not quite the case with some of the dimensional measurements carried out before testing), and so it is vital to ensure that the parts tested are those least likely to have geometric defects, i.e. samples taken from the beginning of the reel. Ideally, these are the first parts, but due to resource constraints, one single reel was used for these tests. As initial tests were inconclusive, leading us to use more parts than originally planned, from the rest of the tape. However, the parts used did not come from further than the first 20% of the reel.

The three-point shield bending test aims to reproduce, under different loads, the type of loading permitted within the strip wound on the reel. In doing so, multiple shields in different states of deformation could be reserved for optical measurements post-bending. The same measurements must also be performed before the test, due to the potential imperfection of the initial shield planarity. In that way only can we have a comparison basis for our results. All the optical measurements follow the

same method as what was described in section 3.1.1.

Cyclic loading

A program running gradually increasing load cycles provides information on the elastoplastic behavior of the part.
The gradual increase of cycle load is defined by setting a maximum load and a number of intermediate loads, distributed evenly between 0 and the maximum load. For this test, maximum load has been set to 30 N, with 3 intermediate loads: 7.5 N, 15 N, and 22.5 N. The velocity of displacement is set to 1 mm/min. The choice of such parameters is clarified in the next subsection. Each cycle is repeated 5 times.

For a matter of repeatability, the test has been performed on 2 different shield samples. The curve obtained through the test on sample n°2 is displayed in Figure 3.21. Important information on both tests is given in table 3.6 below.

Part n°	Maximum charge [N]	Compression displacement at max. charge [mm]
1	30.06	0.39
2	30.13	0.37

Table 3.6: Results of the cyclic loading test on 2 shield samples.

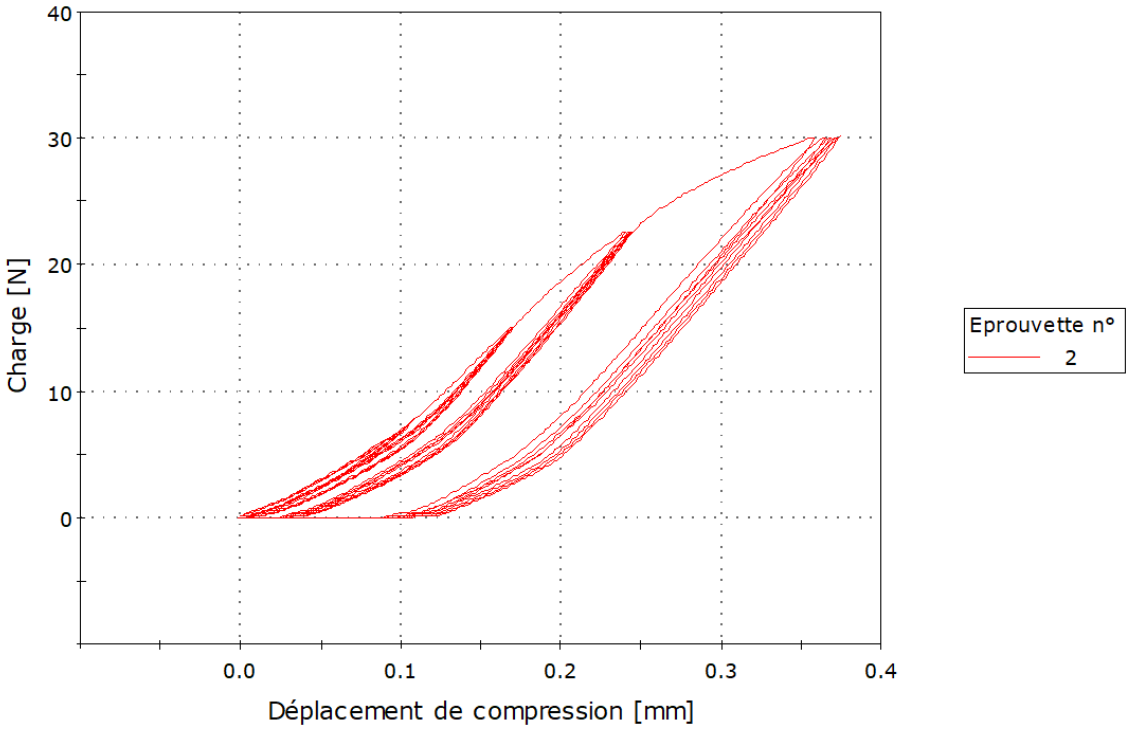

Figure 3.21: Load against compression displacement throughout the cyclic loading test (sample n°2).

Note that the vertical axis here is the effort, which is driven, it is not the compression stress in the direction of displacement. In the same way, the vertical axis is

not a dimensionless deformation ($\Delta L/L0$) but the actual displacement of the compression tool.

This test sheds light on the elastoplastic behavior of the shield when bent like so. Indeed, we can see that the part plasticizes between each group of 5 cycles, as each relaxation leaves a residual plastic deformation at zero load. This gives rise to a bending hardening of the zone that bears deformations. We can also stipulate from these results that, rather than a precise point corresponding to yield strength, there seems to be a transition phase between elastic and plastic behaviors (gradual formation and increase of a horizontal gap between cycle curves).

It is also empirically verified that the mechanical behavior of the part is not purely elastic (or elastoplastic). There is a certain viscosity, highlighted by the presence of subtle hysteresis. Several rheological models have been developed in the literature to theorize these behaviors of materials. Examples include Maxwell, Kelvin-Voigt, and Zener, among others. Although the exploration of these models is too long to be done in this study, it may be interesting to take this aspect into account when solving problems related to unwanted deformation of parts.

To simplify the approach, and because we do not have the necessary resources to study the evolution of the bending stress at the point of bending compared to the imposed bending moment, we will assume that the studied behavior is elastoplastic (linearity will not be a necessary assumption).

Based on the two samples tested with cyclic loading and on this elastoplastic hypothesis, it can be said that the yield strength of a shield under these conditions is approximately 15 N, which corresponds to the load at which a horizontal gap between cycle curves begins to appear (see Figure 3.21).

Bending tests by force-driven compression displacement

These tests allow the analysis of the mechanical response of the part to several imposed forces, reached by the tool after its displacement at a set speed.

Different speeds were tested (Figure 3.22), allowing to choose a displacement speed considered reasonable, *ie.* a good compromise between the approximation of quasi-static conditions, and reasonable test duration. In this diagram, test sample n°1 (light red) corresponds to a 55 mm speed, while the other samples correspond to a 1 mm/min, which is the tool velocity that was selected for all the tests, for the reasons stated above. In fact, sample n°1 was deformed in such a way that even the pseudo-beam EG (see Figure 2.1, section 2.1.2) was bent.

The loads were chosen according to the force response of a displacement imposed on the part, at the same speed of 1 mm/min. Indeed, an adjustment test was made beforehand to identify the "interesting" forces in terms of information about the behavior of the part. This adjustment test is driven in motion, that is, the compression tool stops its movement when the set displacement is reached. Of course, care has been taken not to exceed displacement values that are too high and impractical

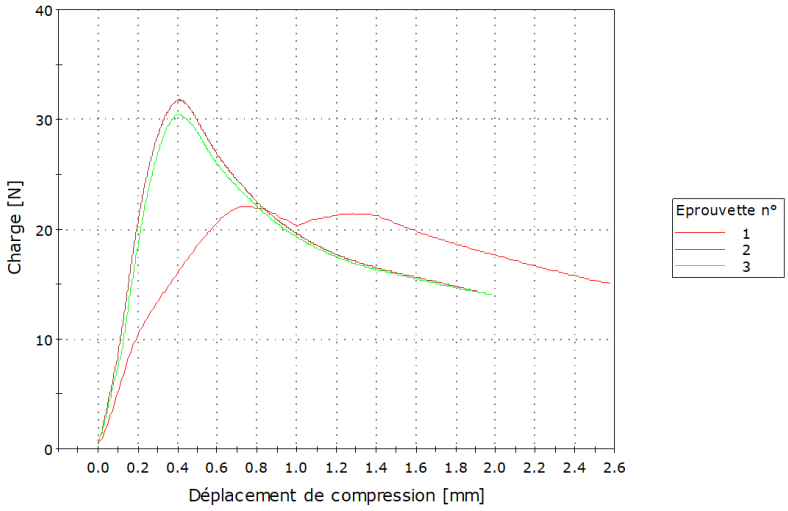

Figure 3.22: Influence of the displacement speed on the mechanical response.

Spec. n°	Aim displ. [mm]	Max. charge [N]	Displ. at max. charge [mm]
21	0.1	8.00	0.10
22	0.1	8.00	0.10
23	0.2	19.00	0.19
24	0.2	19.00	0.19
25	0.3	28.00	0.30
26	0.3	28.00	0.30
27	0.3	28.00	0.31
28	0.4 (load not reached)	30.46	0.39
29	0.4 (load not reached)	30.90	0.39
30	0.4 (load not reached)	30.85	0.40

Table 3.7: Test data: compression displacement on 10 lone shield samples.

in practice in the packaging: the majority of the stress values retained for the test remain in match with a realistic displacement range given the clearance existing in the packaging compartment.

Although this method may seem convoluted, it will be very useful, especially in the section dealing with packaging trials (following section). Indeed, in these cases, we have no way of knowing the deformation of the tested samples (inside their packaging), before carrying out new optical measurements at the end of the tests. This enables us to compare the desired compression displacement (estimated via the fit test) with the actual deformation of the part in its compartment. In this way, we can study factors such as the clearance experienced by the part in the packaging, and the influence of the latter on the problem at hand.

Thus, from the force adjustment test (itself displacement-controlled), we were able to deduce the various test loads to be applied. These loads are in fact defined as the maximum force imparted by the part to the tool in reaction to its displacement at the speed of 1 mm/min (see Table 3.7).

Repeatability was assured by at least doubling each test for each tested sample,

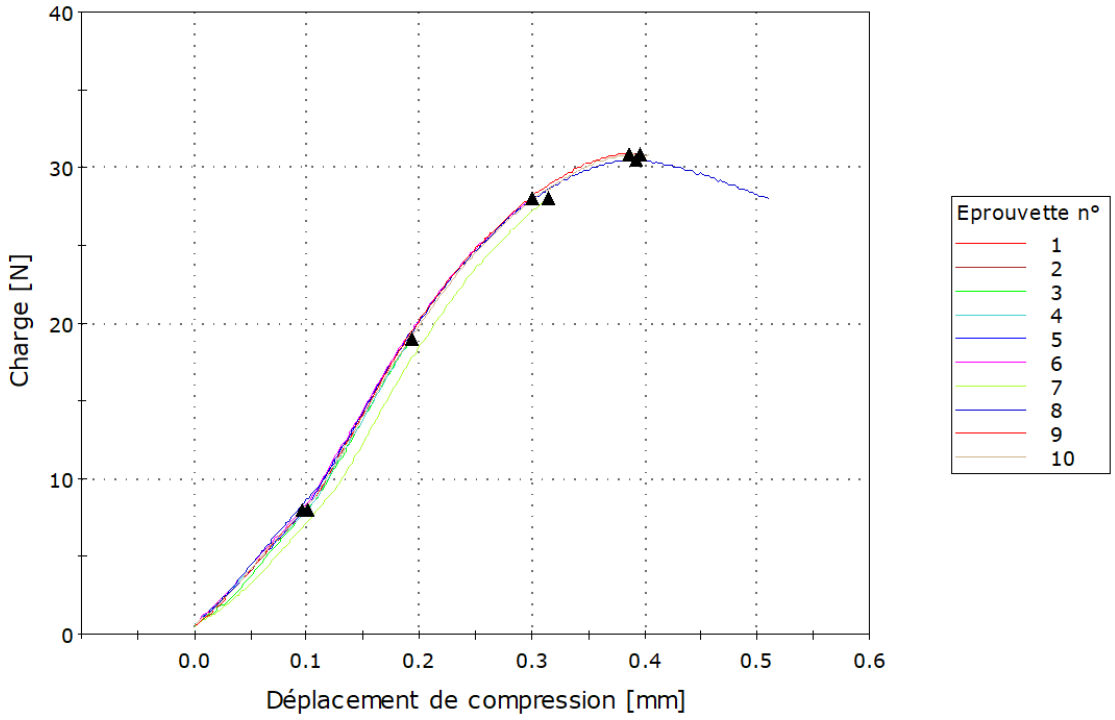

Figure 3.23: Compression displacement on 10 lone shield samples.

with improved repeatability for higher loads (3 tries).
From the emerging results, it can be said that the critical load for the shield alone (*i.e.* plastic deformation threshold) would be of 30 N.

Below are the measured values of coplanarity before and after test for every sample (Table **??**):

Specimen	Coplanarity before	Coplanarity after
21	-0.106	-0.112
22	-0.111	-0.116
23	-0.110	-0.127
24	-0.115	-0.116
25	-0.115	-0.146
26	-0.104	-0.126
27	-0.092	-0.115
28	-0.110	-0.957
29	-0.117	-0.319
30	-0.092	-0.273

Table 3.8: Maximum vertical deviation (coplanarity) for each sample before and after bending test.

This observed deformation magnitude is far less than predicted by the simple theoretical model built in section 2.4.2 (0.15 mm versus 2.55 mm for a 30 N load). This model was hugely limited and could only serve to show that relatively significant deformation was possible with such type of structure by applying only a load

of a couple of newtons at a specific sensitive point.

The 3-point bending tests on the shield alone give valuable insight into the characteristics of the deformation process giving the observed result. However, a shield-only approach has many limits, in particular when considering that the contact zone between the tool and the shield is strongly localized, where the real contact occurring via the interaction between the plastic packaging and the shield inside it remains quite unknown to us. The design of the tool and the defined contact zones gave way to strong bending of the sheet metal of anchor brackets around the contact area, due to the instability of the contact. This phenomenon is visible in Figure 3.19 picturing the result of the test using the first fixture (similar result around this area with the definitive fixture).

To recreate an almost identical deformation, we imagined a protocol for carrying out mechanical tests on the shield within its packaging.

3.4.3 Influence of the packaging

In order to test the whole {shield + packaging} assembly, the idea is to apply similar compression displacement to the piece *via* line contact with the exterior of the packaging at mid-width. Only in this way can the defect reproduction be satisfactory. Then comes the issue of the boundary conditions known by a single compartment in the tape: if a compartment is virtually isolated, there is a symmetry of tensile conditions on either side of the compartment (continuity of the tape).

Achieving the desired boundary conditions for this packaging test is a real challenge. The bending fixture must allow a z-stop on either side of the compartment, while at the same time limiting displacements of the tape in the area adjacent to the cut-out, which would counteract the effect of tension along the entire length of the tape. Ideally, we could imagine a quasi-embedded condition across the cut thickness of the plastic tape, leaving room for movement that is nonetheless constrained by the tape's inherent tension. In this way, we can create a "viscosity" model of displacement (see Figure 3.24).

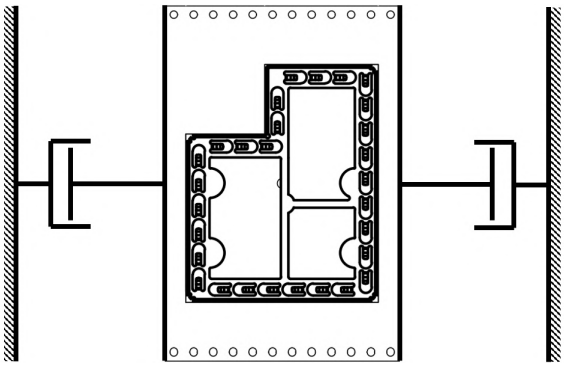

Figure 3.24: Quasi-embedded theoretical model for test boundary conditions.

To achieve a setup as close as possible to the desired conditions, a setup selection test was carried out. Firstly, the tool geometry was changed to a cylinder to have

linear contact, changing to cylindrical surface contact in the case of deformation of the packaging following the tool's shape. Indeed, the rectangular (parallelepiped) tool previously used to apply the load to the shield's anchor brackets now sinks into the plastic compartment like a blade: the contact surface does not adapt (increase) with the deformation of the packaging plastic.

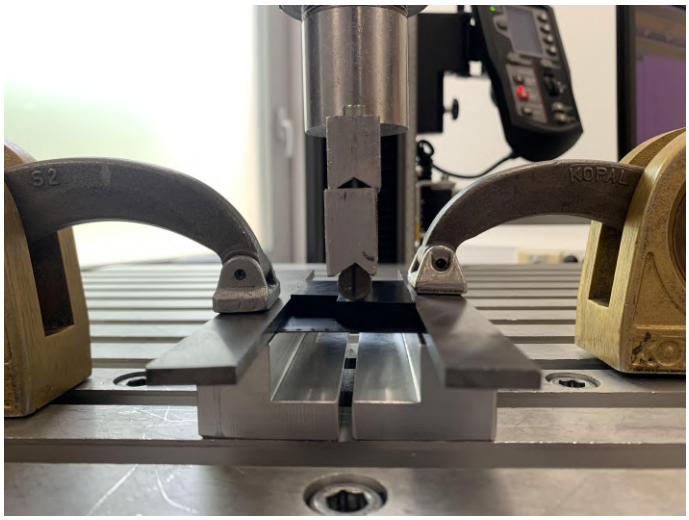

Figure 3.25: First fixture setup assessed for tests with packaging.

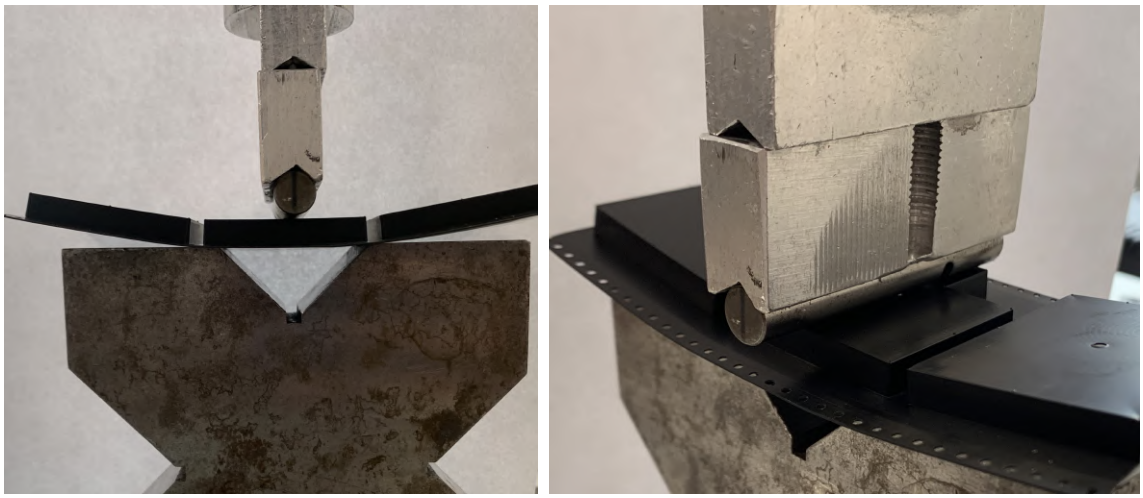

Figure 3.26: Second fixture setup assessed for tests with packaging.

The first fixture tested is the machined fixture used in the first test on the shield-only setup. The z-stop coupled with x-symmetry were addressed by constraining the tape sides with clamps applying force to steel plates, thus distributing the force over the maximum possible tape surface (see Figure 3.25).

The second fixture tested is a steel block with an X geometry (that was available in the lab), thus allowing for the z-stop, but not taking into account the symmetry achieved in practice by the continuity of the tape. However, we decide to keep the tape portions (compartments) adjacent to the shield under test. In this way, we can

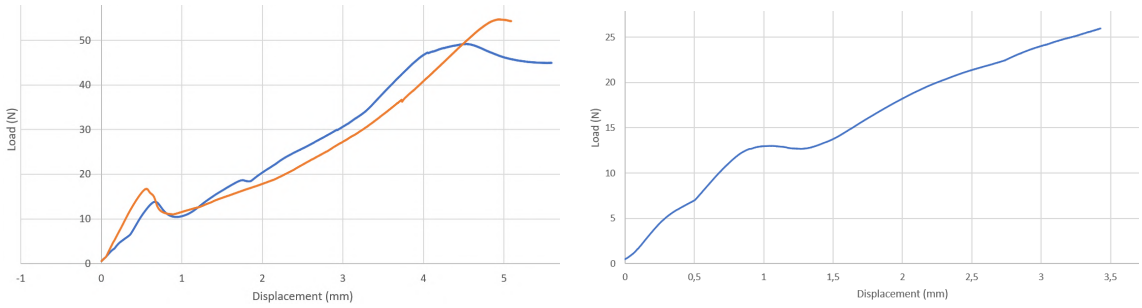

(a) First setup (b) Second setup

Figure 3.27: Setup assessment results.

even test several consecutive pieces of the tape portion removed from its reel, as the applied loading in no way affects adjacent shields (the latter are simply carried away by a global displacement of the tape due to bending of the current part).

Despite a possible lack of precision for the z-stop position definition (only visual positioning of the samples on the fixture, as there is no guide), this second installation provides a mechanical response that we believe to be more reliable. Indeed, this setup recreates the conditions of "quasi-embedment", as displacement of the edges of the packaging on either side of the tested sample is still permitted however under some tape tension. In contrast, the first setting produces a disproportionate force, while the deformation of the assembly is already well underway, before decreasing through secondary plasticization of the tape's plastic structure. This is interpreted as the effect of tape tension (inter-compartment) until plasticization, which obviously does not occur within the reel.

The presence of the compartment in which the shield is conditioned adds a certain amount of rigidity to the system under test. It is therefore expected that the loads required for the same compression displacement of the tool will be increased in comparison to earlier tests on shields alone. A supplementary adjustment test must therefore be carried out to correctly select the forces applied (same strategy as in the last section).

However, the information of interest remains the deformation of the part itself. It will be difficult to follow the response of the shield alone within the compartment when the loading is applied to the whole. For this reason, post-test dimensional measurements will be essential to conclude on the impact of the tested loading on the part geometry, as already explained.

From the adjustment test, we defined the series of loads applied to the test samples, summarized in the table below (Table 3.9). Repeatability is assured by the test being done on two different samples each time (with sufficient consistency between the two).

These results show that the first stress drop occurs when the reaction force reaches about 13 N, which is much lower than the critical load before plastic deformation by a shield alone (30 N, see section 3.4.2). We can identify this drop to the giving way of the plastic structure of the compartment. Indeed, at this time of each

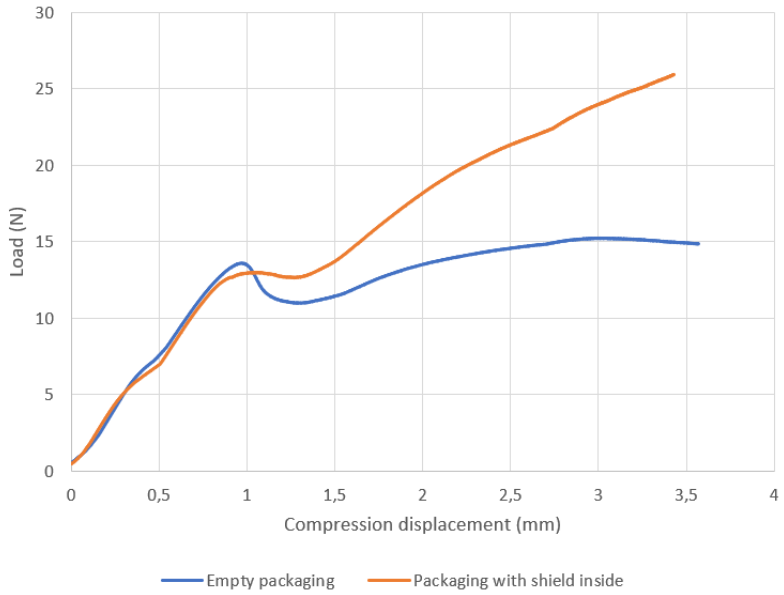

Figure 3.28: Comparison of the load against compression displacement behaviors of an empty pocket and of one containing the shield.

Specimen	Max. charge [N]	Compr. displ. at max. charge [mm]
31	15.00	1.55
32	15.00	1.52
33	22.50	2.48
34	22.50	2.36
35	30.00	3.49
36	30.00	3.71

Table 3.9: Test data: compression displacement on 6 samples of shields within their packaging.

test, we could visually spot white traces below the load application point, testifying the plasticization of the compartment.

The load take-up by the shield's structure only occurs at the rise of the curve. The slight decrease in force between the two local extrema reflects the catching up of mechanical clearance in the compartment with compression displacement. This interpretation can be supported by the diagram in Figure 3.28, which shows the difference in the load against displacement behaviors of empty and full packaging.

The diagram in Figure 3.30 roughly illustrates the best interpretation that can be made of these results matching the observed deformed shape (not only on production runs but also with the optical measurements carried out subsequently to the tests).

The final deformed state depicted on this diagram is at the end of compression, **before relaxation**. The tool makes contact with the packaging, starting the compression movement. When the tool finally comes into contact with the shield, deformation of the latter begins, with bending along two axes. The first bending direction (x-axis) arises from the conditions imposed by global positioning, and the

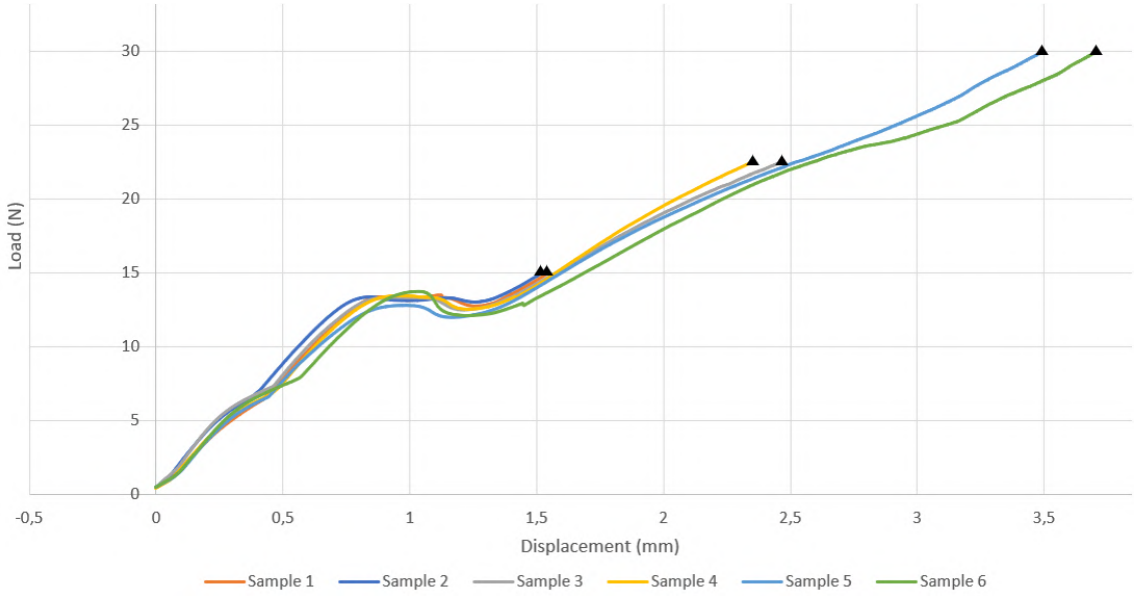

Figure 3.29: Results of the bending test on the {shield + packaging} assembly.

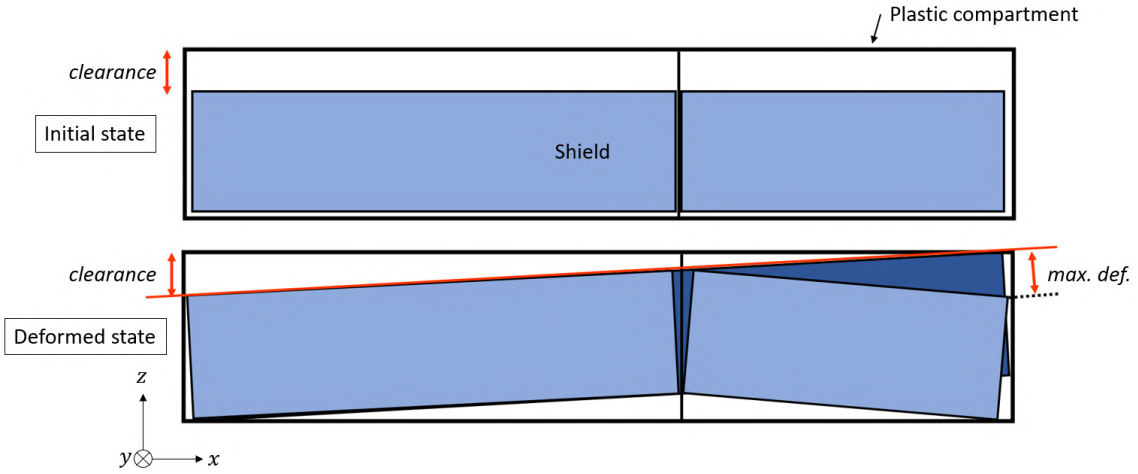

Figure 3.30: Interpretation of the intra-packaging shield deformation mechanism from test results.

second (y-axis) is implied by the uplift of the entire structure as Points B and F (see section 2.1.2) are pressed against the bottom of the packaging compartment.

In this model, the vertical compression displacement needed for the tool to deform the shield to a certain amount will thus be slightly shifted compared to this deformation, in addition to the clearance offset. To estimate that shift, additional information is needed on the clearance and range of movement permitted by the plastic film, which are the parameters that limit the vertical movement of the shield in its compartment. We were unable to estimate these factors in the time available.

As we zoom in on the maximum deformation (see Figure 3.31), we understand that the maximum deformation seen by the shield here is the sum of elastic deformation and plastic deformation. The coplanarity value extracted from optical measurements is in fact exactly the same as plastic deformation, as it is the result-

ing deformation after relaxation of the load, measured orthogonally to the shield's seating plane.

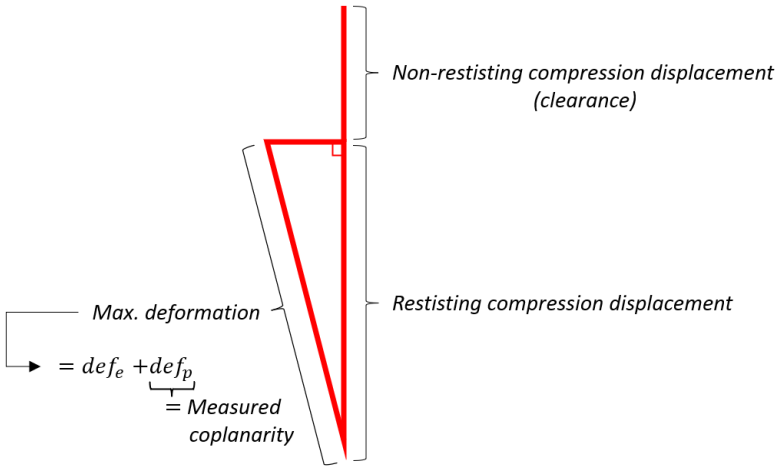

Figure 3.31: Link between the displacement of the tool, the part deformation, and the measured coplanarity.

Below are the listed values of measured coplanarity (after the test) for the samples tested (Table 3.10). As seen before, initial coplanarity is not perfect even if the shields have been picked on the outermost tape layers. However, we cannot measure the coplanarity before tests in this case because shields must remain inside the packaging, whose opening is irreversible and might expose the shield to exterior actions. Thus, in the same way than observed in section 3.1.1 and 3.4.2, we assume that average initial coplanarity is of about 0.1 mm.

Specimen	**Coplanarity**
37	-0.147
38	-0.152
39	-0.712
40	-0.625
41	-1.510
42	-1.660

Table 3.10: Maximum vertical deviation (coplanarity) for each sample after bending test.

These results imply that any load greater than a value slightly above 15 N would give rise to a deformation exceeding the 200 μm manufacture tolerance for shield planarity. However, from the assumption that all parts where the shield anchor brackets are not correctly reflow soldered (solder paste plunge defect) are rejected, we also deduce that any deviation from the seating plane greater than the solder paste thickness will be rejected. This thickness being set to 150 μm, the coplanarity values obtained for a 15 N load would certainly cause the shields to give rise to scraps.

Chapter 4

Solution suggestion and assessment

4.1 Requests for new packaging to the supplier

4.1.1 Needs and suggestions

To potentially see progress over the course of the internship, suggestions were formulated and communicated to the supplier rather early in the process, on the basis of conclusions issued from the first field observations carried out. In fact, the majority of the work has been made during summer and was therefore impacted by a slowdown in all activities, which is all the more marked when it comes to communicating with a foreign external player.

The first action to take naturally revolves around the idea of inhibiting the deformations observed on shields originating from the last 20% of reels. This led to a suggestion for having a critical radius R_{crit} of tape winding, following the reasoning explained below.

Let us name R_1 the estimated radius where is located the last tape layer containing components, and R_2 the radius of the first layer of tape (reel outer surface). A 10 mm margin will be considered for R_1 in comparison to the inner radius of the reel. The radius corresponding to the 20% limit will be named $R_{20\%}$.

$$R_1 = 72 + 10 = 82\,\text{mm} \tag{4.1}$$

$$R_2 = 190\,\text{mm} \tag{4.2}$$

To calculate the number of components concerned by the last 20% of the reel, we will calculate the area taken up by that percentage in the axial plane (y, z).

$$\pi(R_{20\%} - R_1) = 0.2 \times \pi(R_2 - R_1) \tag{4.3}$$

$$\Rightarrow R_{20\%} = 0.2(R_2 - R_1) + R_1 \tag{4.4}$$

$$\Rightarrow R_{20\%} = \sqrt{0.8 \times R_1 + 0.2 \times R_2} = 112.25\,\text{mm} \tag{4.5}$$

Since $R_{crit} \leq R_{20\%}$, we arbitrarily choose to add a 1.75 mm security margin to make the critical radius round up to $R_{crit} = 114\,\text{mm}$.

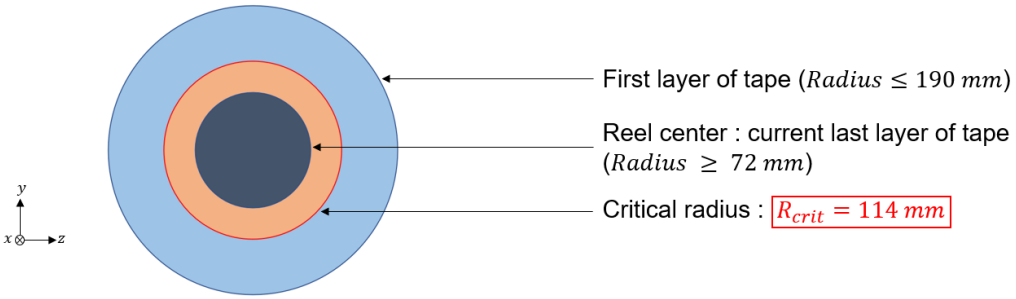

Figure 4.1: Important radii of the conditioning reel, highlighting the critical radius.

This leads to two possible actions, either:

- Opting for larger reels while maintaining the same quantity of components inside of them[1].

- Keeping the reel dimensions as is, while increasing the number of empty pockets towards the reel end.

Any such modification would have to be subjected to a profitability study, based on the assumption that the revenue loss from scraps is compensated, though that aspect will not be elaborated here. The decision between these two options, or a combination of both, should be guided by careful consideration of logistical implications and cost-effectiveness, ensuring that the chosen strategy aligns with the overall objectives and constraints of the project.

Thus, directions were given to the supplier, underlining that an improvement in scrap should be observed by respecting the critical radius, as well as by stiffening the plastic tape. At the time, no further information had been found on how to stiffen the tape.

4.1.2 Specifications of the test T&R

After some time, feedback was given that a test reel had been sent to Continental. This reel had undergone a few modifications compared to the one currently used.

Firstly, the supplier had taken the initiative of emptying the last 20 pockets at the end of the reel, as a response to previous complaints. On a side note, this barely changes the radius of the first tape winding (R_2). Furthermore, implementation of

[1]This solution poses an issue with the Continental logistics flux, which will need adjustment in order to allow the processing of bigger reels. Indeed, storage trays in which reels are conveyed cannot accommodate reels with a radius larger than 200 mm. However, larger reels are used for specific products, so the possibility of such an adaptation would be conceivable.

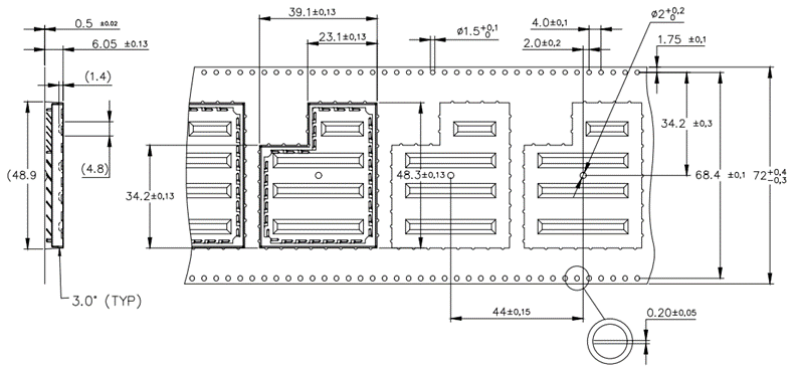

Figure 4.2: Excerpt from the technical drawing for the new version of T&R packaging suggested by the supplier (full drawing available in Appendix B).

this modification had already been scheduled for future deliveries. However, the number of empty pockets on this new version is far from sufficient to clear the area covered by the critical radius (about 50 components) and get rid of the 20% issue.

Secondly, the need to stiffen the tape was answered in this first draft for solution, by a change of the T&R specifications. An excerpt from the new technical drawing for the T&R packaging is shown in Figure 4.2 (the full drawing is available in Appendix B).

In principle, the modifications made should contribute to inhibiting the effects of bending within the reel. Indeed, the addition of stiffening shapes on the bottom of the tape compartment acts on its bending rigidity in the winding direction. Additionally, small stiffeners were added all around every tape compartment wall (see Figure 4.3).

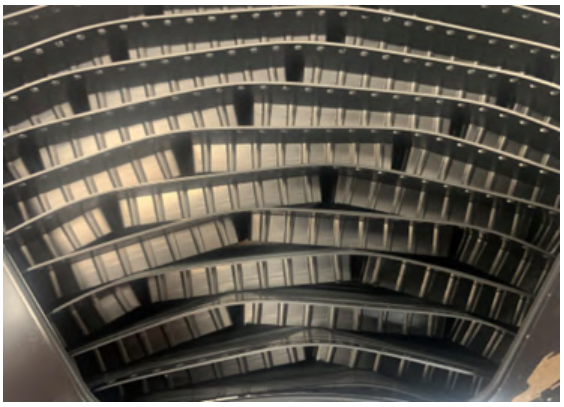

(a) Side view of the reel layout.

(b) Bottom view of one tape layer.

Figure 4.3: New (test) packaging.

4.2 Test of the new packaging

4.2.1 Production test

The test reel received from the supplier was incorporated into a production test, having extracted a small portion from the beginning of the tape for mechanical testing. Unfortunately, the batch produced using this reel yielded highly unsatisfactory results (see Figure 4.4[2] or Table 4.1). The outcomes fell short of expectations, prompting a need for a thorough analysis of the test packaging to potentially discover what prevented this production test from being effective.

It should also be kept in mind that all the analyses that were possible with this test packaging had to be carried out with a single unit of the new reel, which underlines the importance of the uncertainty associated with the results obtained.

Position bobine	Reste	% Bobine restant	Type de défaut	BISAC four	Amplitude avant four	Défaut présent en sortie de ligne ?	Amplitude
52	198	79,2	1	13h39	0	non	
163	87	36,3	1	15h18	0	non	
164	86	35,8	2	15h19	1	non	
165	85	35,4	3	15h20	2	non	
179	71	29,6	1	15h25	0	oui	0
180	70	29,2	1	15h26	1	oui	1
181	69	28,8	1	15h26	0	oui	0
195	55	22,9	1	15h36	0	non	
196	54	22,5	1	15h37	1	oui	2
197	53	22,1	1	15h37	1	oui	2
198	52	21,7	1	15h42	0	oui	0
208	42	17,5	1	15h52	2	oui	3
210	40	16,7	1	15h54	1	oui	1
211	39	16,3	1	15h54	1	non	
212	38	15,8	1	15h57	2	oui	2
213	37	15,4	1	15h57	1	oui	3
214	36	15,0	1	15h58	0	non	
224	26	10,8	1	16h02	2	oui	2
225	25	10,4	1	16h02	2	oui	3
226	24	10,0	1	16h03	3	oui	4
227	23	9,6	1	16h03	1	oui	1
237	13	5,4	1	16h07	1	oui	2
238	12	5,0	1	16h09	2	oui	3
239	11	4,6	1	16h09	3	oui	3

Figure 4.4: Statistical data from the production run using the new (test) packaging.

From this production run statistical data can be extracted, in particular the defect rates below (Table 4.1), equalizing the defect rates obtained with the usual packaging during initial production runs.

Component position (p)	**Defect rate**
$p \in [0\%; 10\%]$	2.0%
$p \in [10\%; 20\%]$	3.2%
$p \in [20\%; 30\%]$	2.4%
Total	**6.8%**

Table 4.1: Production run defect rate analysis for the test packaging.

[2]Columns from left to right: Position in reel, Number of shields remaining in reel, % of reel remaining, Defect type, BISAC oven, Amplitude of deformation before oven (from 1 to 5), Presence of the defect at oven output (yes/no), Final deformation amplitude).

4.2.2 Mechanical tests

To evaluate the new packaging and compare it accurately with the existing packaging already tested, we need to adopt the same test parameters and reproduce the conditions set up for the shield tests in the packaging identically.

Given the rather unsatisfactory production test, we anticipate the new packaging to fall short of expectations on the mechanical tests as well. However, we can deduce from the diagram in Figure 4.5 that the new tape design ensures a much higher bending yield stress, *ie* higher capacity of deformation before yielding under bending stress. In contrast, what the new tape design does not significantly modify is the bending rigidity (or stiffness) of the packaging (slope of the first linear phase of the curve).

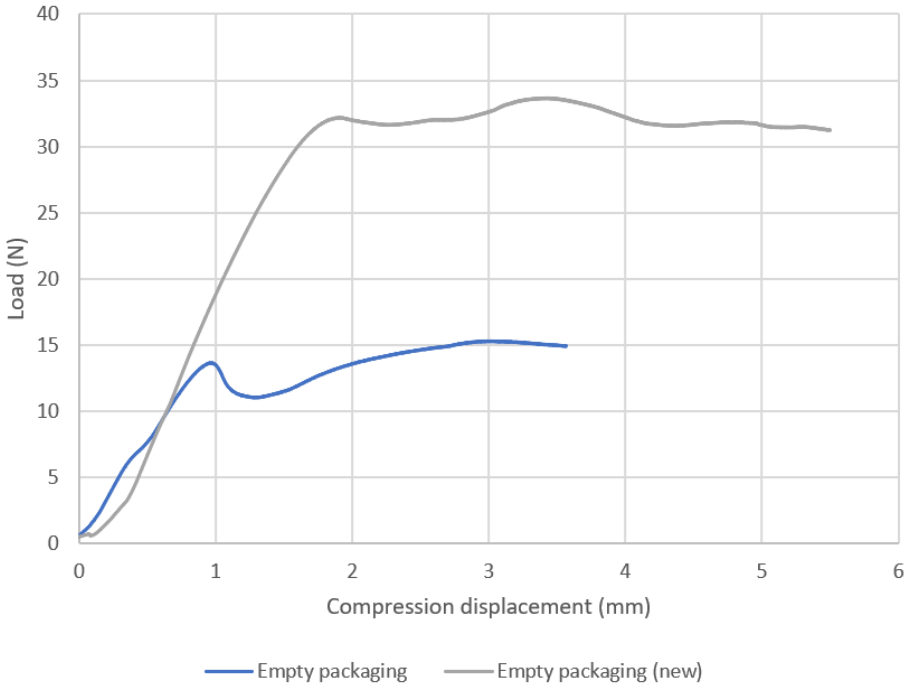

Figure 4.5: Comparison of the load against compression displacement behaviors of an empty pocket for the usual and new packagings.

Below is a Diagram showing the resulting deformation curves for all bending tests carried out with the {shield+packaging} assembly, including the original packaging tests analyzed in the previous Chapter (section 3.4.3). On this diagram are written some interpretation notes as regards the stages of deformation.

By the time the plastic tape gives way, the critical load for the shield alone (30 N) has already been exceeded, meaning that the shield already takes up part of the effort by deforming.

Based on the estimates made in Table 4.2, we can graphically represent the evolution of the final coplanarity against the maximum imposed load (Table 4.7), and eventually, the evolution of the range of the shields' elastic deformation against maximum load applied, as tools for comparing the two types of packaging in terms

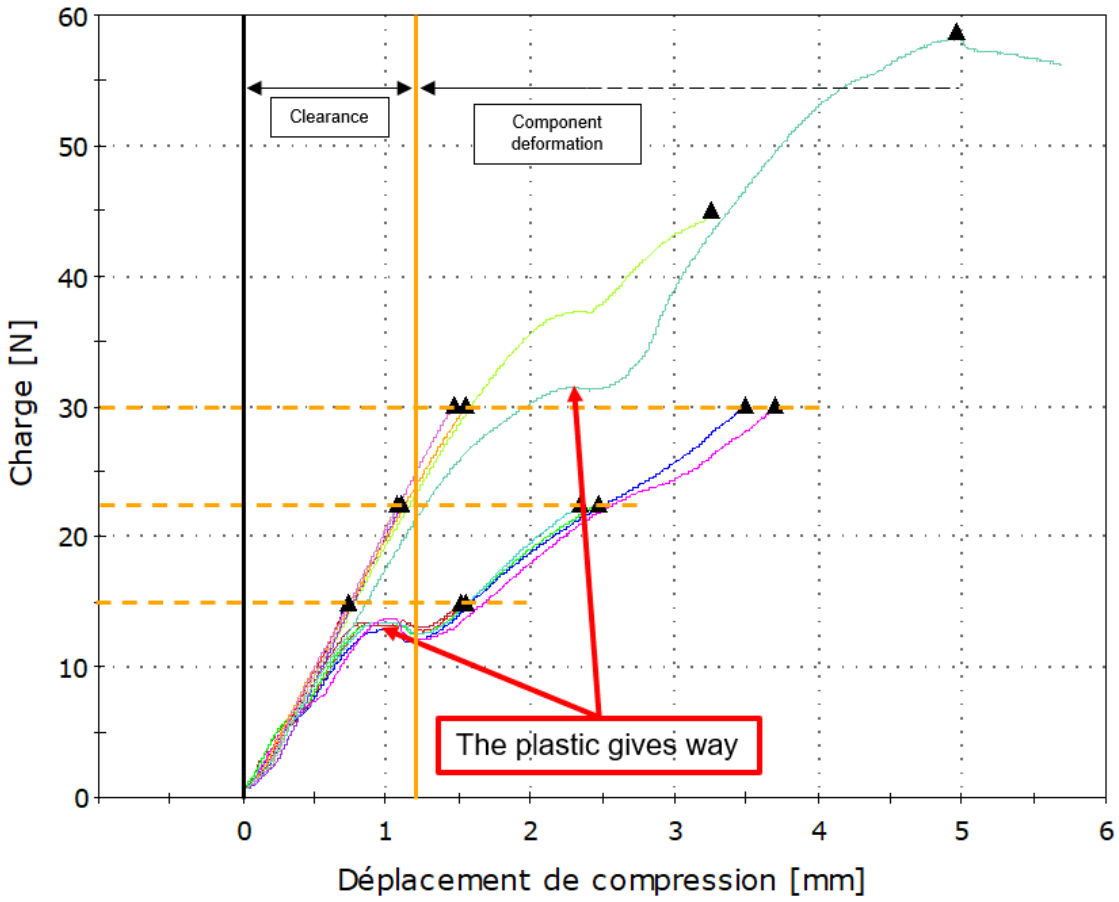

Figure 4.6: Results of bending tests on the {shield+packaging} assembly (original and test packaging).

of the mechanical behavior they impart to the {shield+packaging} assembly.

A first interpretation is that, despite the expectations raised by the production results and the interpretation of the mechanical test on the empty test packaging, the quality of the deformations estimated on the shields coming from the test reel has clearly improved (see Figure 4.7), compared with the results given by the existing packaging. That is because the mechanical tests have been compared using exact same loading conditions. Indeed, given that the new packaging has a higher bending yield stress than the original packaging, the maximum imposed load for the test runs is reached at lower deformation levels (see Figure 4.6).

Secondly, a curious result visible on the diagram in Figure 4.8 leads us to understand that the elastic deformation range of the shield in its packaging would evolve with the maximum load applied to the assembly. While the result is somewhat surprising, further exploration is not feasible due to the lack of a clear understanding of its implications. Moreover, it is not the primary issue that has been identified and requires immediate attention.

In a nutshell, the new packaging suggested by the supplier may have higher bending yield strength, giving it a higher capacity to take up bending stress before

Existing packaging	**Specimen n°**	**31**	**32**	**33**	**34**	**35**	**36**	
	Max. load [N]	15	15	22.5	22.5	30	30	
	Total comp. displ. [mm]	1.54743	1.52224	1.47503	2.35525	3.49122	3.70881	
	Coplanarity [mm]	0.147	0.152	0.712	0.625	1.51	1.66	
	Measured clearance[3] [mm]	1.25561	1.24224	1.20876	1.21717	1.17397	1.22553	
	Max. shield def. [mm]	0.29182	0.28000	1.26627	1.13808	2.31725	2.48328	
	Elastic def. [mm]	0.14482	0.12800	0.55427	0.51308	0.80725	0.82328	
Test packaging	**Specimen n°**	**37**	**38**	**39**	**40**	**41**	**42**	**43**
	Max. load [N]	15	15	22.5	22.5	30	30	58
	Total comp. displ. [mm]	0.73303	0.74259	1.07734	1.11242	1.55424	1.46957	5.59439
	Coplanarity [mm]	0.086	0.080	0.109	0.092	0.16	0.106	1.290
	Estimated clearance[4] [mm]	1.2	1.2	1.2	1.2	1.2	1.2	1.2
	Max. shield def. [mm]	0	0	0	0	0.35424	0.26957	4.49539
	Elastic def. [mm]	0	0	0	0	0.19424	0.16357	3.20539

Table 4.2: Estimation of several quantities such as the clearance inside packaging and the elastic deformation for each specimen tested.

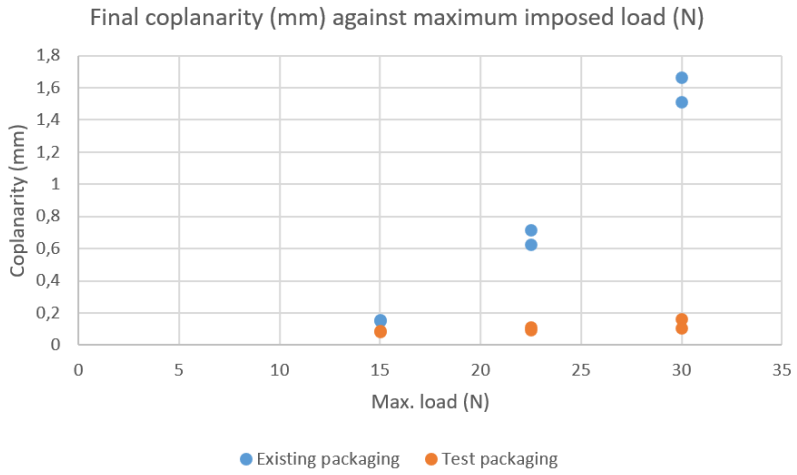

Figure 4.7: Comparison of final coplanarity against maximum load for the two sample groups (from the original and test packaging reel).

giving way and letting the plastic tape deform locally and in an irreversible manner (plastic deformation). Still, its rigidity has not increased sufficiently to prevent the reel's inner-loading from imposing deformation on the components themselves.

4.2.3 Conclusion

What can be drawn from these mechanical studies is that in some cases - and this seemed to be the case for the test reel sent by the supplier, given the production results - the reel is wound in such a way that the tape tension produces an axial stress greater than that required to deform the component contained in certain compartments, especially those located in the last 20% or 30% of the reel. As for the exact value of this axial force, it cannot be known, since winding torque (leading to tape tension) is not set constant by the supplier (see section 1.3.1).

Looking at the results displayed in Figure 4.6, we can imagine that a more effective way to prevent this phenomenon would be to increase the stiffness of each segment of the plastic strip, rather than a modification of the design resulting in an increase in bending yield stress.

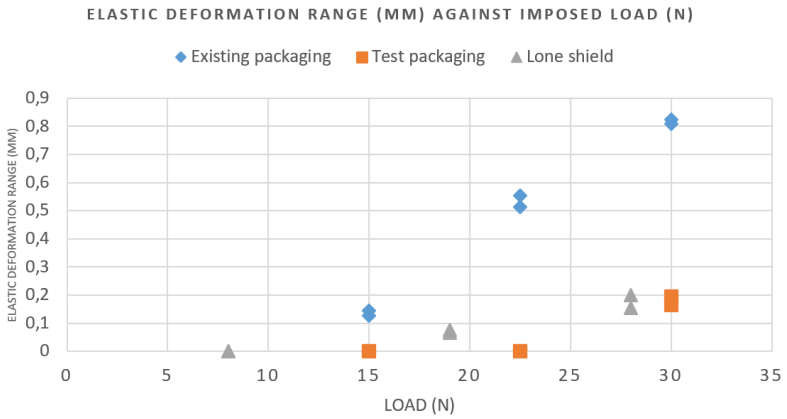

Figure 4.8: Computation of the range of elastic deformation for each packaging type against the maximum imposed load.

Moving forward, exploring alternative directions becomes imperative to formulate a more satisfactory and definitive solution. One potential avenue is to collaborate closely with the supplier to fine-tune the packaging's characteristics and design, seeking a balance that not only augments bending yield strength but also effectively addresses the rigidity concerns. Additionally, considering modifications in the manufacturing process or exploring alternative packaging designs may present viable paths for improvement. The ensuing sections delve into these potential directions, aiming to chart a course toward a robust and optimized solution that ensures the integrity of the components throughout the production life-cycle.

4.3 Directions for a future solution

As we delve into the next section, it is relevant to step back and gain a holistic perspective on what is the underlying issue we are looking to solve in this study.

For instance, as hinted in the state of the art presentation section (in particular section 1.3.1), winding torque is apparently not monitored during the supplier's packaging process, after the manufacturing of shields. Yet, the whole of the study is based on the hypothesis that the root cause of the defect is the inner-reel loading conditions (geometrically aggravated at the end of the reel), originating from tape tension and thus winding torque. This explanation clarifies and gives resonance to the flawlessness of the supplier's control measures, intended to justify the quality of the parts and respect of specifications. Indeed, these control measures could only have been carried out upstream of packaging, therefore completely disregarding the entry into play of the following crucial phases of the product life cycle, taking place between component manufacturing and delivery.

Thus, one unconditional specification has to be made, which is the need to monitor the winding torque upon reel winding for packaging. No matter the final design of the component and/or of the tape, this winding torque must not exceed the value corresponding to the critical radial force provoking the component bending at the reel center. This value for the current packaging is of about 15 N, it may vary de-

pending on design choices.

4.3.1 Exploring various packaging types

The suggestion to monitor the winding torque is only relevant for reel-type packaging. However, although this type of packaging solution is by far the most common for electronic components intended for PCB assembly during the SMT production phase, it is not the only solution available. Thus, the geometrical and mechanical specificities of the BSRF EA's EMI shields could lead us to be interested in other conditioning modes, such as packaging in trays (illustrated on Figure 4.9).

In such a packaging solution, the components are carefully arranged within solid compartments, taking into consideration factors such as size, shape, and orientation. In the conditioning process, components are often loaded into the tray using automated equipment to minimize the risk of damage. The conditioned tray acts as a protective housing for the components, maintaining their integrity and preventing physical damage. This organized arrangement facilitates efficient handling during subsequent stages of the manufacturing process, such as the pick-and-place operation in SMT assembly.

The key distinction lies in the handling mechanism: while reel packaging involves the continuous feeding of components, tray packaging requires the machine to navigate and select components individually from their designated pockets. This tailored approach in tray packaging ensures careful handling and precise placement of components, contributing to the accuracy and efficiency of the SMT assembly process.

Tube conditioning is also one of the possible choices for component packaging (see Figure 4.9), but this type of packaging requires the following components to physically touch and bump into each other inside stacked tubes, also allowing a continuous supply of components to the placement machine. This conditioning type is more suitable for stiff and solid components that are not prone to deform under common amounts of mechanical stress.

4.3.2 Revision of design philosophy

Short-term

A revision of the design philosophy will eventually be necessary, giving greater weight to certain phases of the product life-cycle, such as packaging, transport, delivery, and supply chain, but also taking into account packaging methodology. However, short-term actions, which cannot be so developed, are necessary to respond rapidly to the production issues currently facing Continental Automotive.

In the short term, addressing the current issue firstly necessitates modification in the packaging characteristics to effectively mitigate the problem. Specifically, a strategic adjustment involves the removal of 20% of components, equating to 50

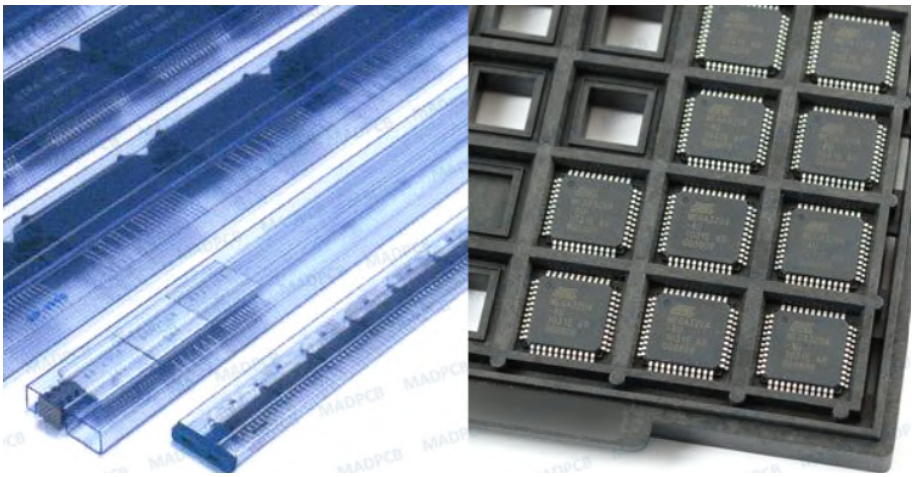

Figure 4.9: Examples of tube (left) and tray (right) packaging types [5].

pieces, from the end of the reel. This modification aligns with the 20 empty slots that have already been incorporated into the packaging by the supplier. By strategically removing components at the end of the reel, we aim to minimize the risk of deformation and enhance the overall integrity of the electronic components during handling and assembly.

Simultaneously, adapting the logistics flow is crucial to accommodate this sensitivity to deformation. Clear and stringent handling instructions must be communicated throughout the logistics chain to ensure that the modified packaging is treated with the utmost care. This includes providing specific guidelines for storage, transportation, and handling to mitigate the risk of mechanical deformation.

In concrete terms, this means working to limit the number of manipulations required in the supply chain, from delivery onwards. In addition, it will be necessary to restrict reel handling by operators (logistics and production) by issuing instructions requiring them to handle reels with both hands, so as to limit the mechanical stresses to which they are subjected. In fact, two-handed handling enables reels to remain stable with two support points, rather than being clamped on one side, which also causes additional bending due to the eccentricity of the coil's center of gravity in this position.

By implementing these short-term measures, we strive to enhance the resilience of the components and optimize the logistics flow, ultimately contributing to the overall quality and reliability of the manufacturing process.

Mid-to-long term

Looking at the mid-to-long term perspective, strategic decisions and actions need to be implemented for a sustainable resolution. A critical design choice must be made, and there are two potential approaches: either adapt the packaging design to the design of the electronic component, or vice versa, adapt the design of the component to align with the packaging. This decision will require a comprehensive

evaluation of mechanical conditions and compatibility.

On the one hand, in terms of conditioning and packaging, two primary options emerge. The first option involves the utilization of tape and reel. For this, the reel design requires scrutiny, with potential modifications to align with mechanical conditions. Alternatively, increasing the reel radius is an option, albeit necessitating the establishment of a specific logistics flow due to storage sizing requirements.

The second option entails exploring alternative packaging methods, such as trays, allowing for flat storage of components. This option raises considerations related to the pick-and-place process, and a thorough evaluation of its compatibility with the manufacturing workflow will be essential.

These mid-to-long-term actions emphasize the need for a strategic approach to address the root causes of the deformation issue, ensuring a more robust and sustainable solution for the overall manufacturing process.

On the other hand, for considering improvements to the component design, several key ideas emerge. First and foremost, a modification to the component design is proposed, focusing on incorporating rounded edges, thus increasing the quadratic moment of the beams by strategically adding material in the z direction. This idea is already present in the design of the MSA shield (see Figure 4.10), and should be considered for application to the LAIRD shield. This adjustment aims to reduce stress concentrations and enhance the overall structural integrity of the component.

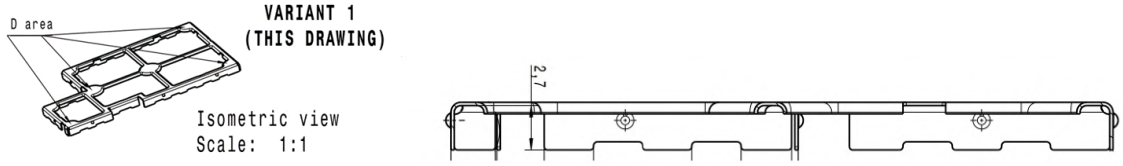

(a) (b)

Figure 4.10: MSA shield isometric view (a) and cross-sectional view (b).

Additionally, a material change is suggested, with the proposal to transition to S690 steel. This alternative material boasts more than twice the stiffness of the current S275 steel (as shown in Figure 3.13, section 3.3.4), contributing to a higher resistance against deformation. This material switch is anticipated to play a pivotal role in fortifying the component's structural properties and addressing the challenges identified in the manufacturing process.

In essence, these proposed modifications to the component design, encompassing rounded edges, increased quadratic moment, and a material change, collectively aim to elevate the resilience of the component, laying the groundwork for a more effective, long-term solution to the deformation issue.

Conclusion

This research has provided valuable insights into the intricate challenges posed by the assembly process of EMI shields in the production of Continental Automotive's BSRF EA. By meticulously tracing and analyzing the origins of the mechanical deformation issue exhibited by one of the shields, we have contributed to the understanding of manufacturing defects and their implications on overall product usability.

We have gone a long way to establish technical analyses confirming the origin of the issue encountered, while at the same time attempting to devise a concrete solution targetting the packaging: a new version of the T&R packaging could be delivered and tested within the allotted time. Although some of the tests were not conclusive, some insights were formulated after analysing the results and have potential to lead to more satisfactory progress.

While definitive curative solutions may still be in development, the work done here underscores the importance of holistic thinking in addressing complex industrial challenges. The emphasis on root cause analysis, the scrutiny of component packaging, and the collaborative approach involving production, technical competence centers, and industrial projects have collectively laid the groundwork for future advancements. The lessons derived from this exploration not only offer potential remedies for the specific issue at hand but also contribute to a broader purpose of optimizing design and industrialization processes.

On a secondary level, this study also aims to offer insights for organizations looking to improve their approach to risk assessment, specifications definition, and collaboration with internal and external stakeholders.

Appendix A

Principles of EMI and shielding

EMI (Electro-Magnetic Interference) shielding is a technique for limiting electromagnetic interference by creating a barrier between a source of electromagnetic field and the device to be protected. EMI, sometimes referred to as Radio Frequency Interference (RFI), is a common problem for most electronic devices, as it can reduce their performance or even cause them to fail. EMI is the result of the coupling of signals from one system to another, occurring between a source and a receiving element [9].

The source is usually an external circuit or phenomenon that creates an electromagnetic disturbance, whether of natural or artificial origin. The receiver, or victim, is the signal or sensitive device whose output signal is distorted by the interference. Signal coupling can occur in four different modes [9] (shown in Figure A.1):

- **Conductive EMI:** The first mode, conductive EMI, arises when an electrical link between two circuits exists, permitting stray signals or currents to move between them. Conducted EMI can be categorized into two types: common mode and differential mode. In common mode, stray currents from both systems travel in the same direction through a shared ground connection, acting as a common return path. Conversely, in differential mode, the undesired current flows in opposite directions through both systems via the supply lines and is not reliant on the ground connection.

- **Radiated EMI:** The second mode, radiated EMI, propagates in the free space between the source and the receiver. A source emits an electromagnetic wave which is unintentionally transmitted to a circuit. Conductors such as cables and printed circuit boards can act as antennae, transmitting and receiving an external electromagnetic wave.

- **Capacitive EMI:** The third mode, termed capacitive EMI, takes place when two closely spaced conductors within a system, typically less than one wavelength apart, come into play. This minimal gap gives rise to a parasitic capacitance, where electrical charge accumulates and moves through charge differentials. These charge differentials result from the electric fields generated by the adjacent conductors. Consequently, the parasitic capacitance serves as a conduit for unintended signal transfer.

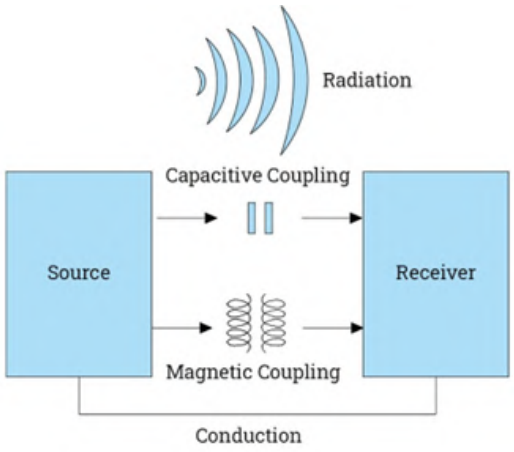

Figure A.1: Types of EMI coupling modes [9]

- **Magnetic EMI:** The fourth mode, magnetic EMI, bears similarities to capacitive coupling, particularly in terms of its occurrence at close distances. In this mode, signal transfer happens through the generation of a current in another conductor via electromagnetic induction. This occurs when there are changes or oscillations in the current flowing through the first conductor.

In addition, EMI can be classified according to its duration: a distinction is made between continuous and pulsed interference. In the case of continuous interference, the source continuously emits the unwanted signal. These are generally characterized by their low energy and frequency. Examples include radio frequencies, electric field leakage from industrial equipment, etc.

Pulse interference, whether intermittent or transient, is electromagnetic interference that occurs only for a short period of time. The definition of its duration varies according to application, but is generally less than the period of an alternating current cycle: $1/50\text{Hz} = 20\,\text{ms}$ in Europe and $1/60\text{Hz} = 16.67\,\text{ms}$ in other countries such as the USA. Impulse interference is characterized by strong bursts of energy that can occur repeatedly or randomly. A repetitive event is usually artificial, making it predictable in terms of amplitude and duration. A random event can be artificial or natural, such as lightning, power surges, electric discharges, etc.

Another way to classify electromagnetic interference considers the spectral band's width of the disturbance, which can either be narrow or wide. The signal's bandwidth corresponds to that of the receiver and is referred to as the resolution bandwidth. In a narrow-band disturbance, the bandwidth is less than or equal to that of the receiver, whereas a wide-band disturbance has a broader bandwidth.

Through the various modes presented, EMI thus gives rise to a plethora of adverse effects, including the reception of jammed or distorted signals by communication devices, unintended power outages, fluctuations in power supply, electrical fast transients[1] (EFT), malfunction or damage to electrical circuits, diminished lifespan and performance of electronic systems, potential electric shocks, burns, and ignition

[1] Abrupt, short-duration bursts of electrical energy or voltage spikes that occur on power lines or electrical circuits.

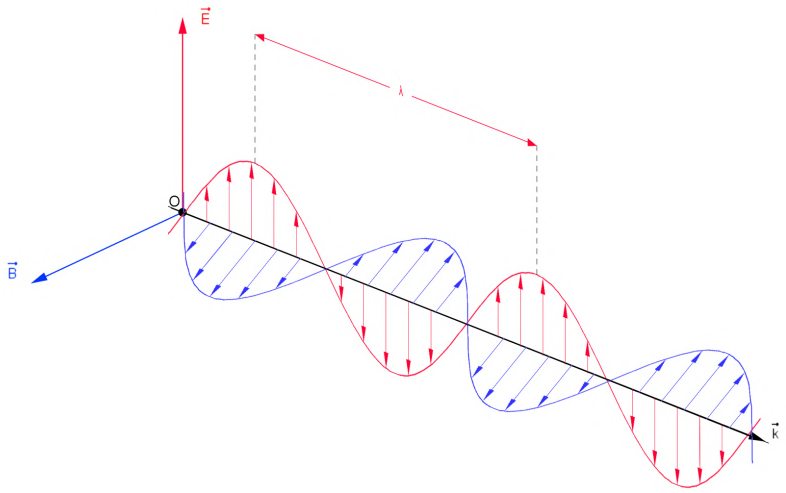

Figure A.2: Electromagnetic wave [8]

hazards.

Furthermore, as electronic systems become increasingly prevalent for communication and control purposes, particularly in automotive systems and beyond, EMI, along with other disturbances stemming from electrical transmission, distribution systems, and natural events like lightning strikes and solar flares, contributes significantly to the contamination of the electromagnetic wave spectrum.

To solve these problems, electromagnetic compatibility (EMC) standards have been developed. EMC is the ability of electronic equipment to function correctly in an electromagnetic environment without generating or transmitting electromagnetic energy to other equipment or systems. These standards aim to guarantee the EMC of industrial systems and all the components present in products. They are defined in France by the International Special Committee on Radio Interference (CISPR), a branch of the International Organization for Standardization (ISO). In the USA, EMC standards are managed by the Federal Communications Commission (FCC).

EMI shielding is one of the techniques used to ensure EMC. It involves isolating a region of the electronic system containing a potential source or receiver of EMI, using a closed enclosure with materials, structures and shapes appropriate to alter the path of unwanted electromagnetic waves entering or leaving the region. Shielding absorbs or reflects electromagnetic waves by its conductive or ferromagnetic properties.

As a reminder, electromagnetic waves comprise an electrical component and a magnetic component, which travel at the same frequency and are orthogonal to each other. These components define an electromagnetic field acting throughout space and governed by Maxwell's equations (see below).

$$\vec{\nabla} \cdot \vec{E} = \frac{\rho}{\epsilon_0} \quad \text{Gauss's Law} \tag{A.1}$$

$$\vec{\nabla} \cdot \vec{B} = 0 \quad \text{Gauss's Law for Magnetism} \tag{A.2}$$

$$\vec{\nabla} \times \vec{E} = -\frac{\partial \vec{B}}{\partial t} \quad \text{Faraday's Law of Induction} \tag{A.3}$$

$$\vec{\nabla} \times \vec{B} = \mu_0 \left(\epsilon_0 \frac{\partial \vec{E}}{\partial t} + \vec{J} \right) \quad \text{Ampere's Circuital Law} \tag{A.4}$$

A conductive material blocks the electric component of the field, while a material with high magnetic permeability blocks its magnetic component. As the two components of the electromagnetic field are intrinsically linked - Maxwell's equations dictate their simultaneous existence or conjugate cancellation - damming one of the two components is enough to block all the electromagnetic power transmitted through space.

A.1 EMI shielding mechanisms

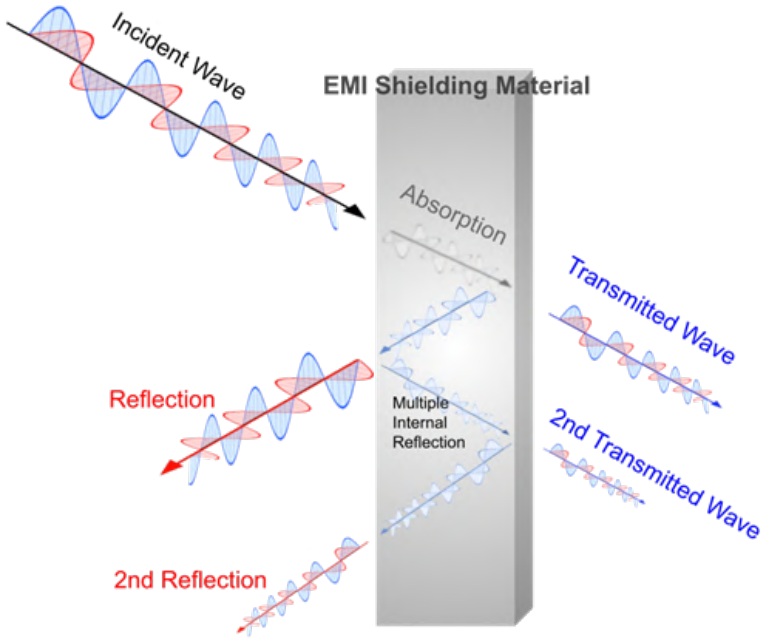

Figure A.3: Shielding mechanisms [9]

The main protection mechanism against EMI is reflection, which reduces the electrical component of EMI. To reflect EMI, the material used for shielding must have mobile charge carriers, i.e. be a good conductor. The incident electromagnetic wave interacts with the mobile charge carriers present in the conductive shielding, causing charges to circulate and redistribute along the conductor, creating an opposing electromagnetic field that cancels out the external electromagnetic field.

Material conductivity is a crucial parameter in determining shielding effectiveness. However, any discontinuity in the envelope larger than the wavelength of the external electromagnetic field will cancel out its shielding properties. To minimize shielding losses, holes and openings are kept to a minimum when designing the enclosure. However, this is not always possible for higher wave frequencies, and the use of filtering devices is necessary to remedy this EMI problem.

Another phenomenon that affects shielding performance is the skin effect, which occurs in AC circuits. Alternating current tends to accumulate on the surface or in the upper layers of the conductor, reducing the conductivity of the inner cross-section, and therefore the performance of the shield. To remedy this, the conductor surface can be increased, thereby increasing the effective conductive cross-section. Alternatively, the shield can be electroplated, or cataphoresis, to deposit a highly conductive material such as silver or copper on its surface [9].

A secondary mechanism of EMI shielding is that of absorption, which deals with the magnetic component of EMI. The materials adapted for electromagnetic absorption require a high dielectric constant and magnetic permeability. When these materials are subjected to an external magnetic field, the magnetic field lines pass through the material. An enclosure with these properties creates a guide for the magnetic field lines, which absorbs the electromagnetic field on the other side of the shield. However, these materials have insufficient electrical conductivity to protect effectively against the electrical component of the electromagnetic wave.

The attenuation of the incoming electromagnetic wave by eddy currents is also part of the absorption mechanism. This phenomenon occurs when the electromagnetic wave oscillates at a high frequency and induces currents inside the conductor. Eddy currents generate a magnetic field that opposes the external magnetic field. Materials with high electrical conductivity can generate eddy currents of higher intensity.

Furthermore, composite materials with large interfacial areas or porous surface structures can implement a shielding mechanism based on multiple reflections. This mechanism results in the dispersion of electromagnetic waves within the material [9].

A.2 Design options

Good EMI shielding design reduces the need for internal devices to manage unwanted signals.

Two factors are decisive: the design of the structure, and the materials used. A simple EMI shield is a Faraday cage made of conductive materials such as copper. The design of EMI shielding depends on the characteristics of the electromagnetic environment in which the equipment is to operate reliably. Here are some EMI shielding design considerations.

The structural design of EMI shielding is crucial to ensure maximum effectiveness. To minimize radiated EMI leakage, discontinuities must be reduced as much as possible. It's also important to create a homogeneous conductive layer by securing housings at every joint and discontinuity, as well as promoting metal-to-metal contact by soldering or brazing. Similar metals are usually bonded to avoid galvanic corrosion.

The poorest electrical connection determines the effectiveness of the shielding. Thus, the slightest fault in the bonding will condemn the entire shield to malfunction. If a permanent connection is not possible, the fastening method chosen must exert sufficient pressure to maintain contact.

Irregular surfaces should be fitted with EMI shielding gaskets to ensure continuous electrical contact. Gaskets should be as thin as possible without compromising their strength and should be compressed with sufficient pressure. Housing contact surfaces must be free from contaminants such as oil, moisture, rust, and dirt. Cable penetrations can degrade shield integrity, requiring the use of appropriate filters to create desired impedance discontinuities [9].

Cable shielding is used for signal lines that penetrate shielded enclosures and are grounded to the outer shield. Openings for ventilation and moisture evacuation must be limited in size so as not to reduce the effectiveness of the shielding: their size must be less than the operating wavelength. If it is impossible to reduce the size of openings, shielding screens can be used.

The choice of construction materials is also crucial to ensuring EMC. Like structural choices, the choice of materials depends on the electromagnetic environment in which the electronic system operates (the relative strength of the electric and magnetic components of the electromagnetic field involved).

EMI shielding of electronic devices is achieved by using materials with the appropriate electrical conductivity and magnetic permeability to impart the desired properties to the device.

Metals such as copper and aluminum are the most widely used for their electrical conductivity. In fact, their cost-effectiveness makes them more attractive than silver, even though the latter is a better conductor. This is why silver is only used as an alloying component or as an electroplated surface coating.

Iron-nickel alloys such as Mu-metal, Permalloy, and Supermalloy are commonly used for magnetic shielding. For instance, Mu-metal has a relative permeability of 100 000 at 1 kHz (i.e. taking the magnetic permeability of air equal to 1). Carbon allotropes such as exfoliated graphite, graphene, carbon fibers, and carbon nanotubes are effective filler materials for EMI protection composites due to their intrinsic rigidity and conductivity. Intrinsically conductive polymers such as polyaniline (PANI) and polypyrrole (PPy) can conduct electricity via conjugated bonds. However, their use is limited by problems of mechanical and chemical stability [9].

Low-frequency circuits are generally characterized by currents that generate magnetic fields. High-frequency circuits, on the other hand, are often characterized by voltages that produce electric fields. To offer protection against electric fields, most of the construction materials commonly used for shielding are sufficient. Aluminum, copper, and silver are typical examples of such materials. The predominant shielding mechanism in these cases is signal reflection.

However, to offer effective protection against magnetic fields, it is necessary to use materials with high magnetic permeability. Mu-metal and iron are common examples of such materials. In this case, the predominant shielding mechanism is absorption rather than reflection.

Finally, shielding materials can be coated by painting, spraying, dispensing, and electroplating [9].

Appendix B

Technical drawings

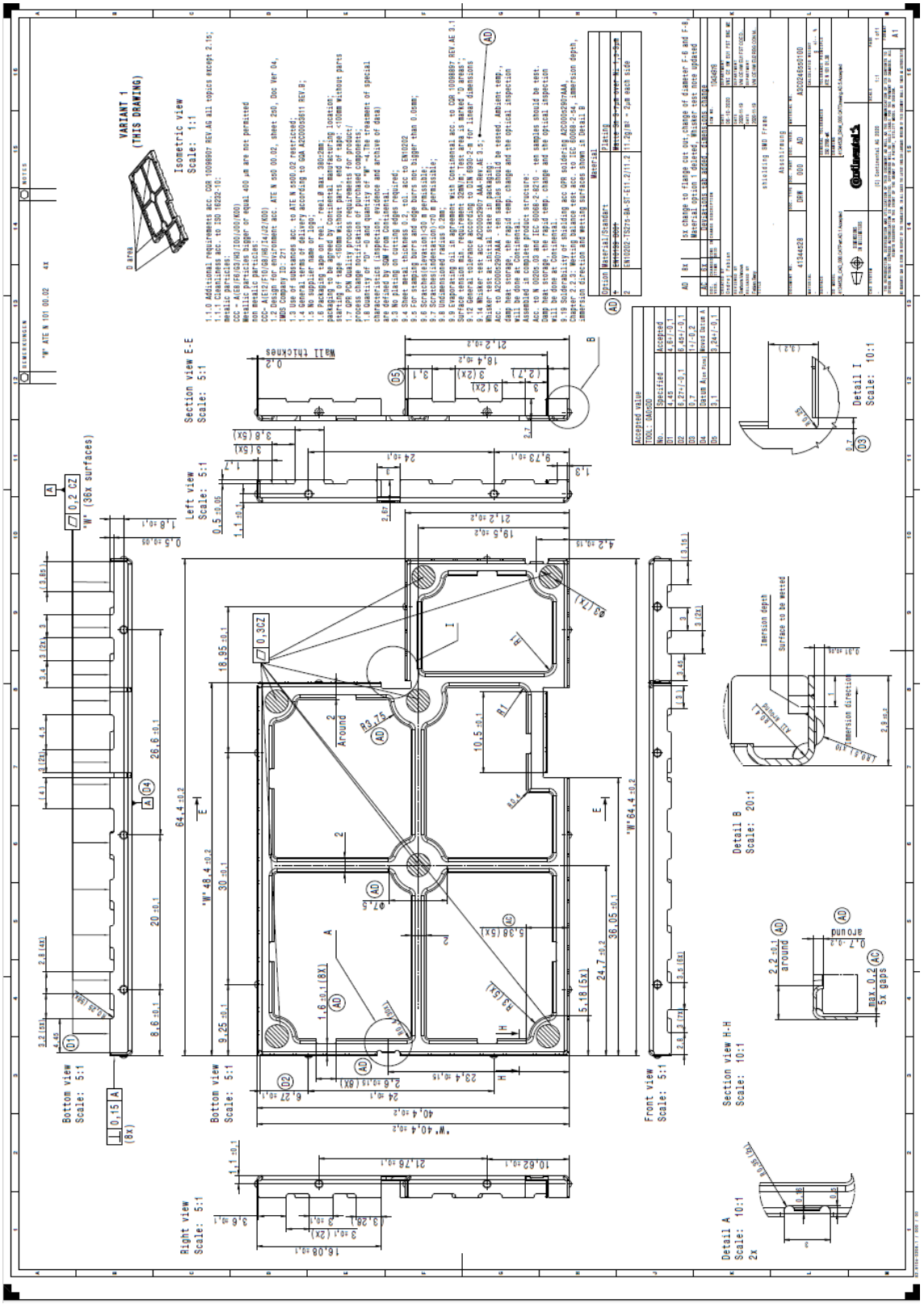

Figure B.1: MSA shield full technical drawing.

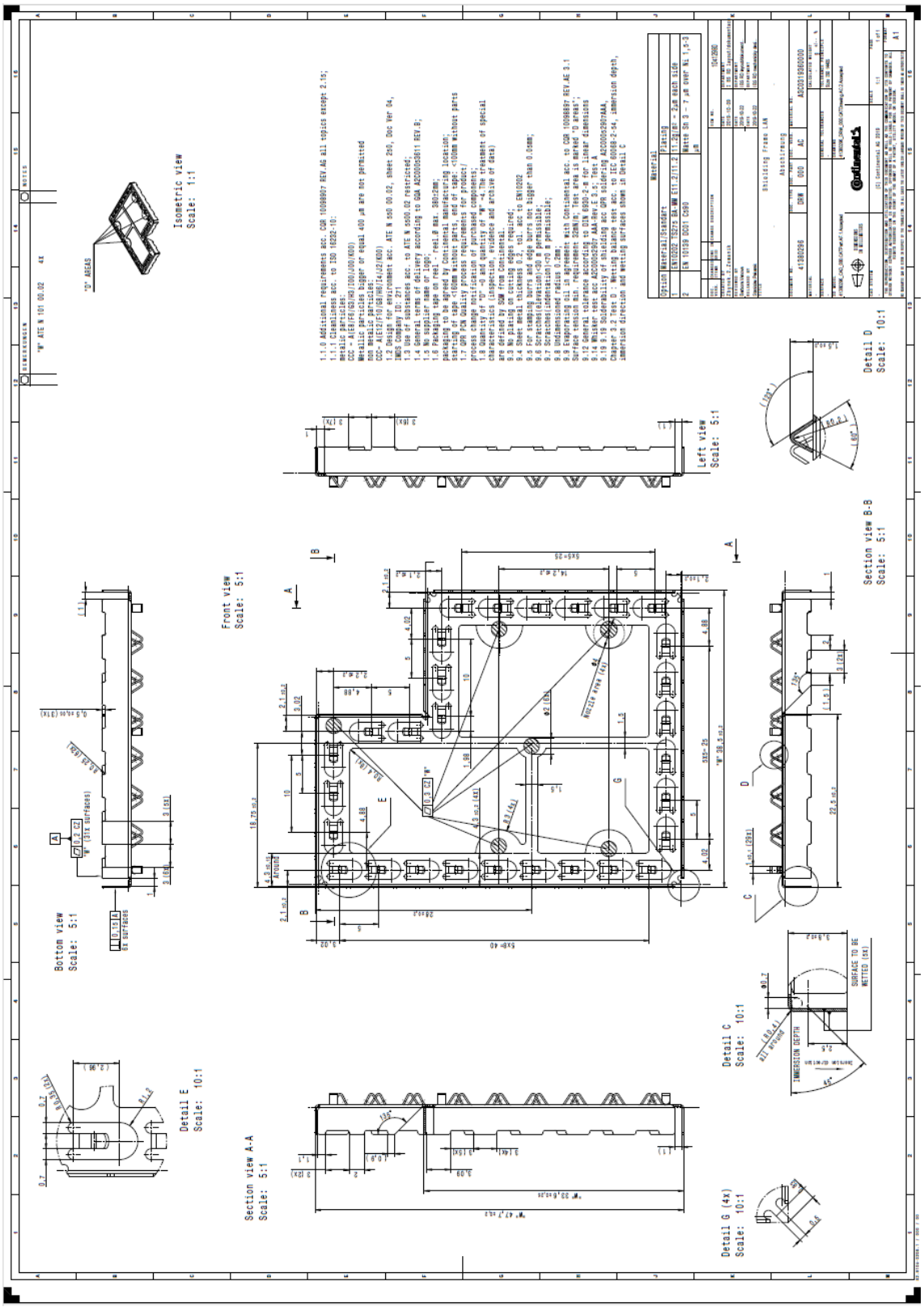

Figure B.2: LAIRD shield full technical drawing.

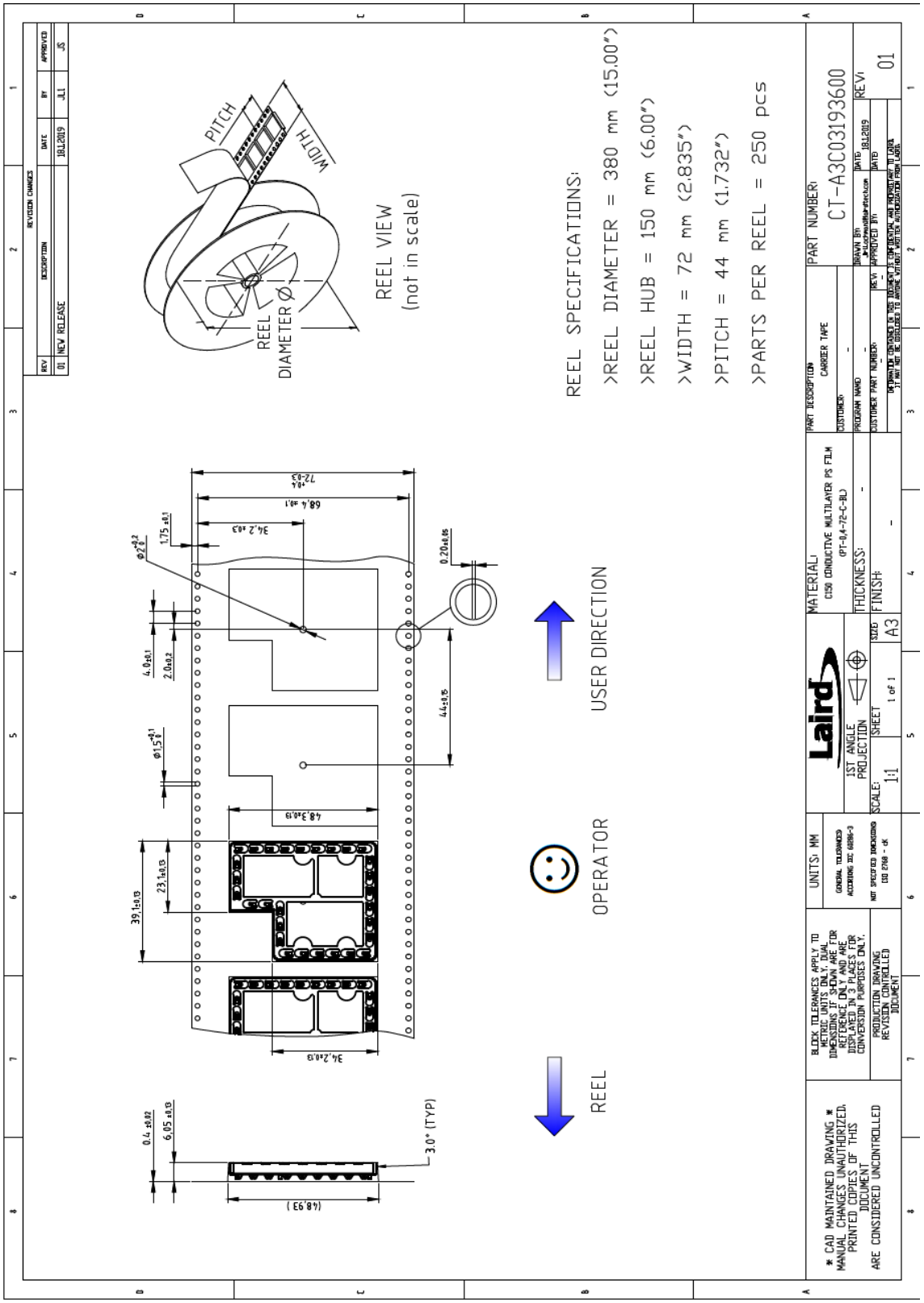

Figure B.3:
LAIRD shield initial packaging full technical drawing.

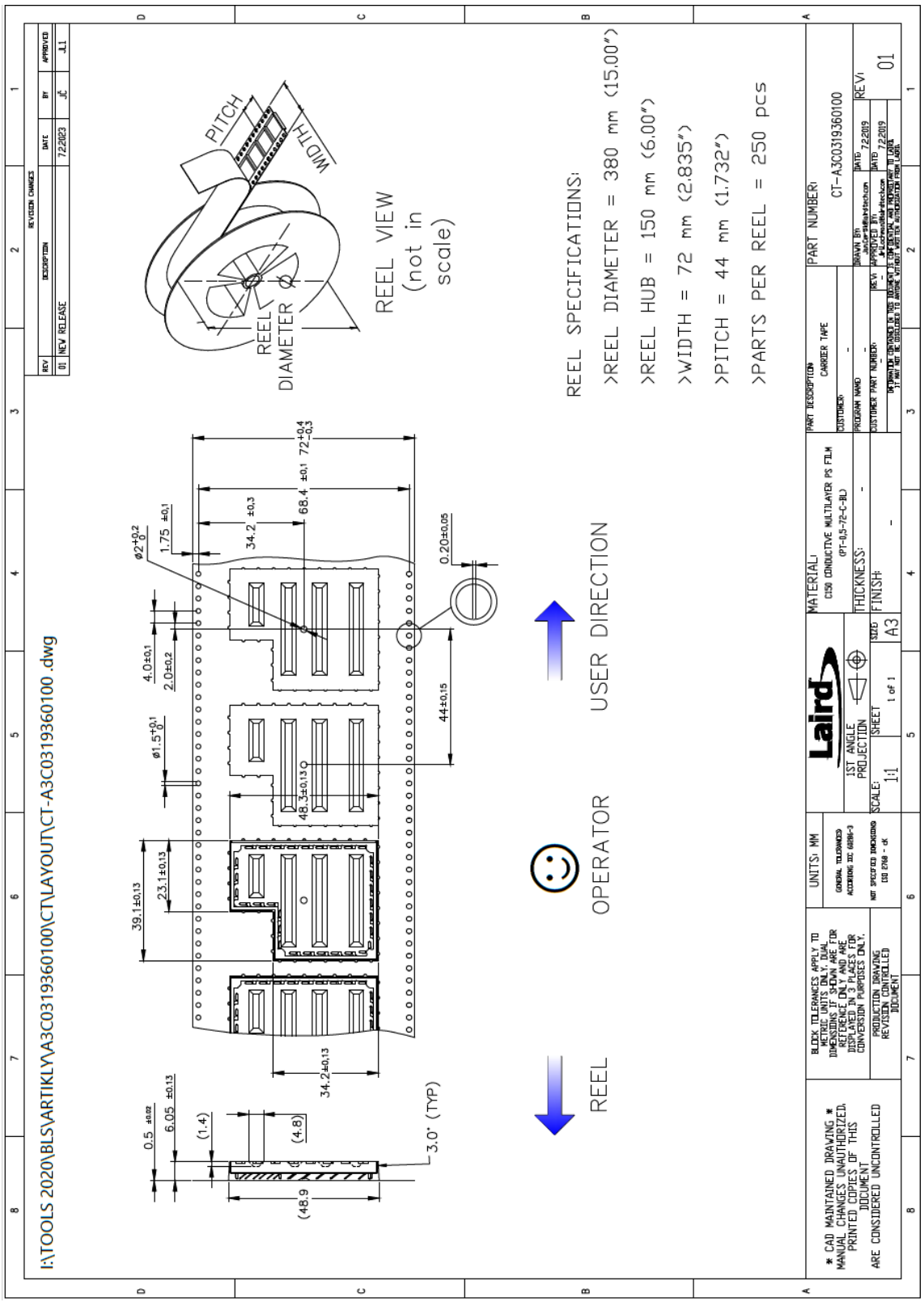

Figure B.4: LAIRD shield modified packaging full technical drawing.

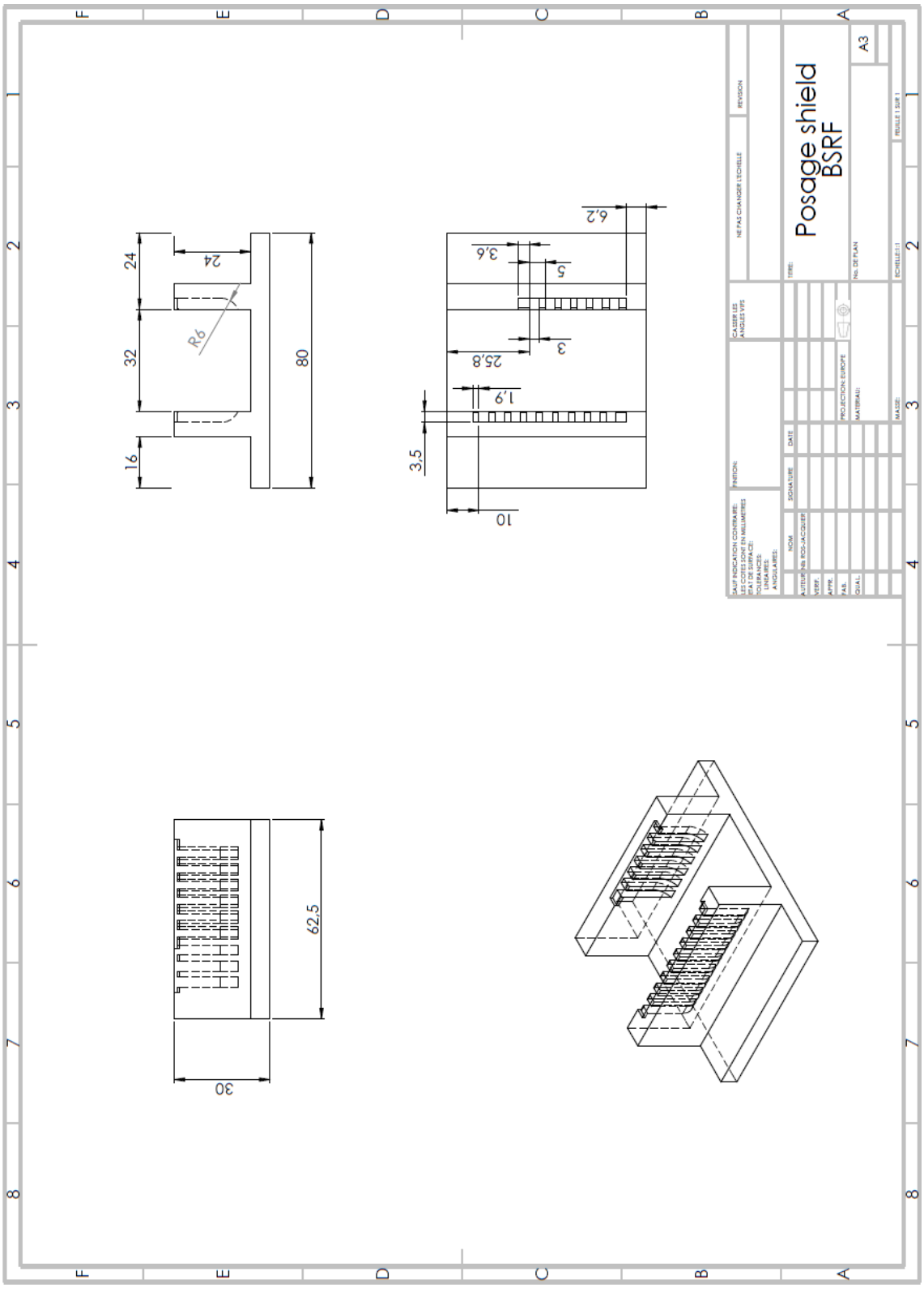

Figure B.5: Full technical drawing of the custom fixture designed for bending tests.

Appendix C

Annex on measurement methods

5 Procedure (cont'd)

5.1 Seating plane method (cont'd)

f) The triangle of terminals defining the seating plane must encompass the projection of the center of gravity (C.O.G.) in order to constitute a valid seating plane. If the plane is not considered valid, the next terminal with the greatest perpendicular distance from the substrate shall be considered as a candidate terminal to be used in forming a valid seating plane. If the seating plane triangle passes through the package center of gravity, the seating plane will be valid, but multiple seating planes could exist. If multiple seating planes do exist, the seating plane yielding the worst-case measurement shall be used for coplanarity determination.

g) Deviation from coplanarity is measured as the distance from the seating plane to the apex of each and every terminal. The largest measurement is the deviation from coplanarity; see Figure 2 and Figure 3 (BGA versus leaded terminal).

h) Report that the deviation from coplanarity was determined by the seating plane method.

Most equipment used for coplanarity measurement is programmed to automatically perform both seating and regression plane coplanarity measurements. Annex A is an illustrative example of how the seating plane on the terminals of a component is determined in the dead-bug position.

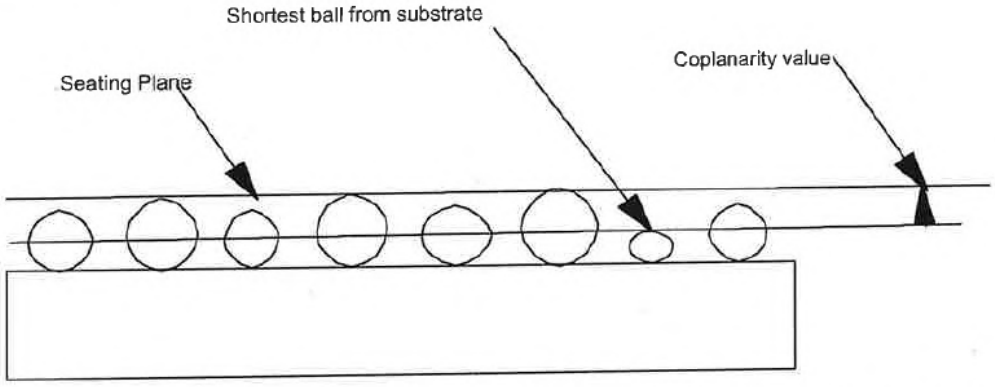

Figure 2 — Coplanarity measurement using seating plane method on ball grid array terminal

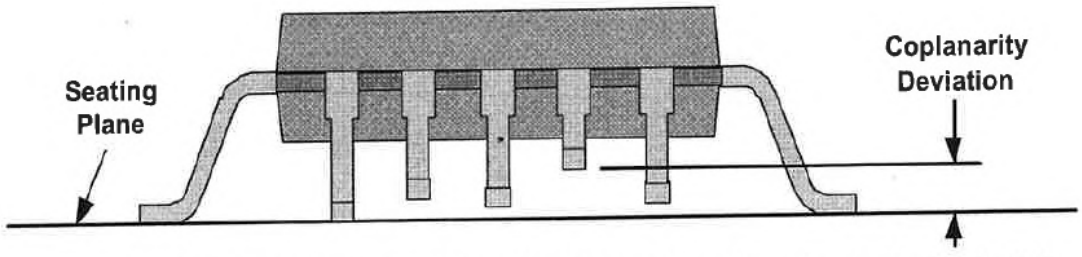

Figure 3 — Deviation from coplanarity meas urement using seating plane method on leaded terminal

Figure C.1: Seating plane method for coplanarity measurements.

List of Figures

List of Tables

Bibliography

[1] Continental Aktiengesellschaft. Continental 2022 annual report. *https://annualreport.continental.com/2022/en/service/docs/annual-report-2022-data.pdf*, 2023.

[2] Basic characteristics of a shark antenna and advantages of this setup: https://www.futura-sciences.com/tech/definitions/smartmotion-antenne-requin-19463/.

[3] Mobility Outlook Bureau. Continental readies automotive technologies with new management. *https://www.mobilityoutlook.com/news/continental-readies-automotive-technologies-with-new-management/*, 2021.

[4] Continental Automotive website: https://www.continental-automotive.com/en-gl/Passenger-Cars/Architecture-and-Networking/Vehicle-Telematics-Solutions/Telematics-Control-Units.

[5] MADPCB website: https://madpcb.com/glossary/tube-and-tray/.

[6] *JEDEC No. 22-B108A: Coplanarity Test for Surface-Mount Semiconductor Devices.*

[7] Pierre-Olivier Martin. Formulaire résistance des matériaux - calcul des poutres. *https://metaletech.com/wp-content/uploads/2021/03/Formulaire-RdM-Poutres-simples.pdf*, 2021.

[8] Electromagnetic wave diagram from the website: https://commons.wikimedia.org.

[9] Industrial Quick Search. Emi shielding. *IQS Directory website: https://www.iqsdirectory.com/articles/emi-shielding.html.*

[10] Sinerji-grup website: https://www.sinerji-grup.com/smd-production-line-solutions-1.

[11] Database of engineering materials designed by scientists of the National Technical University KhPI: https://www.steelnumber.com.

[12] Université de Pau et des Pays de l'Ardour website: https://www.univpau.fr.

[13] F. Yang and M. Veljkovic. Damage model calibration for s275 and s690 steels. *ce/papers, 3: 262-271. https://doi.org/10.1002/cepa.1201*, 2019.